Norris, Neve Traquair (2025) *Spatial variability of meander characteristics in an avulsing distributive fluvial system.* MSc(R) thesis.

https://theses.gla.ac.uk/85301/

Copyright and moral rights for this work are retained by the author

A copy can be downloaded for personal non-commercial research or study, without prior permission or charge

This work cannot be reproduced or quoted extensively from without first obtaining permission from the author

The content must not be changed in any way or sold commercially in any format or medium without the formal permission of the author

When referring to this work, full bibliographic details including the author, title, awarding institution and date of the thesis must be given

Enlighten: Theses
https://theses.gla.ac.uk/
research-enlighten@glasgow.ac.uk

Spatial Variability of Meander Characteristics in an Avulsing Distributive Fluvial System

Neve Traquair Norris BSc Hons

Supervisors: Dr. Amanda Owen, Dr. Laura Quick, and Professor Richard Williams

Submitted in fulfilment of the requirements of the Degree of MSc by Research

School of Geographical and Earth Sciences, College of Science and Engineering, University of Glasgow

Abstract

Previous studies of meandering fluvial systems have mainly focused on meanders at a localised 'reach' scale within a river system, without consideration of the spatial context. As such, much of the research has focused on exhumed meander deposits instead of active meanders. More research is therefore required on the spatial variability of meander deposits across a single system or sedimentary basin. Recent research has found meandering fluvial systems to be a dominant planform type in modern-day sedimentary basins; meander deposits are consequently assumed to be more dominant than originally perceived in the fluvial rock record. Distributive fluvial systems (DFSs) have also been shown to dominate sedimentation patterns in modern-day aggradational sedimentary basins and therefore warrant further study due to their abundance. Due to the prevalence of meandering systems and distributive fluvial systems in modern-day sedimentary basins, this study aims to fill a critical literature gap with regards to the spatial and temporal variability of meander characteristics across a modern-day distributive fluvial system (i.e., from apex to toe of a DFS). This study uses satellite imagery of Brazil, acquired through Google Earth Engine and analysed in ArcGIS software, to conduct a spatial analysis of the meandering Taquari DFS. The Taquari DFS is a well-documented, dominantly meandering system, which provides a good spatial context for the study of meander characteristics across the DFS. Spatial changes in: channel width, channel belt width, meander deposit dimensions and sinuosity are quantified on the Taquari DFS to explore downstream changes in meander characteristics within this system. Polygons are created in ArcGIS using the available satellite imagery, which allows for detailed measurements of meander dimensions downstream. This study also explores the temporal changes in channel width, channel belt width, meander deposit dimensions, and sinuosity on the Taquari DFS since the initiation of the large Caronal avulsion (initiation between 1996 to 1997) by comparing meander dimensions pre-avulsion and during-avulsion. The Caronal avulsion is ongoing and continues to divert flow from the parent channel to the avulsed channel. Using the oldest and most modern satellite imagery available from 1985 and 2022, respectively, fluvial dimensions are compared between pre-avulsion (1985) and during-avulsion (2022) imagery, to understand the impact of the avulsion on the parent channel (active channel) and its associated channel belt and meander deposits. On the modern Taquari DFS (2022), active variables (i.e., active channel width, active channel belt width, and active meander deposit dimensions) show a decrease in dimensions downstream, with a significant decrease in dimensions downstream of the avulsion point (where flow is diverted to the avulsed channel). Pre-avulsion variables were also identified on the 2022 satellite imagery including pre-avulsion channel belt width and abandoned meander deposit dimensions. Pre-avulsion channel belt width displays weak downstream trends and abandoned meander deposit dimensions display no downstream trends. Important differences in downstream trends were identified between active and abandoned meander deposit dimensions along the Taquari DFS. The active meander deposits are larger in size than the abandoned meander deposits upstream of the Caronal avulsion point and the abandoned meander deposits are larger than active meander deposits downstream of the avulsion point. The active meander deposits also show clear changes in size and shape downstream as they change from larger, more rounded deposits, to much smaller crescent-shaped deposits. The abandoned deposits however, display a range of shapes and sizes downstream and show no clear decrease in size, especially between medial and distal DFS zones. The decrease in active meander dimensions (active channel width, active channel belt width, and active meander deposit dimensions) is due to a decrease in discharge downstream as a result of typical DFS bifurcation processes in addition to the diversion of flow from the parent channel to the avulsed channel. Active meander deposit size and shape change downstream as sediment load, and therefore deposition, decrease as discharge decreases. The weak downstream trends displayed by the channel belt relate to confinement in the upper DFS where channel belt migration capacity is limited. The lack of downstream trends displayed by the abandoned meander deposits is due to the range of conditions under which these deposits were formed over time. This research has important implications for the understanding of avulsing rivers due to the significant decrease in width of the parent channel and the size of active deposit dimensions downstream, which influence the redistribution of water and sediment resources within modern DFS. In addition, this research creates an important database on the spatial variability of meander deposit dimensions on a modern DFS which can contribute to the understanding of sandstone-body reservoir dimensions which is important for resource exploration or hydrocarbon storage.

Table of Contents

List of Tables

List of Figures

Acknowledgement

I would first and foremost like to thank my primary supervisor Dr Amanda Owen for her patience and support through this whole project. In addition, my second and third supervisors Dr Laura Quick and Professor Richard Williams have been incredibly helpful with this project. Secondly, I would like to thank my family: Mum, Dad, Aela, and Phoebe who have been a constant for the past two years and have been incredibly supportive. Thirdly, I would like to thank my friends Careen, Chloe, Gopikaa, Puja, and Shona and all the Molema PGRs who have been some of the kindest people I have met in Glasgow. Finally, I would like to extend my thanks to Martin Stokes for providing valuable images of the Pantanal wetlands of Brazil.

Author's Declaration

"I declare that, except where explicit reference is made to the contribution of others, that this dissertation is the result of my own work and has not been submitted for any other degree at the University of Glasgow or any other institution."

Printed Name: NEVE TRAQUAIR NORRIS

Signature: ___________________________

1 Introduction

Understanding fluvial system behaviour is of great importance to the large human populations and vast ecosystems that occupy fluvial environments. Fluvial systems are important biogeochemical interfaces, form important political boundaries (Schumm, 1985; Rhoads, 2020), and are major conveyors of water and sediment to the world's water reservoirs (including oceans, seas, and lakes) (Leopold, 1962; Güneralp and Marston, 2012; Knighton, 2014). Overbank deposits from flood events also deliver important nutrients to floodplains, which are essential for agricultural activity (Poff, 2002).

The impact of flooding, erosion, and avulsion processes from river systems are major hazards for society, which can result in large loss of life and damage to critical infrastructure (Singh and Awasthi, 2010). Population density can be incredibly high in areas with availability of water resources and favourable conditions for agriculture (i.e., the Ganga Plains, India), however, when extreme flood events or avulsions occur their consequences can be catastrophic (Singh and Awasthi, 2010). Avulsions in particular can occur at any time and be triggered by normal flood events (i.e., if a river is at or near an avulsion threshold), and pose even greater risks to populations and infrastructure due to the vast dispersion of water and sediment they generate (Slingerland and Smith, 2004). An *avulsion* is the diversion of flow from the channel to the floodbasin as a result of channel bank failure. The frequency of extreme events such as avulsions are becoming more common as climate change increases extreme flood events (Poff, 2002); it is therefore important to understand avulsion processes in modern river systems.

Understanding the deposits of fluvial systems is also of great importance to geologists as sediment deposited by rivers can become preserved in the rock record and form reservoirs that host many different minerals and other resources that can be of benefit to society (i.e., uranium, copper, petroleum, and water) (Owen et al., 2015; Swan et al., 2018; Hu et al., 2019; Nie et al., 2020; Rhoads, 2020). For example, point bar deposits from the meandering Powder River in Wyoming host large reserves of uranium and organic-rich siltstones (Berg 1968; Dalh and Hagmaier, 1976). Both uranium and organic-rich material are used to generate energy, with uranium being of particular interest as a source of carbon-free energy which is used to generate electricity instead of carbon-based energy (i.e., fossil fuels) (Chakravorty et al., 2012; Naik, 2024).

Fluvial deposits can also be critical for the transition to clean energy as fluvial sandstones have the potential to be geothermal sites (i.e., Frio Sandstones, Texas, USA; Bebout et al., 1978) or reservoirs, which can be used for carbon capture and storage (CCS) (i.e., Sherwood Sandstone Group, UK; Newell and Shariatipour, 2016). Colombera et al. (2017) examined modern case studies including the Mississippi (e.g., Jordan and Pryor, 1992) and the Ganges (e.g., Boeser, 2011) in addition to analogues from outcrops such as the McMurray Formation (e.g., Jablonski, 2012) and the Kayenta Formation (e.g., Miall, 1988) and found that point bar deposits within meander belts have a favourable geometry for subsurface storage due to the compartmentalisation of sandstone and mudstone that form ideal reservoirs.

When exploring and extracting resources it is critical to understand variations in deposit characteristics (e.g., grain size, sorting, porosity, permeability, gross geometry) which influence how subsurface fluids flow, become trapped, and are ultimately extracted (or stored) (Colombera et al., 2017). In addition, understanding subsurface geometries is critical to understand how pollutants are conveyed, to avoid the contamination of, for example, aquifers. For example, Xiao et al. (2020) found that high sinuosity rivers were able to accumulate high concentrations of nitrogen, a major pollutant in modern rivers, in concave banks of the channel.

This study aims to fill a critical literature gap with regards to understanding how characteristics of modern meandering distributive fluvial systems (DFSs) vary spatially within a system (i.e., the change in characteristics downstream) (Owen et al., 2015). This chapter will firstly introduce distributive fluvial systems and avulsions, before introducing different fluvial planform types. In particular, this chapter focuses in detail on meandering rivers including: terminology, formation, typical features, migration patterns, and deposits of meandering rivers in the rock record. Following this, the aims and objectives of the project are outlined prior to introducing the study area.

1.1 Literature Review

1.1.1 Distributive Fluvial Systems

Distributive fluvial systems (DFSs), also known as megafans or fluvial fans, are systems that disperse from an apex and terminate at a toe (Hartley et al., 2010; Weissmann et al., 2010; Davidson et al., 2013). The *apex* of a DFS marks the location where a river goes from being confined to unconfined and flow disperses in a radial manner; the *toe* of a DFS marks the location where the system terminates, at the furthest point from the apex (Figure 1.1) (Hartley et al., 2010; Weissmann et al., 2010; Davidson et al., 2013). DFSs typically have a fan-shaped morphology due to their unconfined nature, however, this is not always observed (Bull, 1968; Hartley et al., 2010). A DFS may be prevented from developing a fan-shaped morphology where the system is confined between two adjacent DFSs; sits in an axial position within a sedimentary basin; or has an incised channel on a DFS's surface preventing the development of floodplains which distribute sediment (i.e., in the upper reaches of the Taquari DFS, Brazil) (Weissmann et al., 2010). Fan-shaped DFSs develop radial patterns through

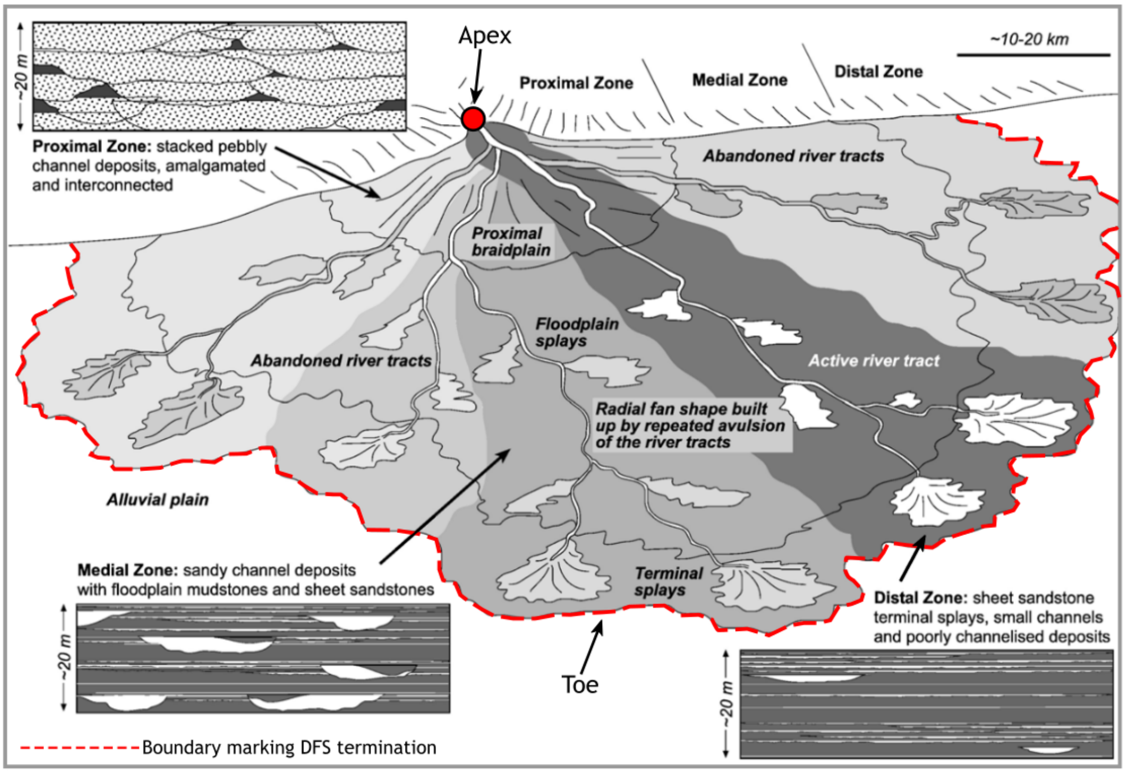

Figure 1.1. Distributive fluvial system (DFS) with proximal, medial, and distal zones. Frequent avulsion processes build a fan-shaped morphology and abandoned river tracts highlight previous channel orientations on the fan. Areas of more recent fluvial activity appear as darker grey colours and areas of the DFS abandoned for longer appear as lighter grey colours (Nichols and Fisher, 2007). Annotations highlighting the apex and toe of the DFS are done in Inkscape.

avulsion processes dispersing water and sediment across a sedimentary basin (Figure 1.1). Active areas of a DFS experience frequent deposition of sediment from active channels, which builds DFS stratigraphy; avulsion processes, which are outlined further later in this chapter, are responsible for changing the location of the active channel on a DFS and therefore result in wider sediment distribution across a DFS (Figure 1.1) (Nichols and Fisher, 2007). DFSs differ from tributary fluvial systems as DFSs tend to bifurcate downstream and reduce in channel size as flow disperses, whereas *tributary* systems involve smaller channels feeding into a larger main channel within a topographically confined area (Weissmann et al., 2010; Davidson et al., 2013; Rhoads, 2020).

At the furthest reaches of a DFS (i.e., the toe), a variety of termination types can exist, as outlined by Hartley et al. (2010). For example, a DFS termination can be marked by the location of a distributary system changing into a *contributory* system, where instead of dispersing, many channels feed into one channel. A termination can also be marked by: a main DFS channel forming a confluence channel to an axial system; a main DFS channel becoming an axial system; a main DFS channel meeting a shoreline or playa edge; or a main channel no longer being identifiable in a dune field, playa, and/or wetland environment (Hartley et al., 2010).

Studies of both modern DFSs (i.e., the Taquari DFS; Weissmann et al., 2010, 2015, and the Okavango DFS; Hartley et al., 2010) and ancient DFSs (i.e., the Salt Wash DFS; Owen et al., 2015, and the Huesca DFS; Hirst, 1991 and Martin et al., 2021) have aimed to characterise downstream DFS trends by splitting a DFS into different zones. Within a DFS, three distinct zones are identified (proximal, medial, and distal) which have been found to display predictable downstream trends within each zone across all planform types in a variety of climates (Figure 1.1) (Weissmann et al., 2010; Davidson et al., 2013; Owen et al., 2015). These downstream changes include a decrease in channel size, channel belt size, channel presence, grain size, and discharge (as a result of infiltration, evaporation, and bifurcation of channels) as well as a decrease in the ratio of channel to floodplain deposits (Weissmann et al., 2010; Davidson et al., 2013; Weissmann et al., 2015; Owen et al., 2015; Martin et al., 2021). Floodplain presence is found to increase downstream (Weissmann et al., 2010; Hartley et al., 2010).

The *proximal* zone of a DFS is the area closest to the apex where the river leaves confinement and deposits coarse-grained sediment as the flow loses transport capacity once it becomes unconfined (Figure 1.1) (Weissmann et al., 2013). Highly amalgamated sandy channel bodies are deposited while being reworked due to frequent avulsion processes (Weissmann et al., 2010; Hartley et al., 2010; Weissmann et al., 2013; Weissmann et al., 2015; Martin et al., 2021). There is very little floodplain preservation or soil development in the proximal zone due to the frequent reoccupation of abandoned channels where fine-grained material is removed and reaches more distal portions of the DFS (Figure 1.1) (Weissmann et al., 2013).

In the *medial* zone of a DFS, the river avulses over a wider area and channel deposits are more frequently separated by floodplain deposits and well-developed soils (Figure 1.1) (Weissmann et al., 2013; Martin et al., 2021). Sediment supply and discharge decrease downstream, and channel bifurcation is more frequent (Weissmann et al., 2013). Levees become more common in this zone and avulsion processes result in channel migration across its basin (Weissmann et al., 2013).

In the *distal* zone of a DFS, the river has the widest area to avulse over with the lowest discharge and the finest grain size resulting in a dominance of floodplain deposits with sparse channel bodies (Figure 1.1) (Weissmann et al., 2013). Much of the deposition in this zone of a DFS is from avulsions which are more common (Weissmann et al., 2013). Additionally, the toe of a DFS may sit at relatively low elevation thus floodplains and soils may be poorly drained, and swamps and ponds are increasingly common (Weissmann et al., 2013).

DFSs have been shown to dominate fluvial sedimentation patterns in modern-day aggradational sedimentary basins; as shown in a study of over 700 modern continental sedimentary basins (Weissmann et al., 2010; Hartley et al., 2010; Davidson et al., 2013). The results of this study by Weissmann et al. (2010) indicate that there is likely a greater percentage of DFS deposits in the continental fluvial record than previously recognised. The debate whether tributary or distributive fluvial systems dominate sedimentation patterns in modern-day aggradational sedimentary basins has been ongoing for many years (i.e., Fielding et al., 2010; Heyvaert and Walstra, 2016). However, the most recent research indicates that it is in fact DFS that dominate these modern-day sedimentary basins (Weissmann et al., 2010; Hartley et al., 2010; Davidson et al., 2013). DFSs have been found to occur in a variety of climatic and tectonic settings including: arid, tropical, subtropical, continental and polar climates as well as in extensional, compressional, strike-slip, and cratonic tectonic settings (Hartley et al., 2010). In areas of active subsidence where accommodation space is created, DFSs are able to deposit and, due to subsidence, have a higher preservation potential in comparison to degradational river systems (Hartley et al, 2010; Weissmann et al., 2010; Owen et al., 2015).

Planforms including meandering, braided, straight, and anastomosing channels can develop on DFSs which can often interchange downstream (Nichols and Fisher, 2007; Hartley et al., 2010). Hartley et al. (2010) identified 6 dominant planform types which occur on DFSs from a range of planform types which are present on DFSs globally. Channel planforms identified downstream (in order of dominance) include: a single braided channel bifurcating into braided and/or straight channels; a single braided channel; a single braided channel becoming sinuous downstream (sometimes with bifurcations); a single sinuous channel; a single sinuous channel bifurcating into smaller sinuous channels; and many sinuous channels coexisting with no dominant single channel (Hartley et al., 2010). Hartley et al. (2010) found that braided planforms dominate just over half of the large DFS studied, however, Hartley et al. (2015) identified that meandering fluvial deposits make up a larger proportion of the fluvial rock record than previously realised and that they likely dominate modern settings as well.

Hartley et al. (2010) found that differences in slope gradient, climate, discharge and sediment supply on a DFS, influence the planform which is present. For example, a DFS with a steep gradient, dry climate, low discharge and high sediment supply tends to develop a braided planform. This is due to the fact that sediment can travel far as it is not intercepted or stabilised through vegetation. In contrast, a DFS with a low gradient, wet (more tropical) climate, high discharge, and low sediment supply tends to develop a meandering planform, which has a high sediment distribution capacity as a result of constant discharge. Planform changes downstream within a DFS are often influenced by changes in discharge and sediment supply from a river's catchment area, which is primarily controlled by the climate (Hartley et al., 2010).

Although DFSs have distinct downstream characteristics, which are identifiable in modern and ancient systems, they share many similarities with alluvial fans (Ventra and Clarke, 2018). Important distinctions need to be made between these fan types to distinguish them, for example, in the rock record (Ventra and Clarke, 2018). DFSs and alluvial fans both start in a confined valley before reaching an apex and forming a radial fan-shaped morphology (Ventra and Clarke, 2018). A key difference between these fan types is that DFSs are fluvial systems (driven by rivers), whereas *alluvial fans* are depositional landforms formed by sediment laden flows (i.e., dominantly dry fans that do not have the constant water supply associated with river systems) (Bull, 1968; Ventra and Clarke, 2018).

Alluvial fans tend to grow after short-lived hydrological events which result in sediment rich bedloads and suspended loads depositing sediment through debris flow events (Ventra and Clarke, 2018). DFSs in contrast, have a constant sediment supply as this type of river system collects sediment from the catchment area (Ventra and Clarke, 2018). As alluvial fans do not have a constant water or sediment supply, they often have much smaller aerial extents (<100 km^2) and radii (~1 to 20 km) (Hartley et al., 2010). DFSs, however, typically, have much larger aerial extents (10^3 to 10^5 km^2), with larger radii (>100 km) (Hartley et al., 2010). Alluvial fans typically have much higher gradient slopes (>1°) whereas DFSs have lower gradient slopes (<0.1°) (Hartley et al., 2010). The gradient of the slope is often influenced by discharge and tectonics (Bull, 1968).

1.1.2 Avulsions

Avulsions are one of the most important processes within a DFS, responsible for sustaining wetlands, growing floodplains, and controlling sediment distribution and transport within a sedimentary basin (Slingerland and Smith, 2004). Avulsion is the diversion of flow from a parent channel (main active channel) to a floodbasin via a local failure of channel banks during a high flow event (Figure 1.2) (Smith et al., 1989; Jones and Schumm, 1999; Slingerland and Smith, 2004;

Assine, 2005; Buehler et al., 2011; Makaske et al., 2012). Failure occurs within channel banks as crevasse splays break through channel levees, resulting in the distribution of sediment and water to floodplains (Figure 1.2) (Slingerland and Smith, 2004).

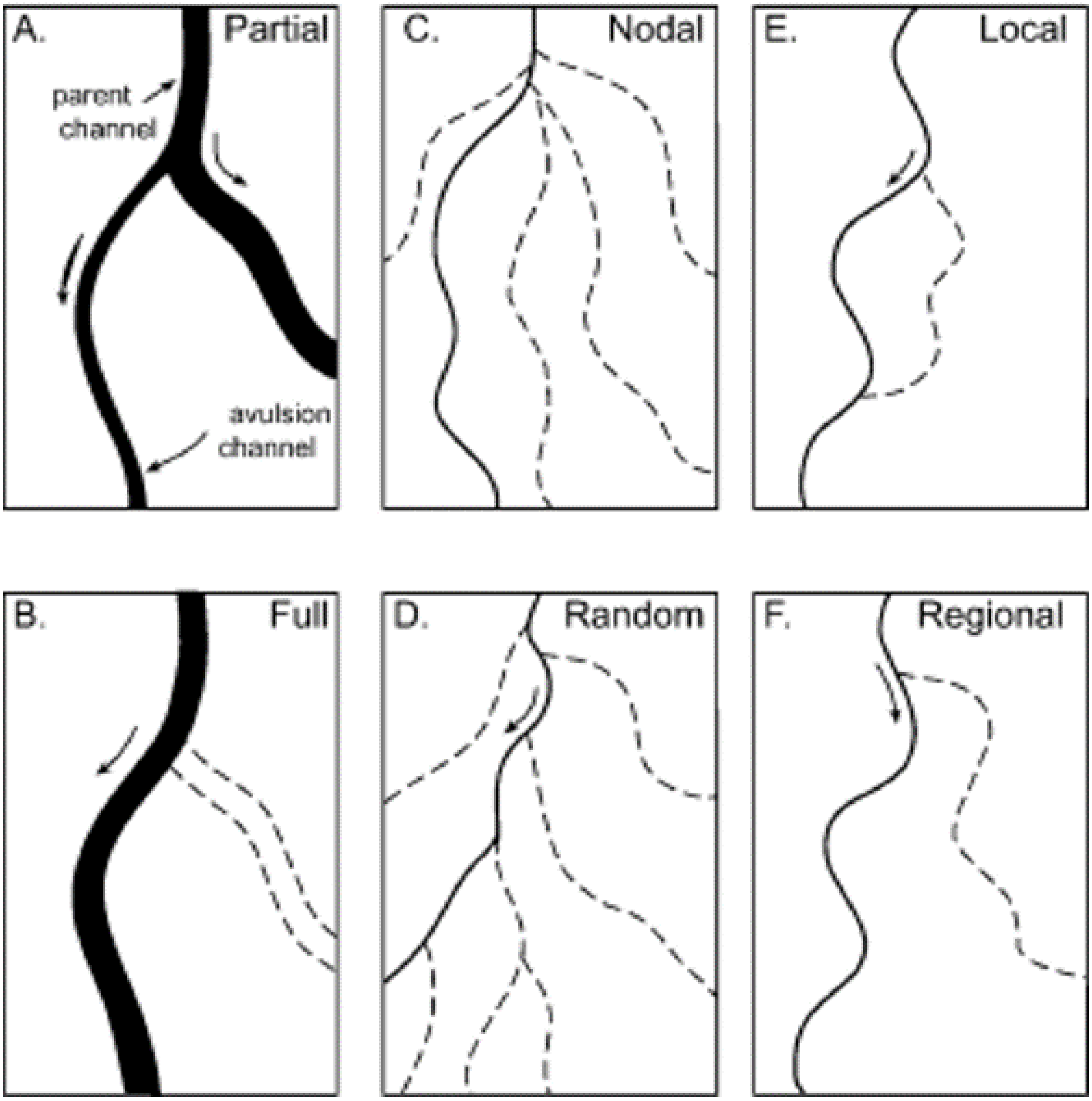

Figure 1.2. Avulsion styles showing the switching and abandonment or partial abandonment of parent channels to create avulsion channels (Slingerland and Smith, 2004).

When flow is diverted from a parent channel to a new avulsion channel it can be a complete shift in flow where a parent channel is abandoned or a partial shift in flow where a parent channel is still active as new channels form in the floodbasin (Figure 1.2) (Jones and Schumm, 1999; Assine, 2005). In some cases, flow may also be diverted before joining the parent channel again downstream (Jones and Schumm, 1999; Assine, 2005). Avulsions can occur quickly (i.e., decades) or over longer timeframes (i.e., centuries) (Slingerland and Smith, 2004). Flow that is diverted from a parent channel to an avulsion channel will find a route where the gradient is steepest away from the channel and flow is most efficient (Slingerland and Smith, 2004).

The size and extent of an avulsion reach is influenced by the amount of discharge and sediment diverted to the avulsion channel; the duration of the avulsion (i.e., how long it takes to shift flow completely or partially to an avulsion channel); and the characteristics of the floodbasin (i.e., topography) (Slingerland and Smith, 2004). Slingerland and Smith (2004) have identified three distinct types of avulsions that occur including: a) channel annexation, where an active channel is appropriated or an abandoned channel is reoccupied, b) incision of new avulsion channels into the floodbasin and c) progradation, where an avulsion deposits large volumes of sediment through different channels.

The most common triggers for avulsions are large flood events which exploit unstable sections of channel levees that have formed crevasses (Jones and Schumm, 1999; Assine, 2005). Although larger flood events are more likely to trigger avulsions, crevasse splays along levees can result from lower flow events where a channel is at or near an avulsion threshold (Jones and Schumm, 1999, Assine, 2005, Makaske et al., 2012). A combination of factors may bring a river closer to an avulsion threshold, i.e., if the channel belt is experiencing superelevation (Bryant et al., 1995).

Channel superelevation occurs where the sedimentation rate is high enough for channel aggradation to occur resulting in the elevation of a channel being higher than its adjacent floodplains (Bryant et al., 1995, Jones and Schumm, 1999, Slingerland and Smith, 2004). Aggrading rivers naturally build levees which slope towards floodplains where deposition of sediment occurs less frequently (i.e., via overbank deposits of a river flowing over full capacity) (Slingerland and Smith, 2004). When a high flow event occurs, a channel can lose the capacity to contain higher volumes of water and sediment within its banks. In this case, levee failure will naturally occur where a channel and its levees sit too high above the floodplains (Bryant et al., 1995; Jones and Schumm, 1999; Slingerland and Smith, 2004; Assine, 2005).

When an avulsion occurs, it will create an *avulsion belt* on the newly inhabited section of a floodplain, encompassing all the features of the avulsion process (Slingerland and Smith, 2004). Flow in a new avulsion belt is unconfined and large volumes of coarse-grained sandy sediment is deposited on top of finer-grained overbank deposits (Smith et al., 1989; Slingerland and Smith, 2004; Assine, 2005). An anastomosing planform is often present after the avulsion node before a dominant channel planform (i.e., meandering or braided) establishes and forms a larger main channel or channels (Smith et al., 1989; Assine, 2005; Makaske et al., 2012). This may be due to the slowing of channel aggradation processes which result in the replacement of anastomosing channels with a dominant single channel planform (i.e., meandering) (Smith et al., 1989).

Future avulsions are often influenced by the topography created by previous avulsions. For example, when an avulsion progrades, it changes the accommodation space within a basin by distributing sediment and leaving behind abandoned avulsion ridges which sit topographically higher than floodplain deposits (Jones and Schumm, 1999; Assine, 2005). It is also important to note that direct human influence on river systems can trigger avulsions through, for example, the regulation and/or diversion of flow, and engineering of a channel (Heyvaert and Walstra, 2016).

Understanding avulsion processes and deposits can also have important implications for rock record exploration as these large sandy deposits can be useful for hydrocarbon reservoirs (Slingerland and Smith, 2004). Additionally, the occupation and abandonment of a river on a floodplain can also lead to the development of soils necessary for agriculture (Smith et al., 1989; Slingerland and Smith, 2004). However, most importantly, avulsions can pose major hazards to large populations resulting in mass displacement and loss of human life, as well as damage to critical infrastructure (Slingerland and Smith, 2004; Heyvaert and Walstra, 2016). The avulsion of the Kosi River (India/Nepal) in 2008, for example, demonstrated the huge impact that avulsions can have on society as many villages became inaccessible, much agricultural land was destroyed, and flooding affected around 3 million people (Chakraborty et al., 2010; Sinha et al., 2014).

1.1.3 Fluvial Planform

Within an alluvial channel, discharge and sediment load influence erosion and deposition processes which, in turn, control morphological change in a channel (i.e., channel pattern) (Weissmann et al., 2013; Rhoads, 2020). Frequent erosion and deposition processes in alluvial channels allow sediment to be scoured (i.e., from the channel bed and banks) and deposited within the channel, forming different channel patterns as changes in sediment load and discharge occur downstream within a channel (Schumm, 1985). It is important to distinguish between fluvial planforms and their deposits, as reservoir dimension, connectivity, and heterogeneity are influenced by the different migration styles of rivers (Hartley et al., 2015; Colombera et al., 2017).

Different planform types include meandering, braided, anastomosing, and straight channels (Figure 1.3) (Leopold and Wolman, 1957; Schumm, 1985; Makaske et al., 2012). Due to the scope of this study, braided, anastomosing, and straight rivers are not outlined in detail within this chapter. Meandering rivers are, however, explored in further detail below. It is important to note that braided and anastomosing rivers are multi-thread channels (i.e., channels are divided by bars and islands) and that meandering and straight rivers are

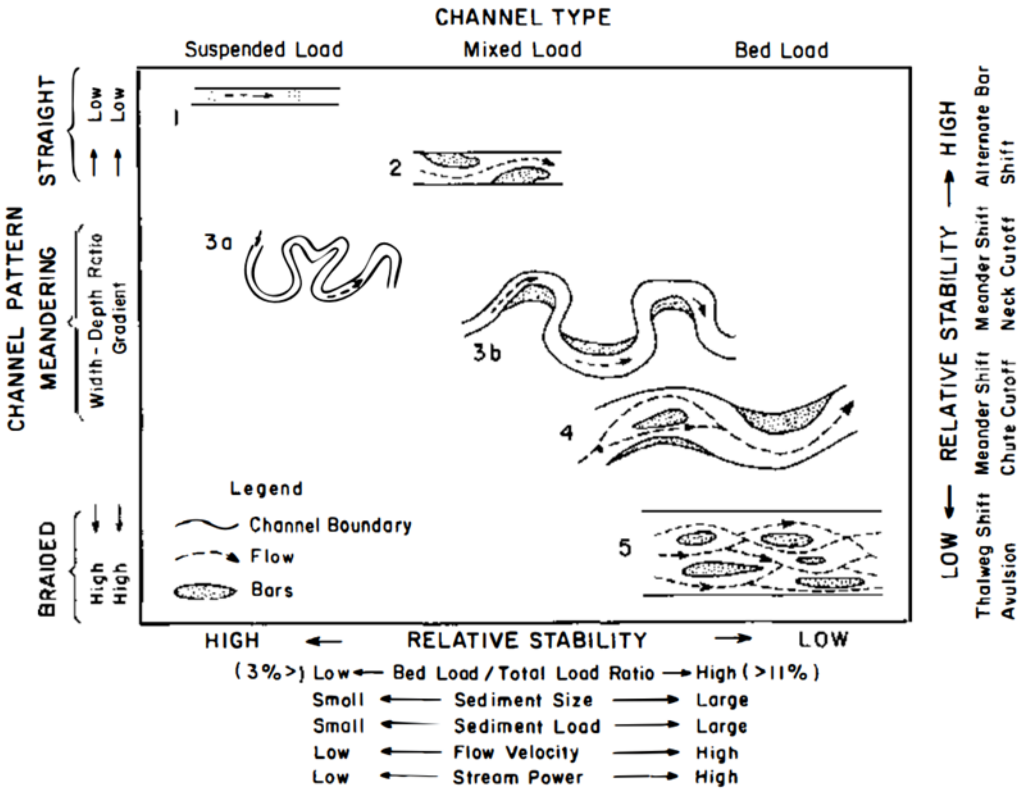

Figure 1.3. The formation of different river planforms based on sediment load, gradient, and the relative stability of the channel (Schumm, 1985).

dominantly single thread channels (i.e., one dominant channel) (Schumm, 1985; Gurnell et al., 2009). Meandering channels, however, have been known to experience *anabranching*, where a bifurcated channel rejoins the main channel downstream (Shukla and Rhoads, 2023). Although a dominant planform type will often exist across a river, it is important to note that these planforms are 'end members' and a continuum in planforms can exist between them (Leopold and Wolman, 1957; Callander, 1978; Gurnell et al., 2009).

Planform type is influenced by slope, sediment supply, and discharge (Figure 1.3) (Schumm, 1985). For example, braided systems often exist on steeper slopes (i.e., higher gradient slopes) than meandering systems, with higher sediment supply and variable discharge. Meandering systems however, develop on lower gradient slopes with lower sediment supply and more consistent discharge than braided rivers (Leopold and Wolman, 1957; Schumm, 1985; Hartley et al., 2010). Anastomosing rivers have been shown to form on floodplains with shallow gradients that have a very high sediment supply, often forming sediment islands within the channel (Leeder, 2009; Makaske et al., 2017). Straight channels often have low discharge and low sediment supply (Makaske, 2001).

1.1.4 Meandering Rivers

Meandering rivers are characterised by a series of reversing curves which migrate across floodplains in a distinctive manner and form point bar deposits along their course (Leopold and Langbein, 1966; Rhoads, 2020). The series of reversing curves that form a meandering river are referred to as a *meander train*; these make up a succession of sinuous waves over a space that can be measured by their wavelength and amplitude (Figure 1.4) (Callander, 1978; Seminara et al., 2001; Rhoads, 2020). The *wavelength* is the distance between the two bend apexes on the same side of the river and the *amplitude* is the distance between the apexes of two successive bends on the opposite side of the river (Güneralp and Marston, 2012; Rhoads, 2020). The individual curves are referred to as *meander bends* and the outermost point of a meander bend is known as the *apex* (Güneralp and Marston, 2012; Rhoads, 2020). The distance between the outer banks of each meander bend is known as the *meander belt* and the *inflection point* of the river is the point at which one bend changes into

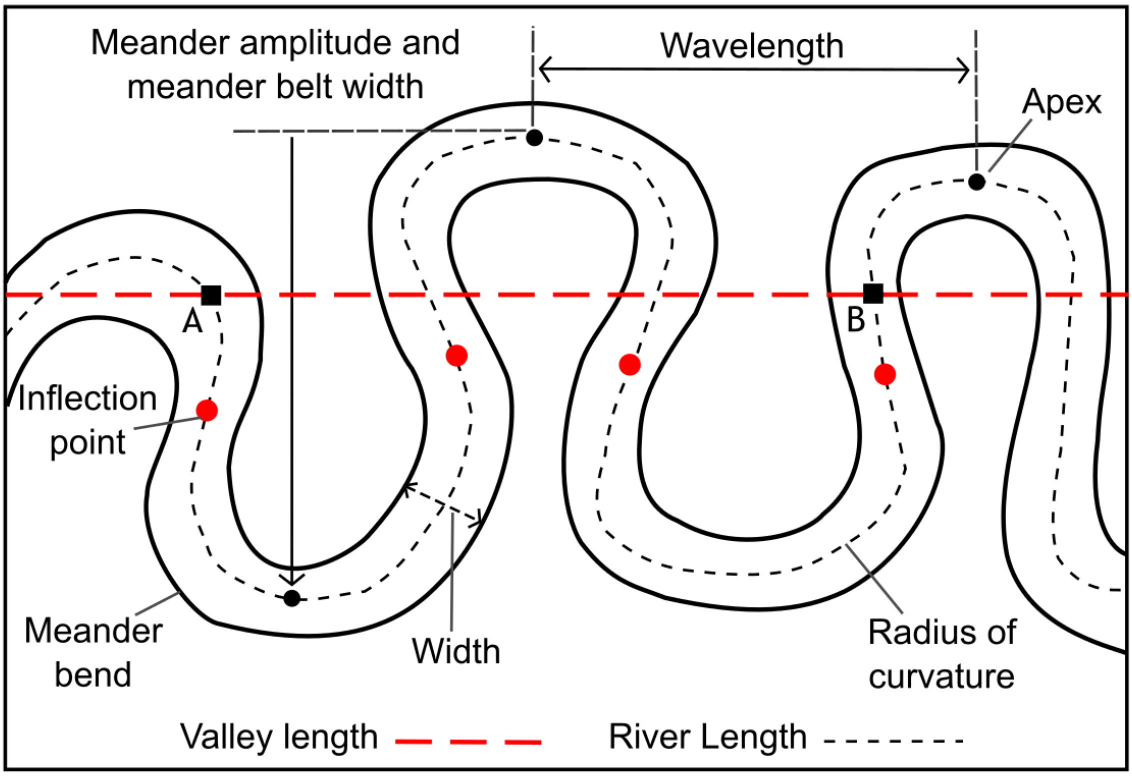

Figure 1.4. Meander terminology and features of a meandering river. Sinuosity is calculated between points A and B by dividing the river length (black dashed-line) by the valley length (red dashed-line). Inspired by Güneralp and Marston (2012) and Rhoads (2020).

another bend (Figure 1.4) (Inglis and Lacey 1947; Güneralp and Marston, 2012; Rhoads, 2020).

The measure of the curvature of a meandering river is known as *sinuosity*, which is calculated by dividing the length of the line that follows the deepest part of the river downstream (the thalweg) by the length of the valley (Figure 1.4) (Leopold and Wolman, 1957; Schumm, 1985; Wilzbach and Cummins, 2008). High sinuosity rivers have a sinuosity of > 1.5 (Wilzbach and Cummins, 2008) and straight rivers have a sinuosity of < 1.3 (Brice, 1964; Makaske, 2001; Assine, 2005). The sinuosity of a channel increases as meander bends grow; the evolution of a meandering river is detailed below.

Meandering rivers develop from initially straight channels that exist in an unstable state (Figure 1.5) (Yang, 1971; Rhoads, 2020). Laboratory experiments conducted by Friedkin (1945) identified that the initiation of a meandering planform within a straight alluvial channel is triggered by a disturbance within a channel, which results in the formation of a series of bends within the channel over time through processes of erosion and deposition. Inglis and Lacey (1947)

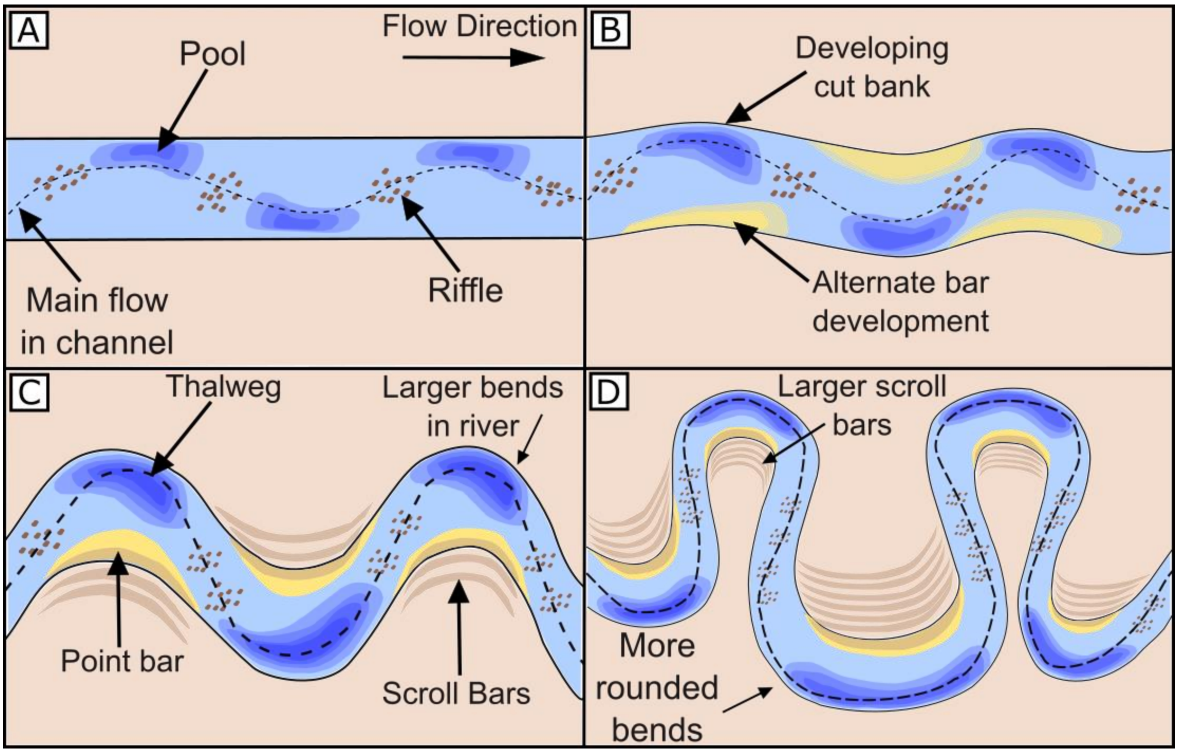

Figure 1.5. The initiation of a meandering river from an initially straight channel. A) straight river channel with pools and riffles forming due to oscillatory motion. B) small curves starting to form around pools on the outside bends of the river and alternate bars on the inside bends of the river. C) larger bends forming in the river as flow moves around point bars and erodes cutbanks, scroll bars start to develop. D) a more mature meandering river with large, rounded meander bends and scroll bar deposits on the inside of bends. Inspired by Rhoads (2020) and River Styles (2020).

and Leopold and Langbein (1966) found that an alluvial channel will try to reach a state of equilibrium in which the least amount of energy is used to carry sediment within a channel. These studies also found that a channel will naturally adjust its planform to a shape that requires the least amount of energy for water to flow within its banks, i.e., a meandering planform. Within a channel, there is an oscillatory motion of the flow that is understood to naturally adjust a channel from straight to meandering, however the reasons for this flow oscillation are still debated (Leeder, 2009; Rhoads, 2020).

Theories for the initiation of oscillation within a straight channel include: the reduction of different flow directions within the channel; an increase in channel slope resulting in less energy dissipation of the flow; and a reduction in stress of the water against the channel walls (Friedkin, 1945; Langbein and Leopold, 1966; Leeder, 2009; Rhoads, 2020). The oscillatory flow within the channel allows sediment to be scoured from channel banks and transported downstream where it is deposited upon a reduction in channel velocity and sediment transport capacity (i.e., at the inflection point of a meander bend) (Callander, 1978; Rhoads, 2020).

Leopold and Wolman (1957) found that within a straight channel, the thalweg would migrate across the channel and start to develop mud deposits on alternate sides of the channel which were typical of a meandering system. Over time, alternating areas of deep and shallow topography develop on the bed of a straight river, referred to as *pools* and *riffles* respectively (Leopold and Wolman, 1957; Leopold and Langbein, 1966; Yang, 1971; Bluck, 1971) (Figure 1.5). Yang (1971) attributes the formation of pools and riffles to dispersion and sorting processes within the channel. Leopold and Wolman (1957) and Yang (1971) found that pools are associated with the meander bends and that riffles form between bends in the river (i.e., the inflection point) (Figure 1.5).

Pools are the deepest part of the channel, which extend from the end of a bar unit further upstream and around the outside bend of a channel, usually reaching the lowest depth after the apex of the curve (Figure 1.5) (Bluck, 1971; Leeder, 2009; Rhoads, 2020). As the flow moves around the outside bend of the meander it will enter the pool and collect sediment as the channel is scoured (Callander, 1978). Sediment which is then transported within the flow of the channel is deposited as a riffle near the inflection point of the bend, where the channel is shallower and transport capacity reduces (Figure 1.5) (Friedkin, 1945; Callander, 1978; Wilzbach and Cummins, 2008; Rhoads, 2020). The upstream portion of the riffle is typically composed of coarser-grained gravels whereas the downstream portion of the riffle is typically composed of finer-grained sands (Bluck, 1971).

The development of pools and riffles within a straight channel is followed by the development of *alternate bars*. These alternate bars form as a result of the oscillatory flow in the channel depositing sediment on alternating sides of the channel downstream (Lanzoni, 2000a,b; Rhoads, 2020). An experimental study by Lanzoni (2000a,b) showed that flume channels with initially flat beds became unstable and started to develop alternate bars under a range of sediment sizes and flow conditions. Lanzoni (2000a,b) also showed that alternate bars in straight channels tend to migrate progressively downstream through time as sediment is transported through pools, across riffles, then onto bar tops, before being accreted into the moving bar front. Additionally, when immobile coarse material accumulates between the pool and alternate bar, the migrating bar unit can stabilise which is common when the bed material consists of mixed sand and gravel (Lanzoni, 2000a,b).

As these alternate bar units become stable, flow is forced around the bar which eventually leads to the formation of bends in the channel through further erosion and deposition processes (Figure 1.5) (Callander 1978; Rhoads, 2020). At the bankfull stage, where the river is at its highest discharge capacity before breaching its banks, the bars in the river do not have a large influence over the direction of flow as the water is too deep to be influenced by their topography (Friedkin, 1945; Rhoads, 2020). However, in low flow conditions the channel is usually influenced by bar-unit topography as flow can either travel around the bar or over the side of it into the pool of the next bar unit (Rhoads, 2020). The continued erosion and deposition processes eventually form the typical sinuous planform associated with meandering rivers. Erosion occurs on the outside bend of the meandering channel (concave bank) and deposition occurs on the inside bend of the channel (convex bank) creating bar units referred to as *point bars* (Friedkin, 1945; Wolman and Leopold, 1957; Leopold and Langbein, 1966; Nanson, 1980).

Point bar deposits are made up of mainly sandy material with some mud preserved between individual beds deposited during lower flow conditions (Wolman and Leopold, 1957; Willis and Tang, 2010). Coarser-grained sandy material is deposited on the side of the point bar closer to the channel bend apex with finer-grained sediment deposited on the downstream side of the channel bar (Willis and Tang, 2010). Laboratory experiments by Peakall et al. (2007) showed that point bars grow as they accrete onto bars migrating downstream, and through sediment settling out from suspension onto the bar unit. Peakall et al. (2007) also showed that the cohesion of the river's banks (i.e., by vegetation or fine-grained sediment) is an essential part of the preservation of the meandering planform. This cohesion must be strong enough to prevent the formation of a braided planform yet not so strong as to prevent planform migration. Ridges of finer-grained sediment called *scroll bars* can develop on point bars as suspended load is deposited on the point bar where the channel is shallower, and velocity is lower than the outer bend of the channel

(Nanson, 1980). Scroll bars follow the convex shape of the point bar and highlight migration of the point bar through accretion of scroll bars (Figure 1.5) (Nanson, 1980; Russell et al., 2018).

Opposite the point bar, on the outside bend of the river, is the *cut bank*, the fastest and deepest part of the river where erosion and scour occur (Bluck, 1971; Güneralp and Marston, 2012; Rhoads, 2020) (Figure 1.5). The fast flow and higher shear stress on the outer bend of the river has a greater capacity for erosion and allows the flow to carry more sediment (Güneralp and Marston, 2012; Leeder, 2009; Rhoads, 2020). Despite the frequent erosion processes observed in the outer banks of the meander, silt dominated concave deposits called *counter point bars* may form on this outer bend (Smith et al., 2009). Counter point bar deposits form directly downstream of point bar deposits, formed of finer-grained material than the point bar and following the concave shape of the outer meander bend (cutbank) (Smith et al., 2009; Hooke, 2023).

The cutbanks of the river are often steep as they are constantly being eroded and cut into, whereas the point bars are often more gently sloping towards the floodplains and the channel (Güneralp and Marston, 2012). Meandering rivers migrate through the erosion of the cutbank and the deposition of point bars on the inner bend (Leopold and Langbein, 1966). The width of the channel is often maintained through these processes of erosion and deposition as these tend to occur at the same rate (Wolman and Leopold, 1957).

Meander migration occurs frequently as meandering rivers often display unstable behaviour and migrate laterally over floodplains (Leeder, 2009; Güneralp and Marston, 2012; Rhoads, 2020). There are three main ways in which meandering rivers tend to migrate: expansion, translation, and rotation of meander bends (Figure 1.6) (Daniel, 1971; Ghinassi et al., 2014; Russell et al., 2018; Rhoads, 2020; Hooke, 2023). *Expansion* is the migration of the river in the opposite direction to the axis of the valley; the further the migration, the more sinuous the river will become (Figure 1.6) (Ghinassi et al., 2014). *Translation* is the movement of the river bend downstream in the same direction as the valley axis; this maintains the sinuosity of the river (Figure 1.6) (Ghinassi et al., 2014). *Rotation* is where the bend of the river curves in a circular manner reducing the symmetry of the meander bend (Figure 1.6) (Ghinassi et al., 2014). These migration patterns can be seen in rivers over space and time and often occur as a combination of these processes (Güneralp and Marston, 2012; Ghinassi et al., 2014).

Evidence of meander migration is recorded in the floodplains surrounding the river (i.e., through scroll bar accretion, meander cut-offs, and meander scars) (Güneralp and Marston, 2012; Russell et al., 2018). In planform, scrollbar migration is used to describe channel migration, as lateral accretion patterns of point bars show the growth of the meander bend over time (Russell et al., 2018). Meander cut-offs (Figure 1.6) can occur by either neck cut-off or chute cut-off, and may be partially complete in some cases (Callander, 1978; Micheli and Larsen, 2011; Rhoads, 2020; Hooke, 2023; Gao and Li, 2024). *Neck cut-off* (Figure 1.6) involves the river becoming more sinuous and allowing the two limbs of the meander bend to meet, whereas *chute cut-off* (Figure 1.6) involves the creation of a new channel between meander bends, which is formed via overbank flow creating a channel across the meander bend (Micheli and Larsen, 2011; Rhoads, 2020; Hooke, 2023; Gao and Li, 2024). Meander cut-offs reduce the sinuosity of the river and the length of the channel (Rhoads, 2020). The

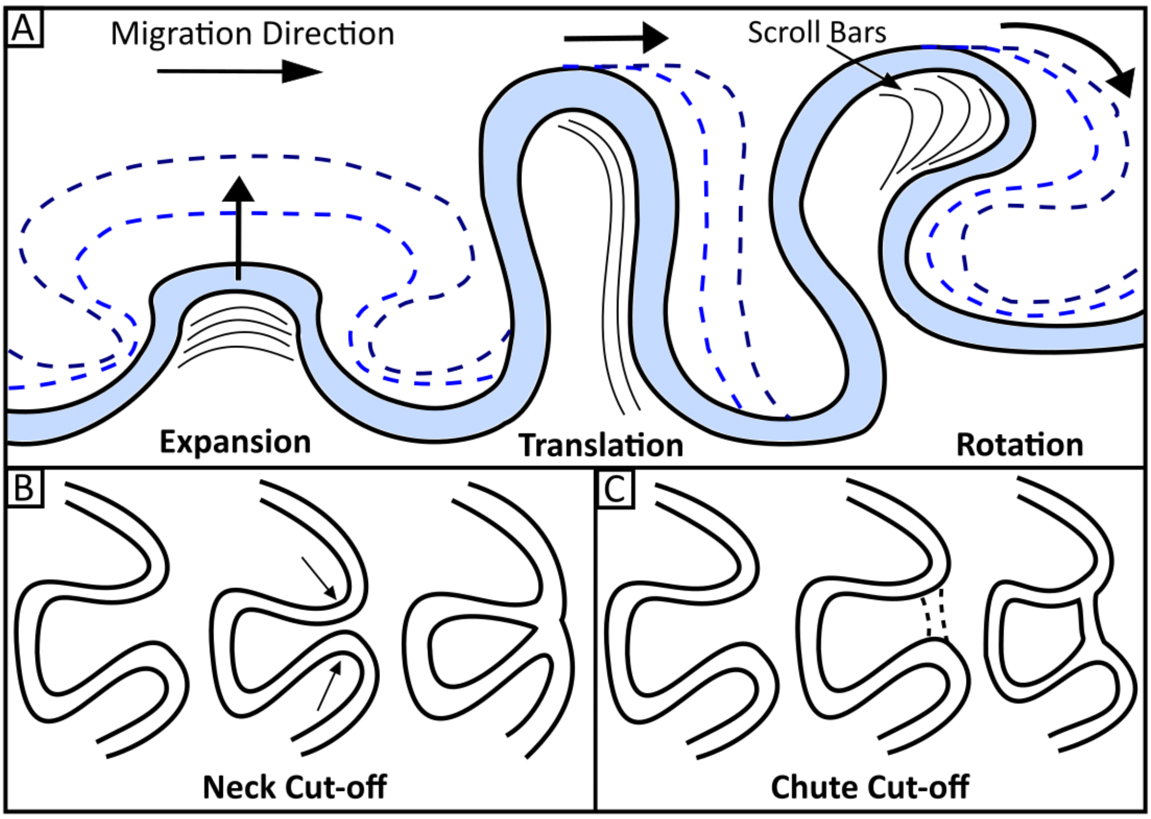

Figure 1.6. A) three types of channel migration experienced by meandering rivers. B) neck cut-off occurring when two meandering limbs intersect. C) chute cut-off when a channel forms over a meander bend. Inspired by Rhoads, 2020.

straightened section of the river will naturally readjust over time to become sinuous again (Rhoads, 2020).

Following a meander cut-off, a channel will typically experience a high amount of sedimentation, erosion, and changes in morphology as the channel widens and begins to form bars (Hooke, 2023). This initial, highly active phase, occurs over a 2 to 4 year period before the channel becomes more stable (Hooke, 2023). Hooke (2023) includes many examples of the highly active and sensitive nature of meandering systems as they are constantly adjusting to different influences such as changes in discharge and sediment supply at different scales (i.e., bar scale, bend scale, and reach scale (across several bends)).

At reach scale, meander bends are often able to respond individually to the same hydrological conditions thus highlighting the variability of natural systems as they respond to changes in erosion and deposition (Hooke, 2023). For example, at reach scale, Hooke (2023) found that some bends in the River Bollin (UK) experienced more erosion and deposition than others, and experienced changes in width and shape over a two decade period. Similarly, in the Powder River in Montana, USA, Hooke (2023) found that channel bank erosion was highly variable both spatially and temporally, which may be the result of vegetation within channel banks. This is due to the cohesive strength that vegetation offers as vegetated banks are often able to withstand greater amounts of erosion (Hooke, 2023).

Hooke (2023) also found that flood events can have a significant impact on a river. For example, a 1978 flood on the Powder River resulted in a greater amount of morphological change than in the previous 37 years of smaller magnitude floods, and this was in addition to a 53% decrease in channel width and a 29% increase in channel sinuosity between 1939 and 2013 (Hooke, 2023). This work by Hooke highlights that changes within meandering rivers can be highly individual and can relate to a variety of different factors, which include but are not limited to the stability of channel banks at different reaches of a river (i.e., where vegetation increases bank resistance). Hooke (2023) also found that channel stability is strongly related to the gradient of the channel, with stable reaches of a river often existing on lower gradient slopes than reaches of the river which experience increased meander growth on higher gradient slopes.

1.1.4.1 Deposits of Meandering Rivers in the Rock Record

In modern imagery, meandering rivers have been observed as a dominant planform type in sedimentary basins and are therefore hypothesised to be more dominant than originally perceived in the subsurface (i.e., the rock record) (Hartley et al., 2015). The characteristics of meander deposits should therefore be explored further to understand their reservoir potential, for example (Swan et al., 2018). Difficulties in identifying deposits of meandering rivers in the rock record have led to the assumption that braided fluvial systems dominate the rock record, which may not be the case (Hartley et al., 2015).

The deposits of braided and meandering fluvial systems have differences in terms of sandstone body shape, dimensions, heterogeneity, and deposit connectivity (Hartley et al., 2015; Swan et al., 2018). Sandstone bodies deposited by meandering systems are understood to be: relatively small in size, isolated or poorly connected in subsurface, and highly heterogeneous in terms of sand and mud deposits (Hartley et al., 2015). Sandstone bodies deposited by braided systems, in comparison, are understood to be laterally extensive, amalgamated, and sheet-like with little internal heterogeneity (Hartley et al., 2015, Swan et al., 2018).

Braided deposits have been found to contain large volumes of gravel, with trough cross-bedding and migration downstream in the same direction as paleoflow (Swan et al., 2018). Meandering deposits, however, show fining upward sequences with coarse-grained material at the base of the bar changing into finer material towards the top of the bar (Swan et al., 2018). These bar units consist of inclined packages of heterolithic material (Swan et al., 2018).

Early studies of meander deposits (i.e., Visher, 1960) identified depositional sequences present in many sandstones which included: trough cross-bedding at the base, followed by current lamination above, then symmetrical ripples (of a finer grain size), and finally laminates of clay and fine sand at the top (deposited from suspension). These sequences are understood to represent a decrease in energy as finer grains are deposited with less sorting upwards in a point bar (Visher, 1960). This decrease in energy is due to the slow outward movement of the pool within the channel as lateral migration occurs, therefore decreasing water depth over the bar unit and decreasing bed shear stress (Visher, 1960, Johnston and Holbrook, 2018; Liu et al., 2020).

Braided and Meandering deposits share similar features when studied at outcrop scale such as the presence of trough cross-bedding and stratification (Swan et al., 2018). However, Hartley et al. (2015) identified that fining-upward sequences which are typical to meander deposits are not always well-developed. Therefore features which can be present in coarse-grained braided and meandering systems (i.e., cross-strata, erosion surfaces within deposits, and mud-stone intraclasts), lead to difficulty in differentiating between these deposits in the rock record (Hartley et al., 2015).

Similarly, previous misinterpretations of meandering systems in the rock record may have been influenced by the belief that meandering rivers did not occur before the development of vegetation as they were unlikely to form on unvegetated dry land (i.e., arid environments) (Santos et al., 2019). New research, however, suggests that meandering rivers are common in arid environments and that there is a higher preservation of meandering planforms in the pre-vegetated rock record than previously believed (Santos et al., 2019). For example, the ancient Salt Wash DFS in Utah, USA, has previously been interpreted as braided, however the use of high-resolution satellite imagery in recent studies by Hartley et al. (2015) and Swan et al. (2018) have recognised exhumed point bar deposits in the proximal to medial portions of the DFS.

This study, as will be outlined below, will contribute important spatial data on meander deposits within a modern DFS. Due to the abundance of meander deposits in the rock record, identifying spatial trends in meander characteristics is relevant to understanding sandstone body dimensions under different conditions. For example, channel width and sediment transport capacity decrease downstream on a DFS, therefore the size and shape of meander deposits will also decrease. This will have important implications for the understanding of meander deposit size and shape in the subsurface (i.e., for hydrocarbon reservoir purposes).

1.2 Aims and Objectives

It is understood that predictable downstream changes in channel size are present in tributary and distributary systems (Weissmann et al., 2010). Therefore, it is expected that there will be similar systematic changes in meander characteristics downstream, resulting in a variation in meander characteristics within a predictive framework. Previous work regarding downstream trends of meander characteristics is limited, mainly focusing on meanders in isolation (i.e., exhumed meander deposits (e.g., the ancient Salt Wash DFS, Utah; Hartley et al., 2015 and Swan et al., 2018, and the Scalby Formation, Yorkshire, UK; Ielpi and Ghinassi, 2014)). Additionally, modern studies of meander characteristics (i.e., Russell et al., 2018) provide important quantification of meander deposit characteristics over a range of examples at reach scale. However, more research is required on how these meander characteristics vary within a spatial context (i.e., across a single river system or depositional basin) (Owen et al., 2015).

The understanding of the spatial variability of meander deposits has important implications for sandstone-body reservoir dimensions, which are important for the extraction of resources (i.e., water), or for carbon capture and storage (CCS). In addition, this work has implications for the understanding of the subsurface connectivity of sandstone bodies, which are able to transport fluids which may contain pollutants. This work will also contribute to the quantification of a modern DFS model, which has important implications for modern geomorphic processes (i.e., avulsions), and the distribution of water and sediment within a sedimentary basin.

This study aims to understand the spatial variability of fluvial characteristics (i.e., channel width, channel belt width, meander deposit size, and sinuosity) in a modern meandering DFS, and more precisely, to understand whether there is a change in meander characteristics (i.e., meander deposit dimensions) downstream. Additionally, this study aims to understand the impact that an avulsion event can have on a parent channel (i.e., the active channel) in terms of changes in channel width, channel belt width, meander deposit size, and sinuosity. The hypothesis of this study is that channel size will decrease downstream resulting in a decrease in channel belt width and meander deposit dimensions (area, length, and width), and that sinuosity will be variable.

The objectives of this study are:

1) To quantify spatial changes in active channel width, active channel elevation and slope gradient, active channel belt width, channel belt width, active meander deposit dimensions, abandoned meander deposit dimensions, and active channel sinuosity at system scale (from apex to toe of the Taquari DFS), and across proximal, medial, and distal DFS zones, using satellite imagery from 2022.

2) To compare active channel width and sinuosity directly between 1985 (pre-avulsion) and 2022 (during-avulsion) using satellite imagery from each year, respectively, to understand temporal changes which have occurred in the Taquari DFS since the initiation of the Caronal avulsion (i.e., between 1996 to 1997).

3) To compare changes in active channel width, active channel elevation and slope gradient, active channel belt width, channel belt width, active meander deposit dimensions, abandoned meander deposit dimensions, and active channel sinuosity upstream and downstream of the Caronal avulsion point to understand the impact of the avulsion on these variables.

4) To create a dataset on a modern DFS in which active and abandoned meander deposit dimensions are quantified spatially (i.e., from apex to toe of a DFS) to understand variations in deposit dimensions downstream on a DFS.

1.3 Study Area

The Taquari DFS, also known as the Taquari Megafan, was chosen as a study area as it is a well-documented distributive fluvial system with a dominantly meandering planform (Assine, 2005). In addition, it has experienced no significant human engineering on the banks or in the channel (i.e., dams), allowing for the study of the natural system. As the Taquari is such a large system, it gives an ideal opportunity to study meandering rivers in a spatial context, therefore increasing the understanding of how meander characteristics change downstream from proximal to distal zones of a DFS. The Taquari DFS is also experiencing a large avulsion where discharge is diverted to the avulsed channel and the parent channel experiences slow abandonment. This provides an opportunity to study the impact of decreasing discharge and sediment load on meander characteristics (i.e., deposit dimensions) downstream on a DFS.

The Taquari DFS is located within the Pantanal Basin, an active sedimentary basin in the Mato Grosso do Sul state of west-central Brazil, South America. The Pantanal is an important wetland environment that hosts a variety of plant and animal species and a diverse range of vegetation (Assine, 2005; Hartley et al., 2010; Louzada et al., 2023). The Taquari DFS is the largest in a series of large DFS within the Pantanal basin which are fed by rivers from mountains to the east of the basin (Assine, 2005) (Figure 1.7). The Taquari DFS reaches the south-flowing axial Paraguay Fluvial System on the western margin of the basin which collects water and sediment from the Taquari DFS (Figure 1.7) (Assine, 2005; Porsani et al., 2005; Zani et al., 2012; Ivory et al., 2019).

The Pantanal Basin is Cenozoic in age and is tectonically active with its formation thought to be associated with forebulge extension during the formation of the Andes Mountain range (Porsani et al., 2005; Buehler et al., 2011; Assine et al., 2016). As a result of ongoing Quaternary tectonic activity, subsidence is common in the basin due to faulting which causes depressions and accommodation space creation where flooding is frequent (Assine, 2005; Assine et al., 2016). The basement rocks of the Pantanal Basin are Neoproterozoic magmatic and low-grade metamorphic rocks (Zani et al., 2012). In the drainage basin of the Taquari DFS, the river is incised into sandstones from the Palaeozoic (Assine, 2005; Buehler et al., 2011; Zani et al., 2012). Deposits on the DFS itself are Pleistocene in age and were deposited in an arid climate before the Late

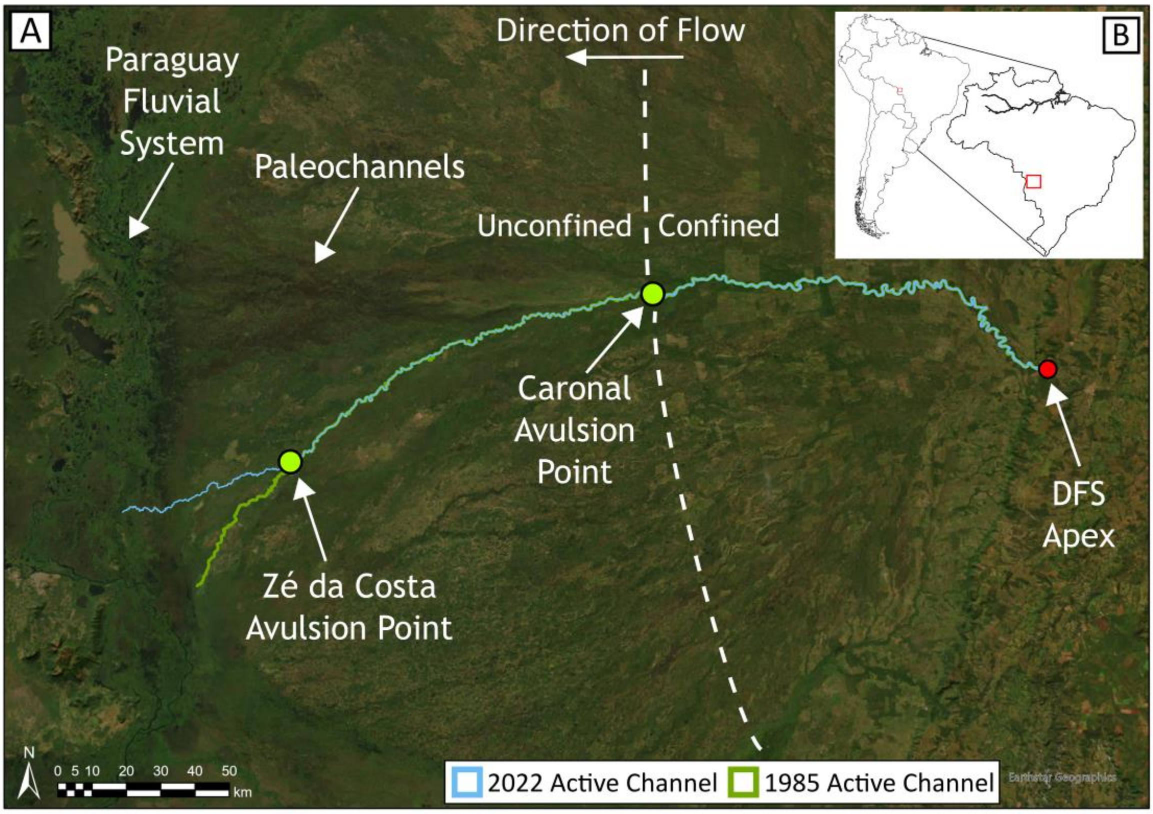

Figure 1.7. Reference map for the Taquari distributive fluvial system (DFS), Brazil, South America, using satellite imagery from 2022. The position of the Caronal and Zé da Costa avulsion points on the 2022 active channel are highlighted by green marker points. Although the 1985 channel is mapped using imagery from 1985, it is present on this map as a reference. Paleochannels can be seen to the north of the active channel. The Paraguay Fluvial System truncates the Taquari DFS on its western margin. The Caronal avulsion point also marks the boundary between the confined portion of the DFS (upstream of the avulsion point), and the unconfined portion of the DFS (downstream of the avulsion point).

Pleistocene/Holocene transition resulted in climate warming and the formation of a more tropical, humid, wetland environment (Assine, 2005; Assine et al., 2016).

The Pantanal wetland is the biggest tropical wetland in the world at around 130,000 km^2 to 140,000 km^2 (Assine, 2005; Buehler et al., 2011; Porsani et al., 2005; Ivory et al., 2019). The average rainfall of the area is around 1000 mm yr^{-1} (Ivory et al., 2019). Flooding mainly occurs during the wet season from December to March (Assine et al., 2005; Porsani et al., 2005; Buehler et al., 2011). As the area is generally topographically low, the lowland areas drain very poorly resulting in some areas of the wetlands remaining saturated year-round, including during the dryer months from July to September (Buehler et al., 2011; Assine et al., 2015). Flooding in the Paraguay River, along the west margin of the basin, increases water supply to the wetland increasing the saturation in distal portions of the Taquari DFS (Ivory et al., 2019).

The Taquari DFS makes up around 37% of the Pantanal area and is around 50,000 km^2 (Assine, 2005; Porsani et al., 2005). The apex of the DFS is at the highest altitude (~190 m in elevation) to the east of the basin with the toe at the lowest altitude (~85 m in elevation) to the west of the basin where it is truncated by the Paraguay Fluvial System (Zani et al., 2012). The average gradient is around -0.36 m/1000 m (Assine, 2005; Porsani et al., 2005; Zani et al., 2012) and the length of the DFS from apex-to-toe is around 250 km (Buehler et al., 2011). The Taquari DFS forms a large fan-shaped distributive fluvial system (Figure 1.7) with a dominantly meandering planform, although some distal portions of the DFS have an anastomosing planform (Assine, 2005; Porsani et al., 2005).

Geomorphic features of the Taquari DFS include paleochannels from previous avulsions of the river, relict point bar deposits, oxbow lakes, and abandoned avulsion lobes (Figure 1.7) (Buehler et al., 2010; Makaske et al., 2012; Assine et al., 2016). The active meandering channel belt of the Taquari DFS contains active point bars and sandy channel levees (Assine, 2005). Within the DFS, two distinct geomorphologic zones exist, one in the upper DFS, and one in the lower DFS (Assine, 2005; Buehler et al., 2011; Porsani et al., 2005). The Caronal avulsion point marks the boundary between these two geomorphologic zones, where the active channel is confined upstream of the avulsion point and then unconfined downstream of the avulsion point (Figure 1.7). The active channel is incised for the first ~100 km of the upper DFS where a 3 km to 5 km wide confined meander belt is created by the single meandering channel which is entrenched in Pleistocene sediment from previous DFS lobes (Assine, 2005; Porsani et al., 2005; Buehler et al., 2011). Avulsion processes in the upper DFS are hindered by the depth of the river incision in this area (Assine, 2005; Porsani et al., 2005; Buehler et al., 2011).

Downstream of the confined portion of the DFS, an intersection point exists where flow on the DFS becomes unconfined and the modern zone of deposition is present (Assine, 2005; Porsani et al., 2005; Weissmann et al., 2010; Buehler et al., 2011; Louzada et al., 2020). Where flow becomes unconfined, the river is able to avulse and prograde over a larger area on the DFS surface, therefore depositing large volumes of sediment on floodplains during large flood events or via crevasse splay progradation (Porsani et al., 2005). As flow is dispersed over the DFS, river discharge decreases downstream, and the river becomes narrower and shallower (Assine, 2005). As discharge and stream power decrease downstream, inactive portions of the DFS preserve geomorphic features such as avulsion lobes as no active sedimentation takes place in this portion of the DFS (Assine, 2005; Zani et al., 2012).

Two significant avulsions have occurred within the Taquari DFS within the last 35 years known as the Zé da Costa and Caronal avulsions (Figure 1.7) (Assine, 2005). The Zé da Costa avulsion occurred between 1988 and 1998 (stabilising in 1999) and occurred in the distal portion of the DFS where a complete abandonment of the parent channel was observed as the channel shifted position on the DFS surface (Assine, 2005; Louzada et al., 2020). The distal area of the DFS which was abandoned following the Zé da Costa avulsion has now become a much drier area of the DFS that mainly receives water from flooding in the Paraguay River (Louzada et al., 2020). The flow of water to this section of the DFS has also been reduced due to diversion of flow upstream by a much larger avulsion known as the Caronal avulsion (Figure 1.7) (Louzada et al., 2020).

The Caronal avulsion initiated between 1996 to 1997 when crevasse splays formed close to the modern zone of deposition (i.e., the intersection point between the confined and unconfined portions of the DFS) with one splay stabilising in 2004 and forming the main avulsion channel (Buehler et al., 2011; Assine et al., 2015; Louzada et al., 2021). The Caronal avulsion is still ongoing with most of the flow being diverted to the avulsed channel and a small portion of the flow still feeding the parent channel (Figure 1.7) (Louzada et al., 2021). The Caronal avulsion is much larger and longer lasting than the Zé da Costa avulsion and is responsible for widespread sediment and water distribution to the north of the basin (Louzada et al., 2021). The full impact of this avulsion will not be understood until it is complete.

Paleochannels observed in satellite imagery show previous avulsions that have occurred on the Taquari DFS (Figure 1.7) (Assine, 2005). Avulsion processes and channel progradation have become more frequent on the Taquari DFS and the Pantanal wetland as a whole. This is due to climate change and unsustainable land use practices which increase flooding, and mobilise loose soil and sediment from the catchment area which then enters the Taquari DFS (Assine, 2005; Louzada et al., 2020). Due to the scale of the Taquari DFS, much of the research conducted on this system is done using satellite imagery. This study, as will be outlined in the following Methods chapter, uses similar data collection techniques to conduct the spatial analysis of the Taquari DFS.

2 Methods

To conduct a spatial analysis on the Taquari Distributive Fluvial System (DFS), satellite imagery from 1985 and 2022 were used in ArcGIS Pro to map features of the meandering system at different points in time (Figure 2.1). Firstly, channel width and sinuosity alone were measured on the 1985 DFS due to the limited resolution of the 1985 imagery. Then, channel width, sinuosity, active channel belt width, channel belt width, active and abandoned meander deposit dimensions (area, length, and width) were measured on the 2022 DFS. A digital terrain model (DTM) from 2022 was used to calculate the elevation and slope gradient of the 2022 active channel.

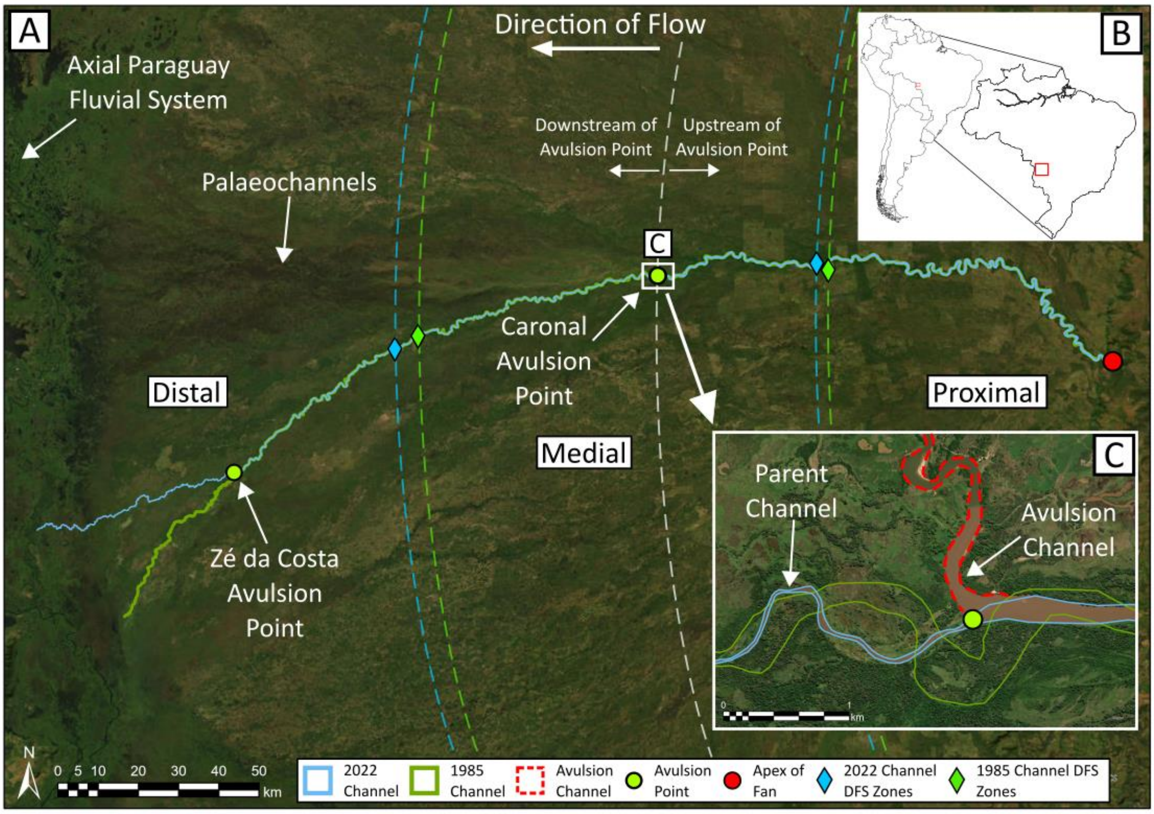

Figure 2.1. A) an overview map of the 2022 Taquari DFS, Brazil, South America (B), with the Caronal avulsion point (C) and Zé da Costa avulsion point further downstream. DFS zones (proximal, medial, and distal) for the 2022 and 1985 systems are highlighted by the blue and green dashed lines, respectively. The white dashed line separates upstream and downstream reaches of the Caronal avulsion point. Inset C shows the Caronal avulsion point where flow is diverted from the 2022 parent channel to the avulsed channel. The difference in size between the 2022 channel (blue) and the 1985 channel (green) can be seen in inset C as discharge decreases in the 2022 channel downstream of the Caronal avulsion point. Although the 1985 channel polygon appears on this satellite image from 2022, it was mapped using imagery from 1985.

This comparison between the 1985 and 2022 Taquari DFS outlines changes that have occurred temporally on the Taquari DFS since the initiation of the Caronal avulsion (between 1996 to 1997) (Assine, 2005; Buehler et al., 2011). Following the initiation of the avulsion, flow in the main active channel (parent channel) has continued to be diverted to the avulsed channel therefore resulting in a decrease in discharge in the parent channel. The methods outlined below describe how the spatial and temporal analysis of the Taquari DFS was conducted to quantify downstream changes in meander characteristics across the 1985 and 2022 Taquari DFS.

Channel width and sinuosity data from the 1985 DFS, and channel width, elevation and slope gradient, channel belt width, meander deposit dimensions, and sinuosity data from the 2022 DFS are collected across the whole system (from apex to toe of the DFS) and then split into proximal, medial, and distal DFS zones (Figure 2.1). As there is currently no other proposed method of splitting a DFS into each zone (Williams, 2023), the DFS is split into equal thirds. This involves splitting the centrelines of the 1985 and 2022 channel polygons into equal thirds representing the proximal, medial, and distal DFS zones. The 2022 system was also split upstream and downstream of the Caronal avulsion point to measure changes in meander characteristics where the discharge in the active channel reduced downstream of the avulsion point (Figure 2.1). The 1985 system was not split at the Caronal avulsion point as it pre-dated the initiation of the avulsion.

Channel width, elevation and slope gradient, channel belt width, meander deposit dimensions, and sinuosity data were collected in ArcGIS Pro and then exported to Excel for processing while additional statistical analyses were conducted in Minitab. Graphs from Excel are exported to Inkscape for annotation; Inkscape is also used to create all diagrams and figures. All data are rounded 2 decimal places except for R^2 values which are rounded 4 decimal places to reflect the smaller R^2 values observed for some variables. It was decided that the DTM data (outlined further in section 2.6) would also be rounded 2 decimal places as this is appropriate for the precision of this data. The following section provides more detail on the precision of satellite data in relation to the use of 2 decimal places when presenting data.

This chapter firstly outlines how satellite imagery was acquired and then used to collect data across the 1985 and 2022 Taquari DFSs. This chapter then details how the active channel, active channel belt, channel belt, active meander deposits, and abandoned meander deposits were identified using the satellite imagery and how measurements for each of these variable were taken downstream. Finally, this chapter outlines how sinuosity was calculated using the active channel polygon and how elevation and slope gradient were extracted from a digital terrain model (DTM).

2.1 Satellite Imagery

All measurements are taken from the ArcGIS Pro World Imagery basemap from 2022. Georeferenced Landsat5 imagery from 1985 and Sentinel2 imagery from 2022 are loaded into ArcGIS as layers and used as reference maps, so that channel features can be traced. The high-resolution basemap (0.3 m resolution) can produce data with up to 12 decimal places. However, for clarity and consistency, it was decided that 2 decimal places appropriately reflected the spatial resolution of the World Imagery basemap.

Landsat5 imagery from June to August 1985 was used to map the active channel before the initiation of the Caronal avulsion. These dates were chosen as they represent the oldest imagery available for the region. Satellite imagery was filtered for the months of June to August where the river experiences normal flow conditions (i.e., no flooding) (Buehler et al., 2011, Ivory et al., 2019). The Landsat5 imagery is 30 m resolution which allows for the mapping of the active channel. However, channel belt and meander deposit measurements could not be mapped at this resolution. The lowest measured channel width for the 1985 channel is ~54 m (in the distal reaches of the DFS) which was still visible using the 30 m resolution imagery. To aid with the mapping of the 1985 channel, the red, green, and blue (RGB) values of the Landsat imagery were changed to band 5 (shortwave infrared), band 3 (red) and band 2 (green) respectively, as this made the wetted channel appear bright blue against a red landscape.

ArcGIS Pro World Imagery from 2022, along with Sentinel2 imagery from June to August 2022 was used to map the active Taquari system using modern imagery. RGB values for the Sentinel2 imagery were changed to band 8 (near infrared), band 3 (red) and band 2 (green). ArcGIS imagery was used along with the Sentinel2 imagery as it is a much higher resolution (0.3 m resolution) than the Sentinel2 imagery (12 m resolution). ArcGIS World Imagery provides up to date, high resolution imagery from a variety of sources in order to display images with little to no cloud cover (Esri, 2024). This allowed for more detailed measurements where the channel width reduced significantly into distal DFS reaches where the 12 m resolution Sentinel2 imagery was not suitable to map the channel where the width was ~ 15 m.

Although the high resolution of the ArcGIS imagery is useful in interpreting the finer-detailed DFS features, this imagery represents a collection of tiles displaying the best imagery available (i.e., low cloud cover imagery (Esri, 2024)) over different time periods. This can often result in discontinuity across tiles as two adjoining tiles may show a different flow regime of the river system, where channel width is larger in one tile than the other. This was not a large concern, however, as any difference in channel width observed between tiles was on the scale of a few metres and would not largely skew the data. In addition to the ArcGIS imagery, Bing Maps, Google Earth Timelapse Tool, and Google Earth were used to aid interpretations across the 1985 (Google Earth Timelapse Tool only) and 2022 DFS. This additional imagery revealed DFS features, such as channel bifurcations and abandoned meander deposits, which were more clearly seen using different imagery.

2.2 Channel Width

Channel width was measured the same way for the 1985 channel and the 2022 channel. Firstly, the dominantly active channel was identified which is defined as the wetted portion of the river where water flows and no vegetation is present (Boothroyd et al., 2021). The channel with the highest discharge downstream was followed as many bifurcations occur downstream on both channels. For the 1985 channel there is one clear channel downstream which can be followed to the distal reaches of the DFS, however, in the 2022 system there are two active channels due to the Caronal avulsion: a parent channel and an avulsion channel.

The parent channel (2022 active channel) is currently in the process of abandonment as flow is diverted to the Caronal avulsion channel (Figure 2.1). However, it was decided that the parent channel would be mapped instead of the avulsion channel as the avulsion channel is still establishing a main active channel and has many bifurcations which are difficult to follow. Additionally, the parent channel has been stable for decades with a defined channel from apex to toe of the DFS which allows direct comparisons of channel width between the 1985 channel and the 2022 channel. Both channels follow the same course downstream on the DFS until the Zé da Costa avulsion point (Figure 2.1) where the channel changed position on the DFS in 1998 (Assine, 2005; Buehler et al., 2011).

To measure channel width downstream on the DFS, a polygon was drawn manually around the wetted portion of the active channel on ArcGIS Pro following the channel with the highest discharge downstream when bifurcation points were encountered. Using the 'Polygon to Centreline' tool, a centreline running through the centre of the polygon was created. The centreline was then split at the Caronal avulsion point (for the 2022 channel only), using the 'Split Line at Point' tool (using a point created at the avulsion point) before being smoothed to account for width changes upstream and downstream of the avulsion point. The 1985 channel was not split before being smoothed as the width decrease downstream was more consistent.

To measure width downstream within the channel, firstly, the centreline of the channel polygon was smoothed so transects could be generated at an appropriate perpendicular angle to the channel centreline for more accurate width measurements (this removed sharp edges and reduced the skew of the transects) (Figure 2.2). Secondly, points were generated along the centreline every 2% downstream; these acted as markers for the transects to be generated. Thirdly, the centreline was split at the 2% marker points using the 'Split Line at Point' tool so transects could be generated at the start and end of each individual line segment using the 'Generate Transects Along Lines' tool and selecting the 'Generate transects at start and end of line' option. Finally, the channel polygon was split, using the transects as traces, by drawing a line over them using the 'Split' tool on the 'Edit' tab in ArcGIS Pro. Using the area between the transects and the length of the split centreline between the transects, mean width was calculated at these intervals downstream by dividing the area of each section by the length of the centreline in each section (area / length = mean width) (Figure 2.2). This reduced bias in the data collection as the width downstream was taken as an average instead of as a single point downstream.

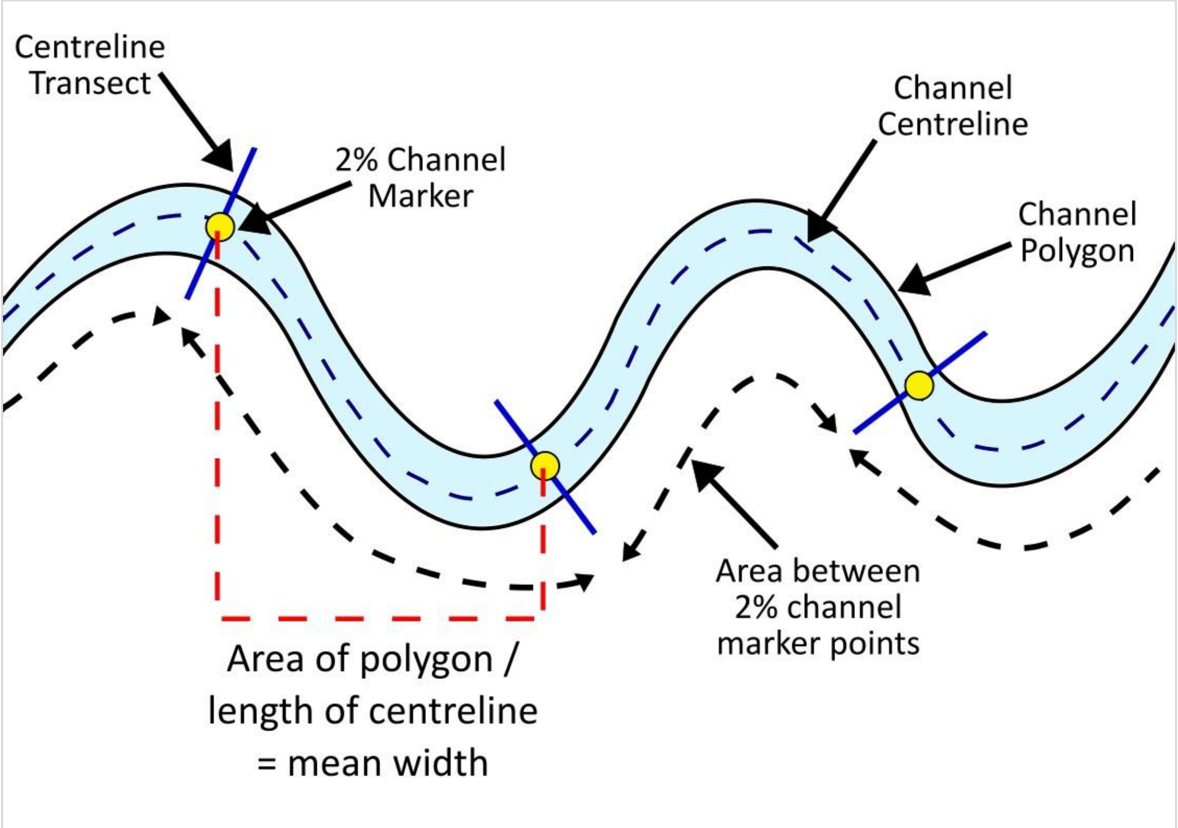

Figure 2.2. Diagram showing how mean width is calculated downstream along a polygon. 2% channel markers are created downstream along the channel's centreline to calculate mean width between these points. Transects are created at each 2% marker point perpendicular to the channel centreline for more accurate width measurements between marker points. The channel polygon and centreline are split at 2% channel marker points, using the transects as a trace to split the polygon, and mean width is calculated by dividing the area of the polygon between the marker points by the length of the centreline between the marker points (mean width = area/length). The red dashed line represents an example where mean width would be calculated between these marker points.

2.3 Channel Belt Width

An active channel belt is defined as the area within which the active channel migrates (Hartley et al., 2018; Nyberg et al., 2023). As a channel migrates it creates a channel belt reflecting the migration capacity of the channel, i.e., larger channels will have a higher discharge and sediment supply and will be able to migrate further across the DFS surface depositing material. Deposition in the active channel belt can be considered as overbank deposits (i.e. outside the channel form), however, preservation potential is limited as the river repeatedly migrates and avulses within the channel belt.

On satellite imagery from 2022, two separate channel belts are identified on the Taquari DFS: the active channel belt and the channel belt. The 1985 DFS does not have a mapped channel belt as the imagery was not suitable for measurements of this detail. The active channel belt and the channel belt are only differentiated in areas where there are clear differences in channel belt width observed in satellite imagery. For example, due to the initiation of the Caronal avulsion (1996 to 1997), the 2022 active channel has a significantly lower discharge than it did previously downstream of the avulsion point. This has resulted in a significant decrease in the migration rate of the active channel, therefore, an active channel belt is created which is much smaller in size than it is upstream of the avulsion point (Figure 2.3C).

A significantly larger channel belt is also observed in satellite imagery downstream of the Caronal avulsion point, which could not have been created by the 2022 active channel in this location due to the evident mismatch in size between the 2022 active channel and the significantly larger channel belt (Figure 2.3C). It is clear that the larger channel belt downstream of the Caronal avulsion point reflects the migration capacity of a significantly larger pre-avulsion channel instead of the 2022 active channel, which is much smaller in size and therefore has a lower migration capacity (Figure 2.3D). The channel belt is then defined as the area within which the active channel migrated before the initiation of the Caronal avulsion (i.e., pre-1996). This channel belt includes abandoned meander deposits and bifurcations that rejoin the river downstream.

Upstream of the Caronal avulsion point, the active channel belt and the channel belt are the same width as there has been no change in discharge associated with the Caronal avulsion due to this portion of the DFS being upstream of the avulsion point. Similarly, downstream of the Zé da Costa avulsion point, in the distal DFS zone, there is no differentiation between active channel belt width and channel belt width as the Zé da Costa avulsion (1988 to 1998) changed the position of the channel in this location before the initiation of the Caronal avulsion. Following the Zé da Costa avulsion, a single dominant meandering channel took many years to establish as an anastomosing planform was initially present following the avulsion. Once the single sinuous channel was established in this distal DFS reach, the active channel belt created by this channel reflected the reduced migration capacity of the channel. Therefore, there is no

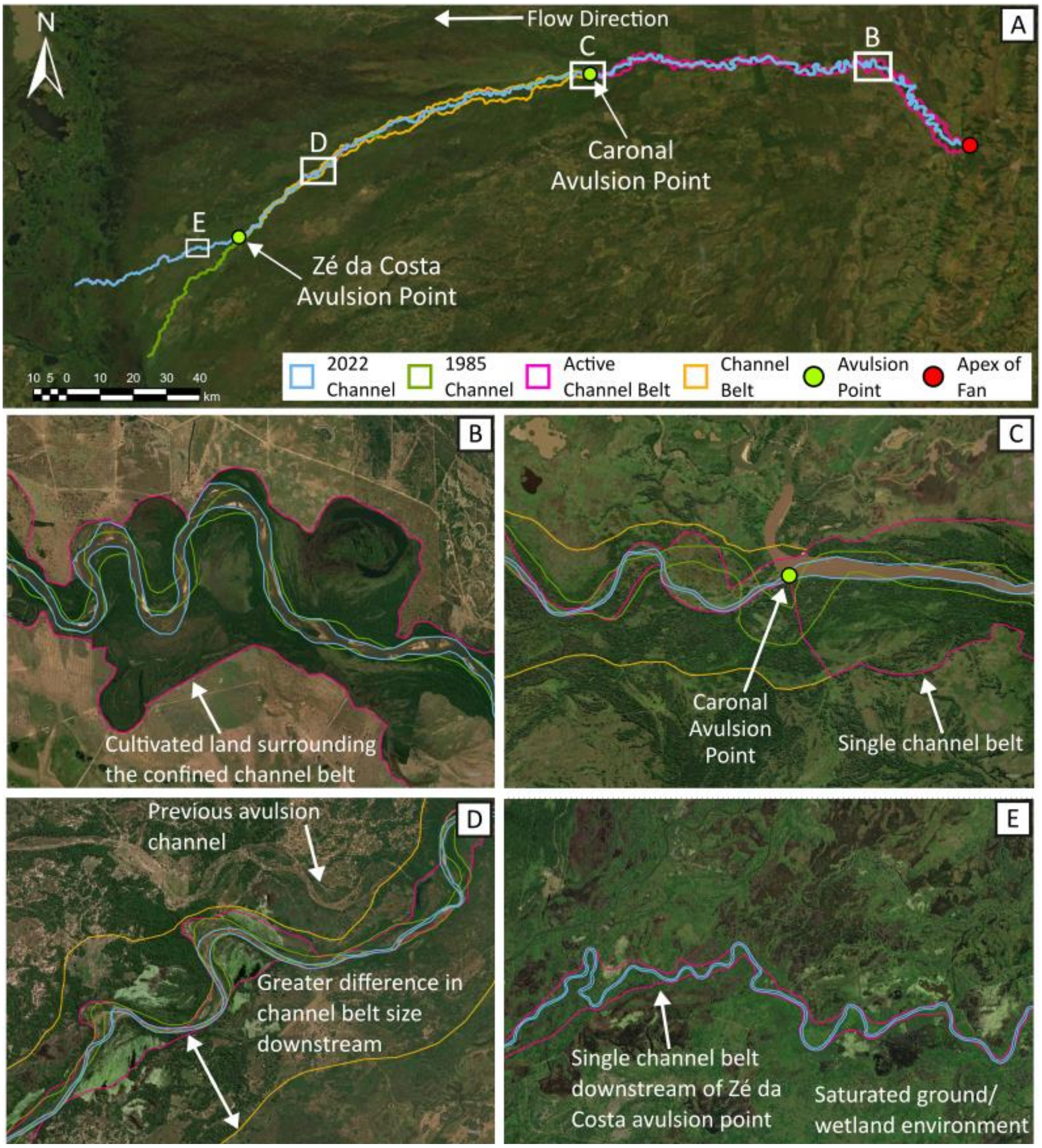

Figure 2.3. A) an overview map of the 2022 Taquari DFS showing the 2022 active channel, the 1985 active channel (not mapped using this imagery), the active channel belt, and the channel belt. Insets are highlighted downstream in white boxes and the avulsion points are highlighted by green marker points. B) a section of the active channel belt upstream of the Caronal avulsion point where the active channel belt is confined and the boundary between the confined channel belt and the unconfined terraces is hidden by agricultural activity. C) the location of the Caronal avulsion point, where two separate channel belts are present downstream of the avulsion point: the active channel belt and the channel belt. D) the difference between the active channel belt and the channel belt downstream and evidence of a previous avulsion channel outside of the channel belt. E) the 2022 channel in the distal DFS where only the active channel belt is present downstream of the Zé da Costa avulsion point. This section of the DFS shows the wetland environment the river exists in with dark areas of saturated land and small bifurcation channels.

separate channel belt which shows the channel's wider migration when it had a higher discharge.

There are many influences on active channel belt and channel belt shape downstream which are outlined below. Firstly, where the two channel belts are the same width upstream of the Caronal avulsion point, the active channel belt is often observed to be very close in width to the 2022 active channel. This is primarily because the active channel is incised into the DFS surface upstream of the Caronal avulsion point (due to a drop in base level (Assine 2005; Buehler et al., 2011)) which results in the creation of a confined active channel belt. The confined active channel belt shows the limited migration capacity of the active channel as it is unable to migrate freely over the DFS surface.

Additionally, in some parts of the active channel belt it was difficult to map the boundary between the confined channel belt and the terraces above this confinement due to farmland which overlaps both areas (Figure 2.3B). It was clear that in some areas of the active channel belt, agricultural activity had cultivated land very close to the active channel. This resulted in straighter sections of the active channel belt boundary being created which showed where vegetation had been removed and evidence of the previous channel belt extent (often indicated by abandoned meander deposits) was lost (Figure 2.3B). In these cases, where it was clear that cultivated land had removed evidence of the active channel belt extent then the boundary of the active channel belt was drawn where there was clear evidence of channel migration (i.e., meander deposits or vegetation cover which indicated the presence of a previously active channel).

Downstream of the Caronal avulsion point, vegetation was also used to differentiate between the active channel belt and the channel belt (which is no longer active). Vegetation was used to differentiate between areas of the DFS that were frequently occupied by the actively migrating channel (active channel belt) and areas of the DFS that had evidence of meander migration but are no longer occupied by the active channel (channel belt). A thick tree line often existed along the banks of the channel separating unvegetated sandy floodplains from thick shrubs and trees. The parts of the channel belt which had not been occupied by the river for longer periods were able to establish thicker vegetation than parts of the channel belt which were more frequently occupied by the migrating channel (and therefore had more sparse vegetation). Although vegetation grows quickly within the active channel belt due to the river existing in a wetland environment, the difference between the thicker vegetation (i.e., densely populated trees) and the more sparsely populated vegetation (with much fewer trees) is still clear.

Meander deposits are also used to differentiate between the active channel belt and channel belt extents. Active meander deposits are formed by the actively migrating channel and are therefore found within the active channel belt (as these deposits are still attached to the active channel). Abandoned meander deposits are not attached to the active channel as they are deposited by a previous version of the channel and are therefore associated with the channel belt. These deposits are identified through ox-bow lakes and scroll bar amalgamation. Abandoned meander deposits are significantly larger than active meander deposits downstream of the Caronal avulsion point and often sit further from the 2022 channel showing that they are clearly deposited by a larger channel and thus help indicate the channel belt extent. Abandoned meander deposits that are attached to abandoned channel bifurcations that rejoin the channel downstream are included in channel belt extent. Previous avulsion channels and bifurcations that flow in a different direction from the main channel are not included in the channel belt extent (Figure 2.3D).

In parts of the distal zone, it was often difficult to map the active channel belt extent due to the Taquari DFS existing in a wetland environment. In distal reaches, the DFS is often saturated with water, resulting in any evidence of meander migration or deposition being hidden by large ponds for example (Figure 2.3E). In addition, the climate favours good growth of vegetation which also hides scroll bars for example. The use of different satellite imagery such as Bing Maps, Google Earth, and Google Earth Timelapse was useful here as imagery from different time periods and flow stages of the channel revealed different features of the channel belt such as scroll bars that were only visible under certain conditions such as drier months of the year.

Using the above interpretations, an active channel belt polygon and a channel belt polygon were created on ArcGIS Pro. Firstly, a polygon was drawn around the active channel belt extent, following this it was then duplicated for the channel belt so the sections of the channel belt upstream of the Caronal avulsion point and downstream Zé da Costa avulsion point would be identical. Secondly, the polygon centreline was extracted, using the same method outlined previously for channel width, before splitting the centreline at the Caronal avulsion point (for the active channel belt only) and smoothing the line to adjust for width changes upstream and downstream of this point (Figure 2.2). Thirdly, points were generated and labelled every 2% downstream along the centreline for consistent data collection. The centreline was then split at these 2% marker points so that transects could be generated at the start and end of each line segment. Finally, the transects were used to split the polygon at the 2% marker points so mean width could be calculated by dividing the area of the polygon between the 2% markers by the length of the split centreline between the markers.

2.4 Meander Deposit Measurements

Active and abandoned meander deposits are measured on 2022 imagery only and not 1985 imagery as the low resolution of the Landsat5 imagery did not allow for measurements of this detail. Active meander deposits are defined in this study as deposits of the 2022 channel that are still attached and associated with processes of the active channel (Figure 2.4). They are identified by looking for evidence of scroll bar accretion and migration on the inside bend of the meander (point-bar deposit). As the river migrates frequently and the limbs of the meandering river often translate, rotate, and expand, it can be difficult to differentiate between the general oscillation of the river and the growth and migration of point-bar deposits as these processes often leave similar marks on the landscape (Figure 2.4C).

Abandoned meander deposits are defined in this study as deposits that are not deposits of the currently active channel (2022 channel), and are instead deposits of a higher discharge pre-avulsion channel (Figure 2.4). Abandoned meander deposits are not attached to the 2022 channel and are often related to ox-bow lakes or identified by scroll bar marks on the landscape. Active and abandoned meander deposits are mainly differentiated by whether the deposit is attached to the channel or not. However, many abandoned meander deposits downstream of the Caronal avulsion sit very close to the 2022 channel; these deposits are then differentiated from the active deposits by their size.

Downstream of the Caronal avulsion point active meander deposits become much smaller than abandoned meander deposits, reflecting the decrease in discharge in the 2022 channel. It therefore becomes easier to differentiate between active and abandoned deposits downstream. Large meander deposits that are deposited

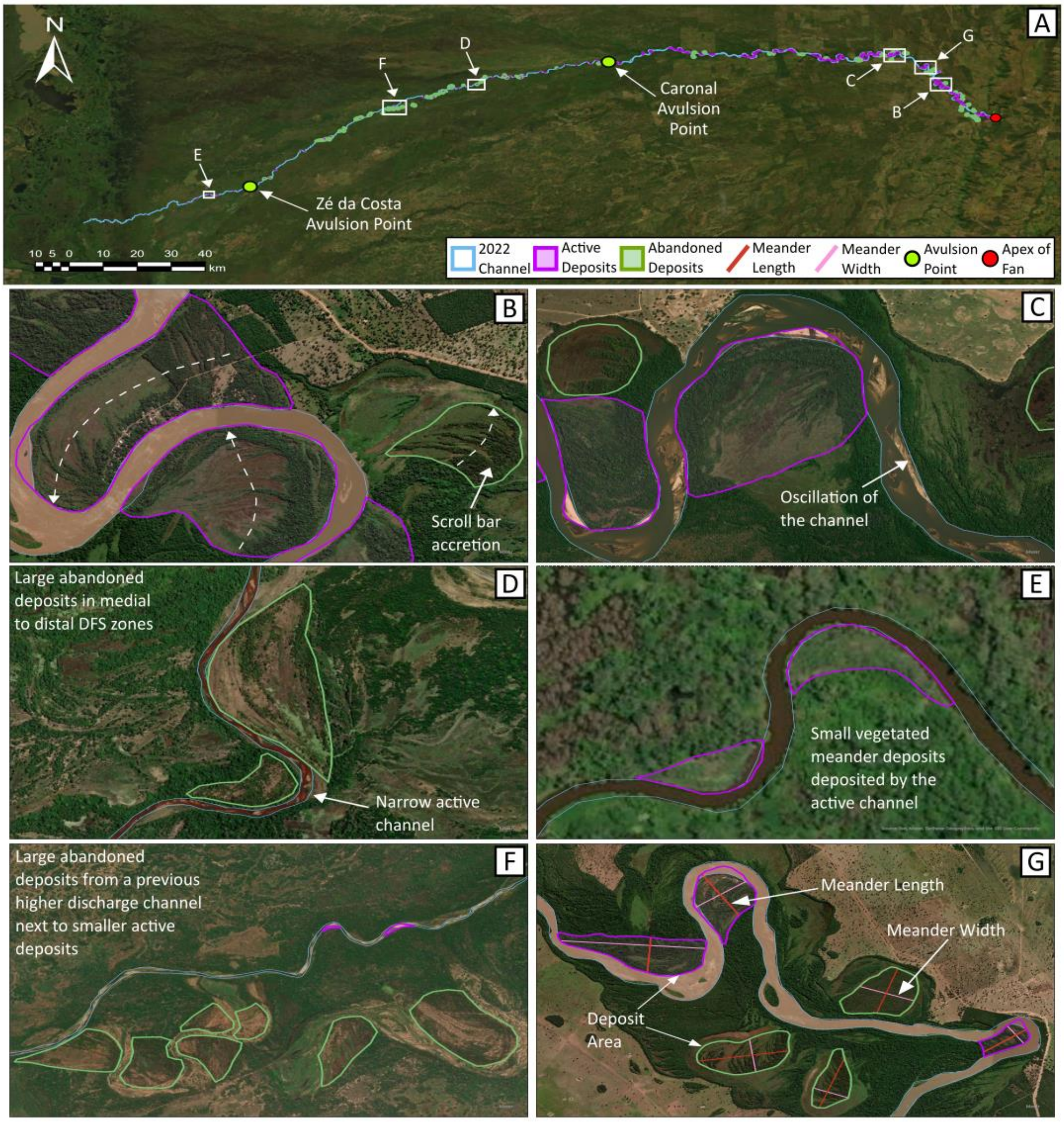

Figure 2.4. A) the location of active and abandoned meander deposits downstream on the 2022 Taquari DFS. B) active and abandoned meander deposits with scroll bars and arrows indicating their direction of growth. The position of the abandoned deposit demonstrates how the channel has migrated over time. C) oscillation of the channel is highlighted to differentiate between meander deposits and lateral movement of the channel's limbs. D) large abandoned meander deposits in the medial to distal DFS zones where the 2022 channel is much narrower. E) small active meander deposits covered in vegetation formed on the inside bend of the meander. F) large abandoned meander deposits in medial to distal DFS zones close to much smaller active meander deposits which are attached to the 2022 channel. G) area, length, and width measurements of meander deposits.

close to the 2022 channel downstream of the Caronal avulsion point are interpreted as abandoned meander deposits as these deposits are substantially larger than deposits associated with the currently active 2022 channel where the width of the channel is significantly reduced downstream of the avulsion point. These abandoned deposits are interpreted to be associated with the pre-avulsion channel which had a higher discharge and sediment supply.

To measure the area of the active and abandoned deposits, polygons were drawn on ArcGIS Pro around the extent of the deposit where scroll bar accretion could be seen (Figure 2.4G). Deposit width was measured perpendicular to point-bar migration direction along the longest axis of the deposit, and deposit length was measured perpendicular to the width along the longest axis of the deposit (Figure 2.4G). The distance of these deposits downstream was calculated using each channel's centreline and creating a 'centrepoint' marker for each deposit by splitting the centreline between these markers using the 'Split Line at Point' tool on ArcGIS. Deposit areas are measured in km^2 reflecting the significantly larger area of the deposits as compared to the deposit length and width which are measured in metres.

2.5 Sinuosity

Sinuosity is a measure of the curvature of the river; the more bends a river has the more sinuous it will be (Wilzbach and Cummins, 2008). Sinuous rivers have a sinuosity value > 1.5 (Wilzbach and Cummins, 2008), however, a cut-off value of 1.3 can be used to differentiate between straight and sinuous channels (Brice, 1964; Makaske, 2001; Assine, 2005). The sinuosity of the 1985 channel and the 2022 channel was calculated using the centreline of each channel polygon (Figure 2.5). Sinuosity is typically measured along the part of the channel interpreted as being the deepest (thalweg) then divided by the straight-line distance between the start point and the end point of the channel. However, the centreline is used instead of the thalweg as this can be automatically generated in ArcGIS Pro. This results in the overall sinuosity being reduced slightly as a consequence of the centreline length being shorter than the thalweg length. A

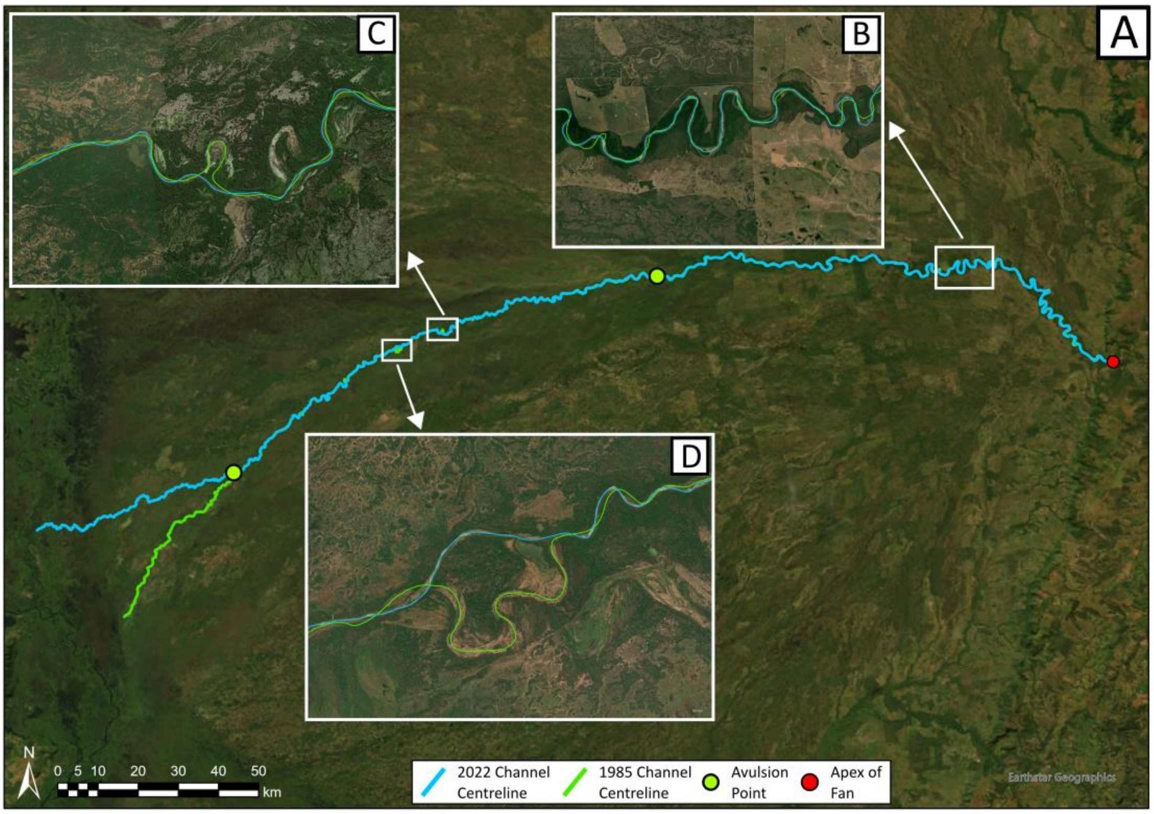

Figure 2.5. A) sinuosity of the 2022 channel and the 1985 channel shown by the centreline of each channel's polygon. B) a section of the proximal DFS where the sinuosity of both channels is similar. Insets C and D show meander cut-offs where the sinuosity of the 2022 channel is lower than the 1985 channel as there is less curvature in this section of the river.

number of meander cut-offs have occurred in the channel between 1985 and 2022 resulting in the reduction in sinuosity in these parts of the channel (Figure 2.5C,D). Meander cut-offs create shorter paths for the channel to flow which are initially straight before the channel begins to meander again.

Sinuosity is measured by dividing the centreline of the channel by the straight-line distance between the start and end of the centreline. Mean sinuosity is measured downstream by splitting the channel centreline at the same 2% marker points that are used to split the channel width and the width of each channel belt. The length of the centreline between each 2% channel marker is divided by the straight line length between the two marker points. Overall sinuosity is measured across the whole channel, then in proximal, medial, and distal DFS zones, and upstream and downstream of the Caronal avulsion point (for the 2022 channel only). For each of these reaches, the length of the centreline is divided by the straight line distance between the start and end of each section.

2.6 Elevation and Slope Gradient

A 4 m resolution digital terrain model (DTM) from the European Space Agency (ESA) was used to create an elevation profile along the centreline of the 2022 channel using the 'Section Tool' in ArcGIS Pro. Data from the attribute table were exported to Excel to create the elevation profile then Inkscape was used to annotate the figure. A 30 m resolution shuttle from radar topography mission (SRTM) digital elevation model (DEM) was also used in the project, however, many of the finer details in the distal fan would not be picked up by this DEM. The ESA DTM contains data collected by the TerraSAR-X and TanDEM-X satellites (European Space Agency, 2024) and was requested for the months of June to September 2022 when the river was in normal flow conditions (i.e., no flooding).

The elevation profile runs from the start of the 2022 channel centreline at the apex of the Taquari DFS to the toe of the DFS before it reaches the axial Paraguay Fluvial System. To calculate the gradient of the slope, the difference in elevation was divided by the distance over which the decrease in elevation occurs (m = rise/run) using the units m/km which were converted to m/m by dividing the gradient by 1000. The gradient was calculated for the whole system, then in proximal, medial, and distal DFS zones, and both upstream and downstream reaches of the Caronal avulsion point.

3 Results

This chapter outlines the results of data collected across the Taquari DFS using satellite imagery from 1985 and 2022 (Figure 3.1). The 1985 imagery (measuring active channel width and sinuosity only), shows the Taquari DFS before the initiation of the Caronal avulsion (1996 to 1997), and represents the pre-avulsion DFS. The 2022 imagery shows the currently active system experiencing the avulsion where channel width, active channel belt width, channel belt width, sinuosity, active meander deposit dimensions, and abandoned meander deposit dimensions are measured (Figure 3.1; Figure 2.4). A digital terrain model (DTM) from 2022 was also used to measure elevation and slope gradient along the 2022 channel centreline; this data was not available for the 1985 system. The previous methods chapter contains more detailed descriptions on each variable measured across 1985 and 2022 imagery.

This chapter will firstly describe the system scale results for the 1985 system (i.e., across the whole system) then the results in proximal, medial, and distal DFS zones in order to address the first objective of this study (Figure 3.1). Then, system scale results for the 2022 system will be described before proximal, medial, and distal DFS zones, and the results for the reaches upstream and downstream of the Caronal avulsion point are described to address the first and third objectives of this study (Figure 3.1). Finally, a comparison between the 1985 and 2022 systems will describe statistical relationships between each system in more detail. Changes in channel width and sinuosity between 1985 and 2022 are also described in order to address the second objective of this study.

R^2 values are used to describe correlation in data. Negative correlations are indicated by a – sign, however, if the R^2 value is < 0.10 then no sign is attached to the value as this is a demonstration of the lack of correlation in the data. Correlation in data is separated into no correlation, very weak, weak, moderate, strong, and very strong correlation based on R^2 values. No correlation < 0.10, very weak correlation = 0.11 to 0.19, weak correlation = 0.20 to 0.39, moderate correlation = 0.40 to 0.59, strong correlation = 0.60 to 0.79, and very strong correlation = 0.80 to 1.00 (BMJ, 2024).

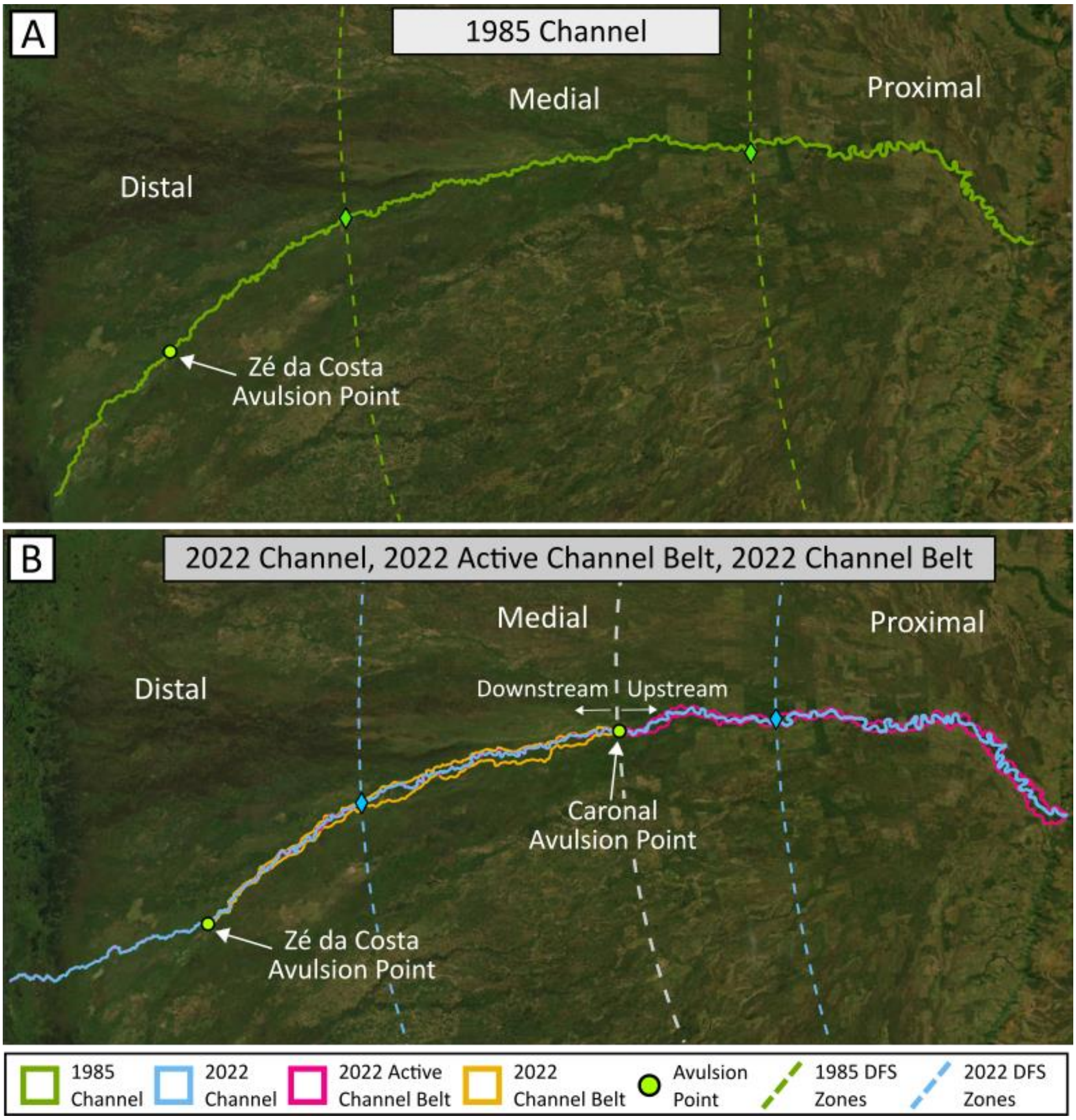

Figure 3.1. A) the 1985 channel (displayed on 2022 imagery for reference) with the Zé da Costa avulsion point marked. (B) the 2022 channel, active channel belt, and channel belt with the Caronal and Zé da Costa avulsion points marked. Each system is split into proximal, medial, and distal DFS zones by dashed lines. The 2022 system shows the location of the Caronal avulsion point which is split into upstream and downstream reaches for comparison.

3.1 1985 Taquari DFS (Pre-avulsion)

3.1.1 Channel Width

Across the whole 1985 system, channel width ranges from 53.59 m to 321.00 m with a median width of 215.64 m, a mean of 202.57 m, and a standard deviation of 83.28 m (Table 3.1). Channel width decreases steadily downstream across the

1985 system as demonstrated by a linear trendline with a strong negative correlation (R^2 = -0.76) (Figure 3.2A).

In the proximal zone of the 1985 system, channel width ranges from 214.97 m to 319.47 m, with a median of 276.46 m, a mean of 273.07 m, and a standard deviation of 34.15 m (Table 3.1). There is no correlation in the proximal zone, as demonstrated by the R^2 value (R^2 < 0.01) (Figure 3.2B). In the medial zone, channel width ranges from 104.39 m to 321.00 m, with a median of 244.49 m, a mean of 219.49 m, and a standard deviation of 72.53 m (Table 3.1). There is a

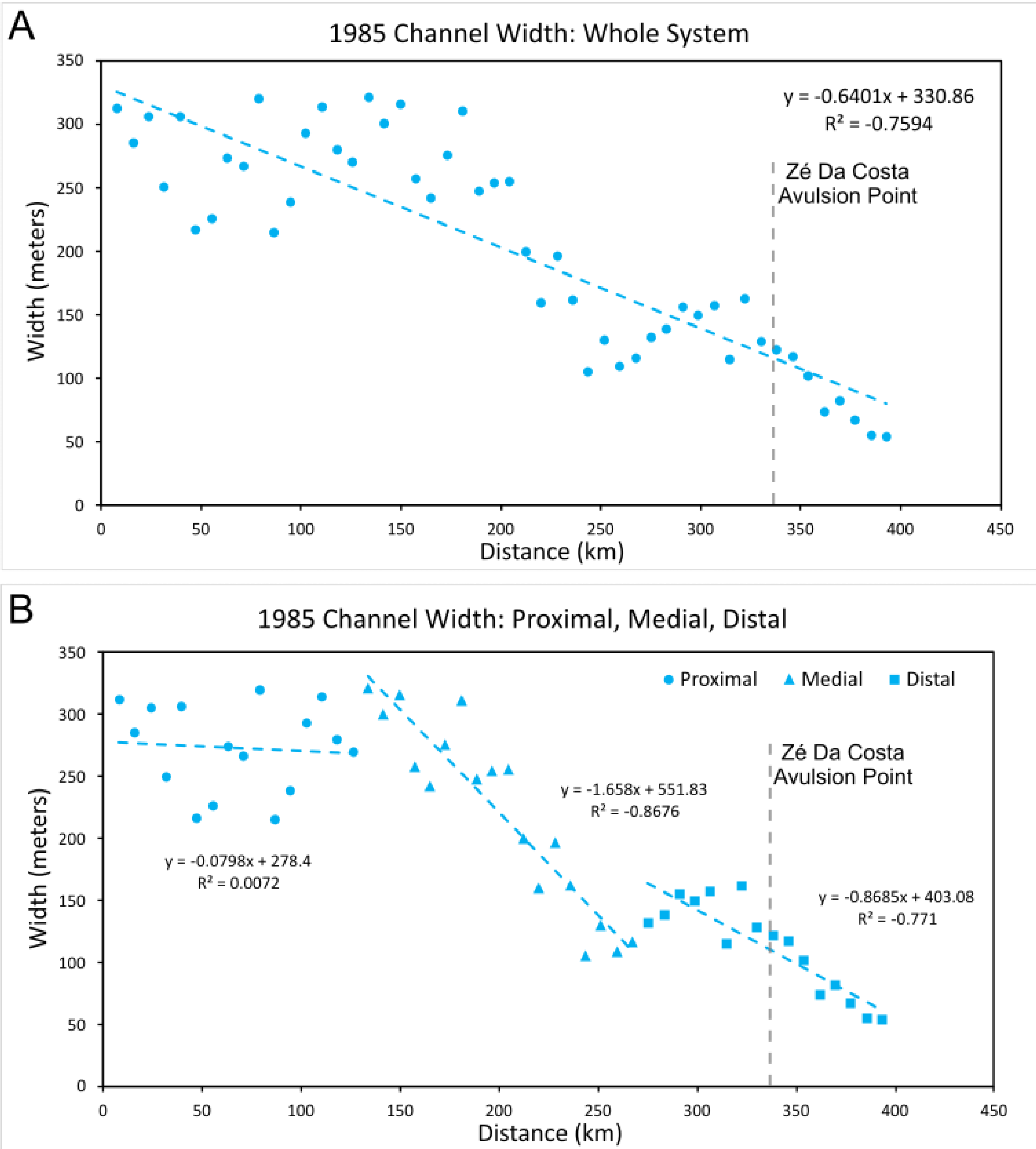

Figure 3.2. 1985 channel width across the whole system (A), and in proximal, medial, and distal DFS zones (B). Each graph displays R^2 values and equations of the line. The Zé Da Costa avulsion point is also marked by a grey dashed line.

large decrease in channel width downstream in the medial zone demonstrated by a linear trendline with a very strong negative correlation (R^2 = -0.87). In the distal zone, channel width ranges from 53.59 m to 161.91 m, with a median of 119.46 m, a mean of 113.03 m, and a standard deviation of 35.82 m (Table 3.1). There is a large decrease in channel width downstream in the distal zone demonstrated by a linear trendline with a strong negative correlation (R^2 = -0.77) (Figure 3.2B).

Table 3.1. 1985 channel width data with statistics and R^2 values across the whole system and in proximal, medial, and distal DFS zones.

	Max	Min	Median	Mean	SD	R^2
1985 Channel Width (m)	321.00	53.59	215.64	202.57	83.28	-0.7594
Proximal Width	319.47	214.97	276.46	273.07	34.15	0.0072
Medial Width	321.00	104.39	244.49	219.49	72.53	-0.8676
Distal Width	161.91	53.59	119.46	113.03	35.82	-0.7710

3.1.2 Sinuosity

1985 channel sinuosity is measured across the whole system and in proximal, medial, and distal DFS zones. To calculate mean sinuosity downstream, the centreline is split between 2% marker points along the channel centreline then the length of the split centreline is divided by the straight line distance between each 2% marker point. Overall sinuosity, and sinuosity of each DFS zone, is calculated by dividing the centreline of the channel reach by the straight line distance between the start and end of the centreline in each reach. Further details on the calculation of sinuosity can be found in methods section 2.5. The overall sinuosity of the 1985 channel is 1.55 with a range in sinuosity values from 1.05 to 2.32. The median sinuosity is 1.32, the mean is 1.36, and the standard deviation is 0.24 (Table 3.2). Sinuosity generally decreases downstream across the pre-avulsion system demonstrated by a linear trendline with a weak negative correlation (R^2 = -0.22) (Figure 3.3A).

In the proximal DFS zone the overall sinuosity is 1.76, with a range in sinuosity values between 1.16 to 2.32. The median sinuosity is 1.56, the mean is 1.54, and the standard deviation is 0.28 (Table 3.2). Sinuosity shows no correlation in the

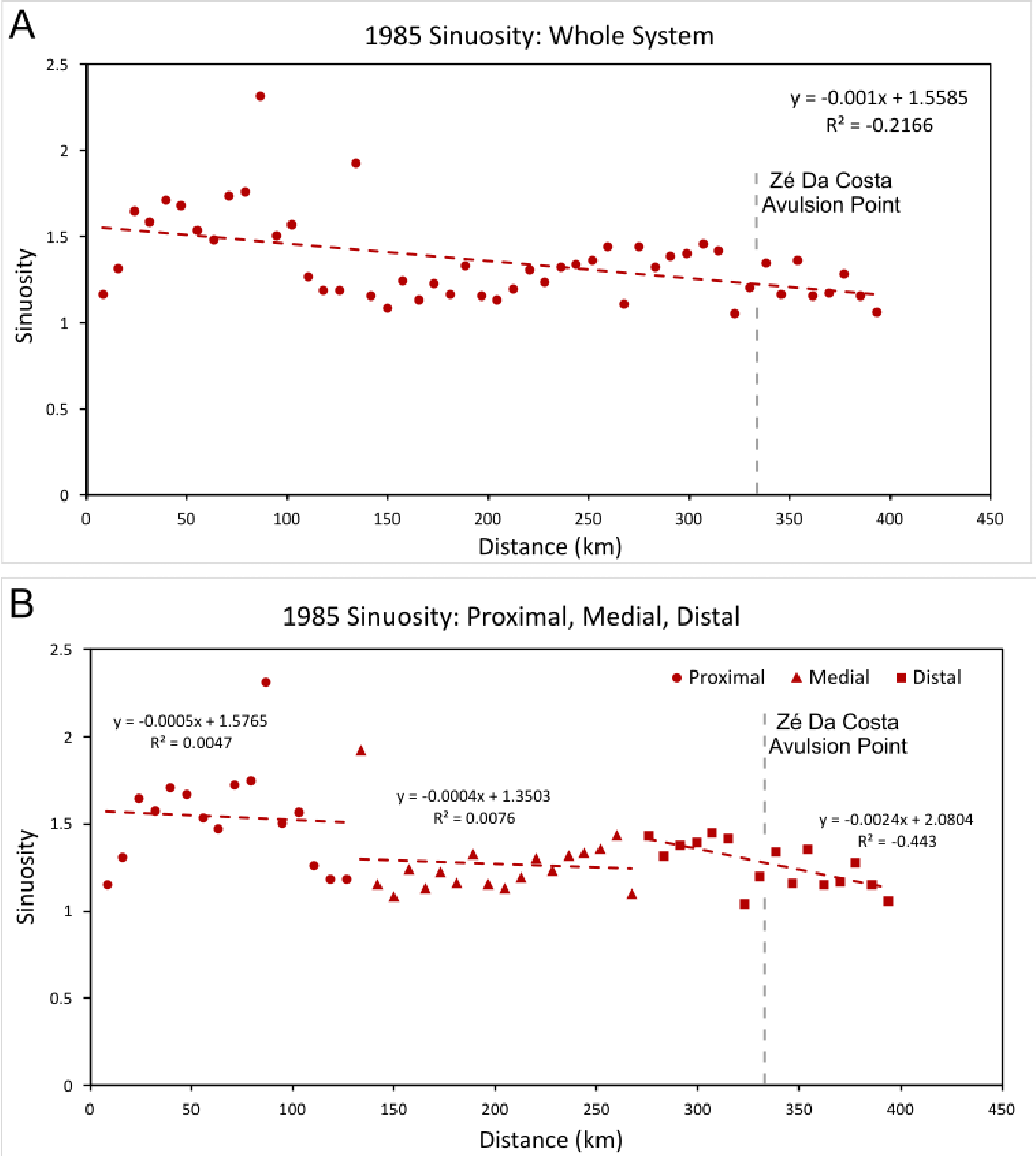

Figure 3.3. 1985 channel sinuosity across the whole system (A), and in proximal, medial, and distal DFS zones (B). Each graph displays R^2 values and equations of the line. The Zé Da Costa avulsion point is also marked by a grey dashed line.

proximal zone, as demonstrated by the R^2 value ($R^2 < 0.01$) (Figure 3.3B). The medial zone of the 1985 channel has an overall sinuosity of 1.27 with a range between 1.08 to 1.93. The median is 1.23, the mean is 1.27, and the standard deviation is 0.19 (Table 3.2). Sinuosity continues to show no correlation in the medial zone and remains fairly constant downstream, as demonstrated by the R^2 value ($R^2 < 0.01$) (Figure 3.3B). The distal zone of the 1985 channel has an overall sinuosity of 1.30 with a range between 1.05 to 1.46. The median is 1.30, the mean is 1.27, and the standard deviation is 0.13 (Table 3.2). The distal zone has the largest decrease in sinuosity of the three DFS zones as a linear trendline with a moderate negative correlation (R^2 = -0.44) demonstrates this change in data (Figure 3.3B).

Table 3.2. 1985 channel sinuosity data with statistics and R^2 values over the whole system and in proximal, medial, and distal DFS zones.

	Overall Sinuosity	Max	Min	Median	Mean	SD	R^2
1985 Channel Sinuosity	1.55	2.32	1.05	1.32	1.36	0.24	-0.2166
Proximal Sinuosity	1.76	2.32	1.16	1.56	1.54	0.28	0.0047
Medial Sinuosity	1.27	1.93	1.08	1.23	1.27	0.19	0.0076
Distal Sinuosity	1.30	1.46	1.05	1.30	1.27	0.13	-0.4430

3.1.3 Summary of the 1985 Taquari DFS (Pre-avulsion)

Within the 1985 system, channel width decreases steadily downstream with a strong negative correlation in data (R^2 = -0.76; Figure 3.2A, Table 3.1). 1985 channel sinuosity has a weak negative correlation in data downstream as there is a very slight decrease in sinuosity downstream (R^2 = -0.22; Figure 3.3A, Table 3.2). Both channel width and sinuosity show no correlation in data in the proximal zone (R^2 < 0.01; Figure 3.2B, Figure 3.3B) however, they do show differences in medial and distal zones. For channel width, there are very strong and strong negative correlations in data downstream in the medial and distal zones as channel width steadily decreases downstream in both DFS zones (R^2 = -0.87 and -0.77 respectively). For sinuosity, the medial zone shows no correlation (R^2 < 0.01), and the distal zone has a moderate negative correlation in data as sinuosity generally decreases downstream (R^2 = -0.44). For both variables, the highest values are found in the proximal zone and the lowest values are found in the distal zone. For example, the maximum 1985 channel width is 321.00 m in the proximal zone and the minimum channel width is 53.57 m in the distal zone (Table 3.1). For 1985 channel sinuosity, the maximum sinuosity is 2.32 in the proximal zone and the minimum sinuosity is 1.05 in the distal zone (Table 3.2). Due to the lack of downstream trends in sinuosity the mean sinuosity for both the medial and distal DFS zones is 1.27.

3.2 2022 Taquari DFS (During Avulsion)

3.2.1 Elevation and Slope Gradient

A digital terrain model (DTM) from 2022 was used to extract elevation and slope gradient data using the 2022 channel centreline. Across the whole 2022 channel, elevation and slope gradient decrease downstream starting at an elevation of 186.54 m to an elevation of 85.16 m with an average gradient of -0.00025 m/m. Median elevation is 130.49 m, mean elevation is 131.74 m, and the standard deviation is 30.29 m (Figure 3.4; Table 3.3).

In the proximal zone of the 2022 channel, elevation decreases downstream with the highest elevation at 186.54 m and the lowest elevation at 149.36 m and a gradient of -0.00027 m/m. The median elevation is 167.06 m, the mean elevation is 167.50 m, the standard deviation is 10.45 m (Table 3.3). In the medial zone, elevation decreases downstream from 148.66 m to 110.80 m with a

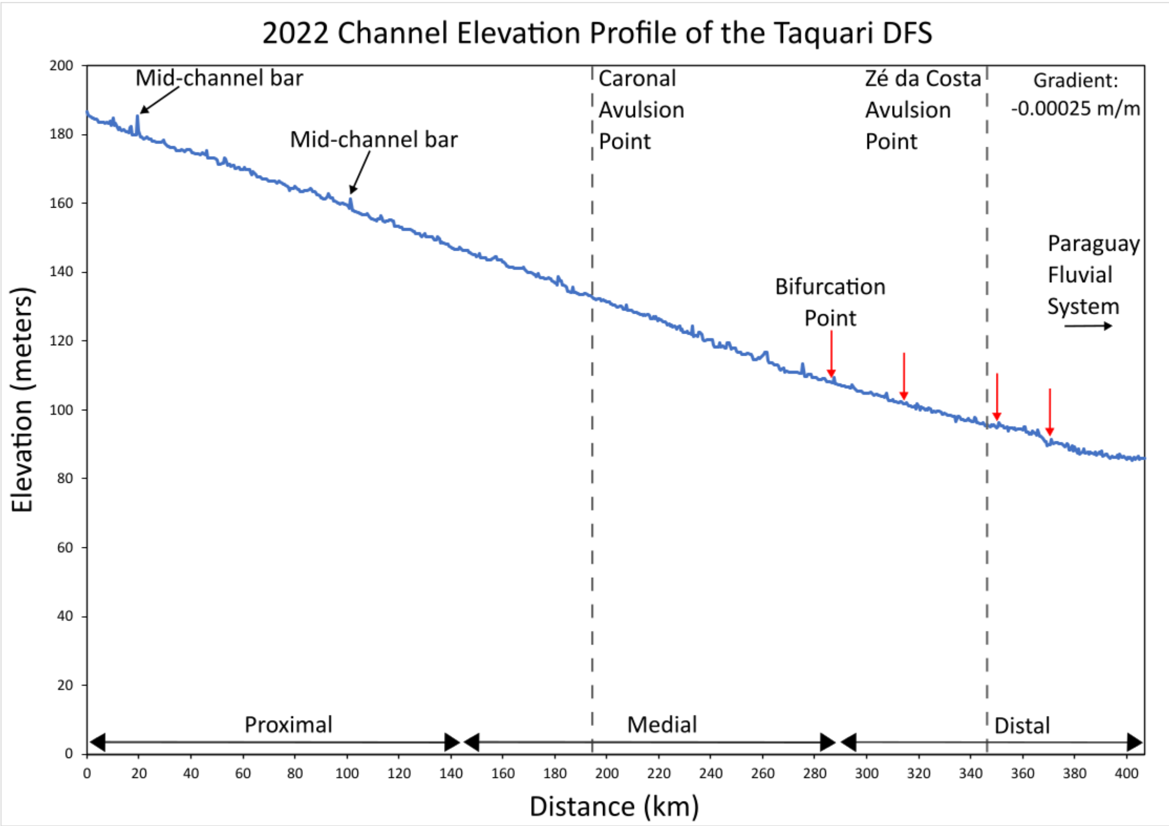

Figure 3.4. 2022 channel elevation profile of the Taquari DFS from the apex (left) to toe (right) of the system. The elevation decreases downstream with an overall gradient of -0.00025 m/m. The Caronal avulsion point and the Zé da Costa avulsion point are marked by grey dashed lines. Arrows at the bottom of the figure indicate proximal, medial, and distal DFS zones. Ridges of higher elevation within the profile have been marked as mid-channel bars, however some of these may be point bars or localised artifacts. Red arrows downstream of the avulsion point indicate where bifurcations occur along the channel. The 2022 channel is incised into the DFS until it reaches the Caronal avulsion point, however, this is not obvious on the profile (Assine 2005; Buehler et al., 2011).

gradient of -0.00025 m/m. The median elevation is 130.37 m, the mean is 130.27 m, the standard deviation is 10.97 m (Table 3.3). In the distal DFS zone, elevation decreases from 113.25 m to 85.16 m, with a gradient of -0.00018 m/m. The median elevation is 96.99 m, the mean is 97.32 m, the standard deviation is 7.73 m (Table 3.3).

Upstream of the Caronal avulsion point elevation decreases from 186.54 m to 133.11 m with a gradient of -0.00028 m/m. The median elevation is 160.08 m, the mean elevation is 159.55 m, the standard deviation is 15.56 m (Table 3.3). Downstream of the Caronal avulsion point elevation decreases from 132.63 m to 85.16 m, with a gradient of -0.00022 m/m. The median elevation is 104.78 m, the mean is 106.35 m, the standard deviation is 13.97 m (Table 3.3).

There is no obvious convex or concave profile across the elevation profile as there is a steady decrease in elevation downstream. However, downstream of the Caronal avulsion point, particularly the distal zone, the profile becomes concave into the lowland areas of the DFS with the most concave section representing the boundary between the Taquari DFS and the axial Paraguay Fluvial System (Figure 3.4). The distal zone is where the lowest gradient is observed (-0.00018 m/m). The steepest gradients are observed upstream of the Caronal avulsion point (-0.00028 m/m) and in the proximal zone (-0.00027 m/m) of the DFS where the 2022 channel leaves the confinement of the catchment area into the unconfined sedimentary basin. However, there is still a confinement of the channel belt in this area, as outlined in the methods chapter. Along the elevation profile, areas of higher elevation are marked as channel bars as these were observed in satellite imagery, however, these can also represent localised artifacts in the DTM (Figure 3.4).

3.2.2 Channel Width

Across the whole 2022 system, channel width ranges from 15.26 m to 309.88 m with a median width of 52.78 m, a mean of 118.58 m, and a standard deviation of 97.61 m (Table 3.4). There is a steady decrease in active channel width downstream as demonstrated by a linear trendline with a strong negative correlation (R^2 = -0.76) (Figure 3.5A).

In the proximal DFS zone, channel width ranges from 180.14 m to 309.88 m with a median width of 227.10 m, a mean of 230.86 m, and a standard deviation of 39.10 m (Table 3.4). There is no correlation in channel width in the proximal zone as demonstrated by the R^2 value ($R^2 < 0.01$) (Figure 3.5B). In the medial zone, channel width ranges from 20.61 m to 239.34 m with a median of 49.99 m, a mean of 89.60 m, and a standard deviation of 74.22 m (Table 3.4). There is a downstream decrease in channel width demonstrated by a linear trendline with a strong negative correlation in data ($R^2 = -0.61$). In the distal zone, channel width ranges from 15.26 m to 65.83 m, with a median of 26.06 m, a mean of 30.08 m, and a standard deviation of 13.36 m (Table 3.4). Channel width continues to decrease downstream as demonstrated by a linear trendline with a strong negative correlation ($R^2 = -0.60$) (Figure 3.5B).

Upstream of the Caronal avulsion point, channel width ranges from 85.86 m to 309.88 m with a median of 217.39 m, a mean of 217.75 m, and a standard deviation of 47.94 m (Table 3.4). There is a modest downstream decrease in channel width as demonstrated by a linear trendline with a very weak negative correlation ($R^2 = -0.14$) (Figure 3.5C). Downstream of the Caronal avulsion point, channel width ranges from 15.26 m to 65.83 m with a median width of 33.64 m, a mean of 34.11 m, and a standard deviation of 13.18 m (Table 3.4). Width continues to decrease downstream as demonstrated by a linear trendline with a weak negative correlation ($R^2 = -0.30$) (Figure 3.5C).

Table 3.3. 2022 channel elevation and slope gradient data across the whole system, in proximal, medial, and distal DFS portions, and upstream and downstream of the Caronal avulsion point.

	Max	Min	Median	Mean	SD	Gradient (m/m)
Elevation Across Whole System	186.54	85.16	130.49	131.74	30.29	-0.00025
Proximal Elevation	186.54	149.36	167.06	167.50	10.45	-0.00027
Medial Elevation	148.66	110.80	130.37	130.27	10.97	-0.00025
Distal Elevation	113.25	85.16	96.99	97.32	7.73	-0.00018
Elevation Upstream of Avulsion Point	186.54	133.11	160.08	159.55	15.56	-0.00028
Elevation Downstream of Avulsion Point	132.63	85.16	104.78	106.35	13.97	-0.00022

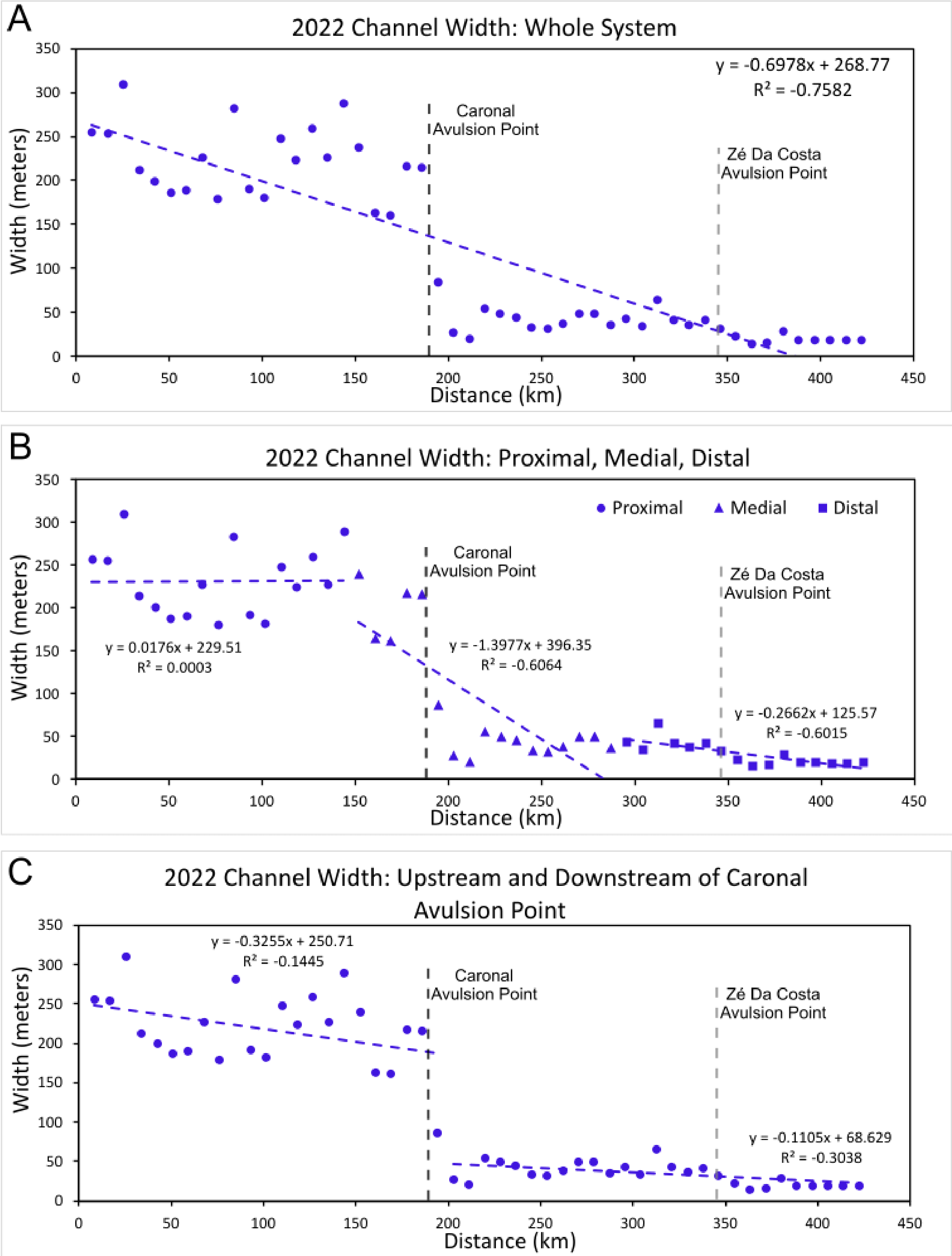

Figure 3.5. 2022 channel width across the whole system (A), in proximal, medial, and distal zones (B), and upstream and downstream of the Caronal avulsion point (C). Each graph displays R^2 values and equations of the line.

Table 3.4. 2022 channel width data with statistics and R^2 values over the whole system, in proximal, medial, and distal DFS zones, and upstream and downstream of the Caronal avulsion point.

	Max	Min	Median	Mean	SD	R^2
2022 Channel Width (m)	309.88	15.26	52.78	118.58	97.61	-0.7582
Proximal Width	309.88	180.14	227.10	230.86	39.10	0.0003
Medial Width	239.34	20.61	49.99	89.60	74.22	-0.6064
Distal Width	65.83	15.26	26.06	30.08	13.36	-0.6015
Width Upstream of Avulsion Point	309.88	85.86	217.39	217.75	47.94	-0.1445
Width Downstream of Avulsion Point	65.83	15.26	33.64	34.11	13.18	-0.3038

3.2.3 Active Channel Belt Width

Across the whole 2022 system, active channel belt width ranges from 47.32 m to 3693.4 m with a median width of 335.37 m, a mean of 1092.67 m, and a standard deviation of 1092.26 m (Table 3.5). Active channel belt width decreases steadily downstream, as demonstrated by a linear trendline with a strong negative correlation (R^2 = -0.77) (Figure 3.6A).

In the proximal DFS zone, active channel belt width ranges from 1321.99 m to 3693.40 m, with a median of 2193.58 m, a mean of 2264.19 m, and a standard deviation of 674.83 m (Table 3.5). Channel belt width decreases downstream in the proximal zone as demonstrated by a linear trendline with a moderate negative correlation (R^2 = -0.59) (Figure 3.6B). In the medial zone, channel belt width channel ranges from 124.49 m to 2129.65 m, with a median of 250.12 m, a mean of 580.56 m, and a standard deviation of 679.90 m (Table 3.5). Active channel belt width decreases downstream in the medial zone as demonstrated by a linear trendline with a moderate negative correlation (R^2 = -0.50) (Figure 3.6B). In the distal zone, channel belt width ranges from 47.32 m to 436.31 m, with a median of 121.60 m, a mean of 155.02 m, and a standard deviation of 97.52 m (Table 3.5). Channel belt width continues to decrease downstream as

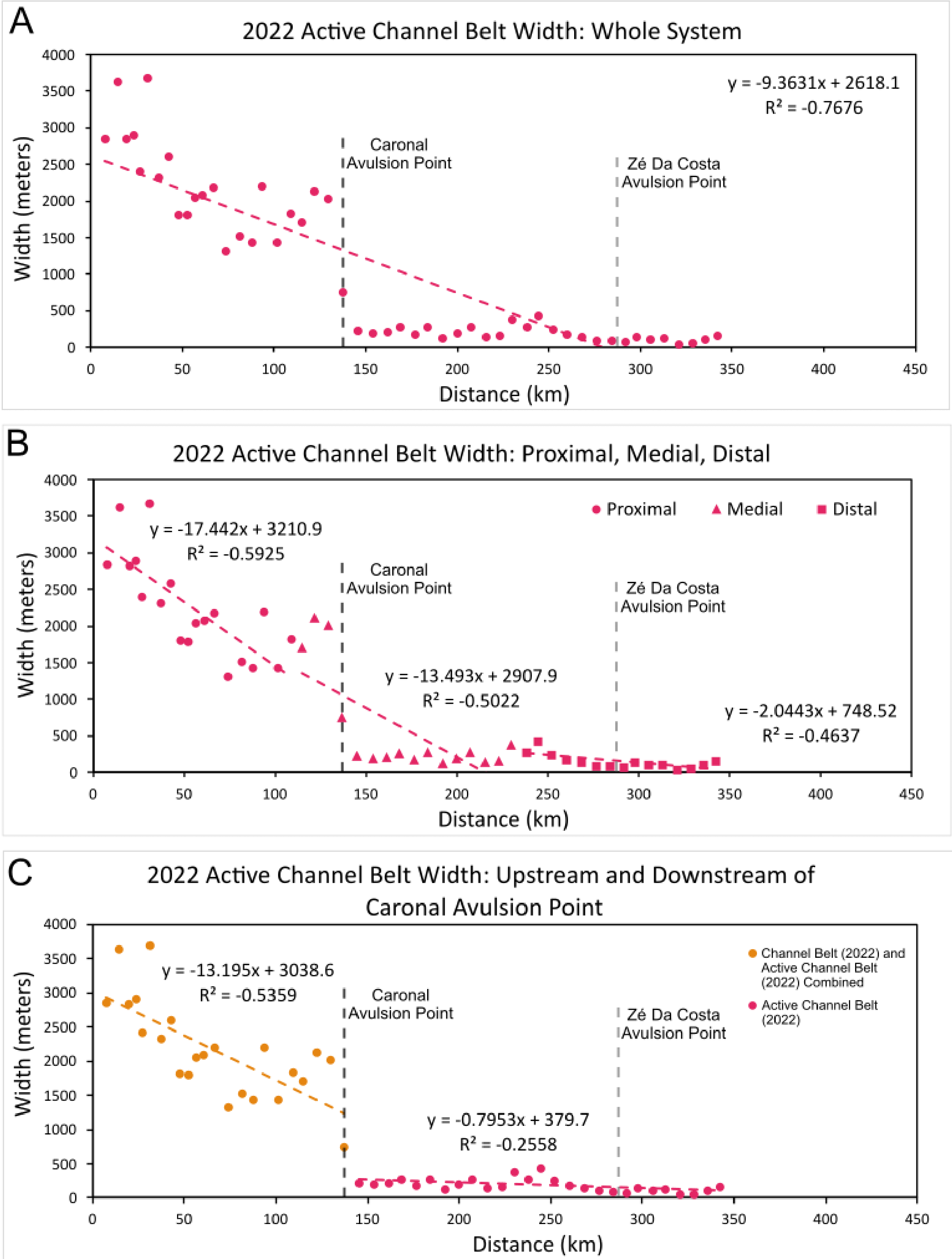

Figure 3.6. 2022 active channel belt width across the whole system (A), in proximal, medial, and distal zones (B), and upstream and downstream of the Caronal avulsion point (C). Each graph displays R^2 values and equations of the line. Graph C shows the combined 2022 active channel belt and 2022 channel belt upstream of the Caronal avulsion point.

demonstrated by a linear trendline with a moderate negative correlation (R^2 = -0.46) (Figure 3.6B).

Upstream of the Caronal avulsion point, active channel belt width ranges from 754.44 m to 3693.40 m with a median width of 2089.20 m, a mean of 2158.27 m, and a standard deviation 693.33 m (Table 3.5). Active channel belt width decreases downstream as demonstrated by a linear trendline with a moderate negative correlation (R^2 = -0.54) (Figure 3.6C). Downstream of the Caronal avulsion point, active channel belt width ranges from 47.32 m to 436.31 m with a median of 162.79 m, a mean of 184.95 m, and a standard deviation of 92.81 m (Table 3.5). Width continues to decrease downstream in the distal zone, as demonstrated by a linear trendline with a weak negative correlation (R^2 = -0.26) (Figure 3.6C).

Table 3.5. 2022 Active channel belt width data with statistics and R^2 values over the whole system, in proximal, medial, and distal DFS zones, and upstream and downstream of the Caronal avulsion point.

	Max	Min	Median	Mean	SD	R^2
2022 Active Channel Belt Width (m)	3693.40	47.32	335.37	1092.67	1092.26	-0.7676
Proximal Width	3693.40	1321.99	2193.58	2264.19	674.83	-0.5925
Medial Width	2129.65	124.49	250.12	580.56	679.90	-0.5022
Distal Width	436.31	47.32	121.60	155.02	97.52	-0.4637
Width Upstream of Avulsion Point	3693.40	754.44	2089.20	2158.27	693.33	-0.5359
Width Downstream of Avulsion Point	436.31	47.32	162.79	184.95	92.81	-0.2558

3.2.4 Channel Belt Width

Channel belt width is differentiated from active channel belt width as the channel belt is not impacted by the Caronal avulsion and therefore has a much larger width than the active channel belt. Upstream of the Caronal avulsion point and downstream of the Zé da Costa avulsion point, the channel belt is the same width as the active channel belt as these channel belts are only differentiated between both avulsion points, as outlined in methods section 2.3. Across the whole 2022 system, channel belt width ranges from 47.32 m to 3693.40 m with a median of 1825.60 m, a mean of 1774.03 m, and a standard deviation of 1046.37 m (Table 3.6). Channel belt width generally decreases downstream, as demonstrated by a linear trendline with a moderate negative correlation (R^2 = -0.48) (Figure 3.7A).

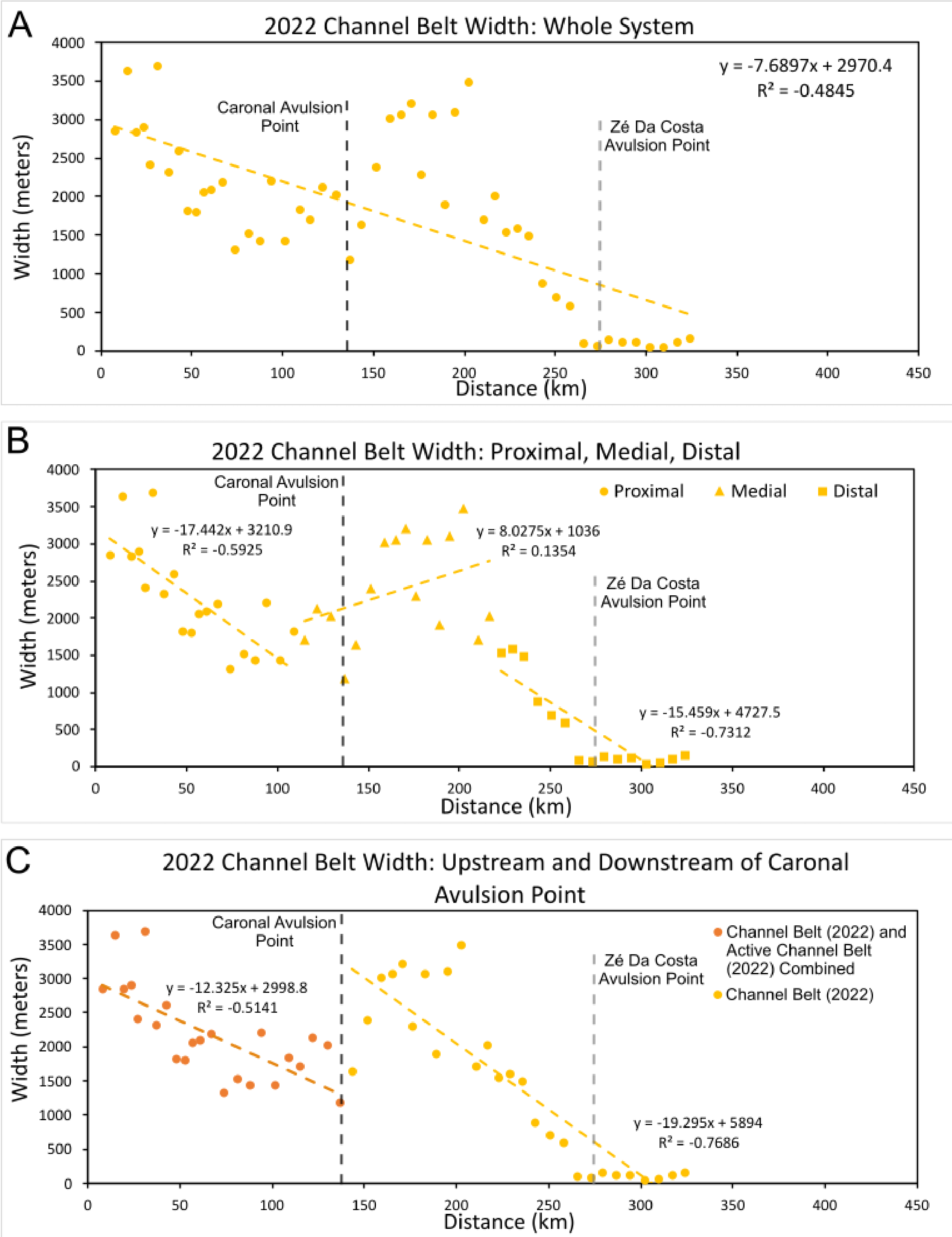

Figure 3.7. 2022 channel belt width across the whole system (A), in proximal, medial, and distal DFS zones (B), and upstream and downstream of the Caronal avulsion point (C). Each graph displays R^2 values and equations of the line. The Zé Da Costa avulsion point is also marked by a grey dashed line.

In the proximal DFS zone, the channel belt has the same width as the active channel belt and therefore both channel belts have the same dimensions in this DFS zone. Channel belt width in the proximal zone ranges from 1321.99 m to 3693.40 m, with a median of 2193.58 m, a mean of 2264.19 m, and a standard deviation of 674.83 m (Table 3.6). There is a general decrease in channel belt width downstream, as demonstrated by a linear trendline with a moderate negative correlation (R^2 = -0.59) (Figure 3.7B). In the medial zone, channel belt width ranges from 1180.75 m to 3483.52 m, with a median of 2211.44 m, a mean of 2371.32 m, and a standard deviation of 670.46 m (Table 3.6). Channel belt width increases slightly downstream demonstrated by a linear trendline with a very weak positive correlation (R^2 = 0.14) (Figure 3.7B). In the distal zone, channel belt width ranges from 47.32 m to 1594.89 m, with a median of 146.65 m, a mean of 516.06 m, and a standard deviation of 570.92 m (Table 3.6). Channel belt width decreases steadily downstream, as demonstrated by a linear trendline with a strong negative correlation (R^2 = -0.73) (Figure 3.7B).

Upstream of the Caronal avulsion point the channel belt is the same width as the active channel belt, as previously outlined. However, there are very slight differences in channel belt width dimensions related to how each polygon was split at the Caronal avulsion point as the active channel belt reduces in size. The width of the channel belt upstream of the avulsion point ranges from 1180.75 m to 3693.40 m, with a median of 2089.20 m, a mean of 2176.80 m, and a standard deviation of 660.47 m (Table 3.6). There is a general decrease in channel width downstream demonstrated by a linear trendline with a moderate negative correlation (R^2 = -0.51) (Figure 3.7C). Downstream of the avulsion point, channel belt width ranges from 47.32 m to 3483.52 m with a median width of 1542.34 m, a mean of 1430.93 m, and a standard deviation of 1183.24 m (Table 3.6). Width continues to decrease downstream demonstrated by a linear trendline with a strong negative correlation (R^2 = -0.77) (Figure 3.7C).

Table 3.6. 2022 channel belt width data with statistics and R^2 values over the whole system, in proximal, medial, and distal DFS zones, and upstream and downstream of the Caronal avulsion point.

	Max	Min	Median	Mean	SD	R^2
2022 Channel Belt Width (m)	3693.40	47.32	1825.60	1774.03	1046.37	-0.4845
Proximal Width	3693.40	1321.99	2193.58	2264.19	674.83	-0.5925
Medial Width	3483.52	1180.75	2211.44	2371.32	670.46	0.1354
Distal Width	1594.89	47.32	146.65	516.06	570.92	-0.7312
Width Upstream of Avulsion Point	3693.40	1180.75	2089.20	2176.80	666.47	-0.5141
Width Downstream of Avulsion Point	3483.52	47.32	1542.34	1430.93	1183.24	-0.7686

3.2.5 Sinuosity

2022 channel sinuosity is measured across the whole system, then in proximal, medial, and distal DFS zones, and upstream and downstream of the Caronal avulsion point. The overall sinuosity of the 2022 channel is 1.56 with a range in sinuosity values between 1.11 to 2.20. The median sinuosity is 1.40, the mean is 1.44, and the standard deviation is 0.26 (Table 3.7). Sinuosity in the active system decreases slightly downstream as demonstrated by a linear trendline with a very weak negative correlation (R^2 = -0.12) (Figure 3.8A).

The proximal DFS zone has an overall sinuosity of 1.82, with a range in sinuosity values between 1.17 to 2.20. The median sinuosity is 1.63, the mean is 1.64, and the standard deviation is 0.30 (Table 3.7). In the proximal zone, sinuosity shows no correlation as demonstrated by the R^2 value (R^2 < 0.01) (Figure 3.8B). In the medial zone, the overall sinuosity is 1.31 with a range between 1.11 to 1.58. The median is 1.26, the mean is 1.29, and the standard deviation is 0.16 (Table 3.7). Sinuosity continues to show no correlation in the medial zone as demonstrated by the R^2 value (R^2 = 0.03) (Figure 3.8B). In the distal zone, the overall sinuosity of the active channel is 1.49 with a range between 1.16 to 1.68. The median is 1.39, the mean is 1.39, and the standard deviation is 0.14 (Table 3.7). Sinuosity increases slightly downstream, as demonstrated by a linear trendline with a very weak positive correlation (R^2 = 0.13) (Figure 3.8B).

Upstream of the Caronal avulsion point, the overall sinuosity is 1.68 with a range between 1.12 to 2.20. The median is 1.51, the mean is 1.54, and the standard deviation is 0.32 (Table 3.7). Sinuosity decreases downstream, as demonstrated by a linear trendline with a very weak negative correlation (R^2 = -0.19) (Figure 3.8C). Downstream of the Caronal avulsion point, the overall sinuosity is 1.39 with a range between 1.11 to 1.68. The median is 1.38, the mean is 1.37, and the standard deviation is 0.15 (Table 3.7). There is no correlation in sinuosity downstream of the avulsion point as demonstrated by the R^2 value (R^2 = 0.08) (Figure 3.8C).

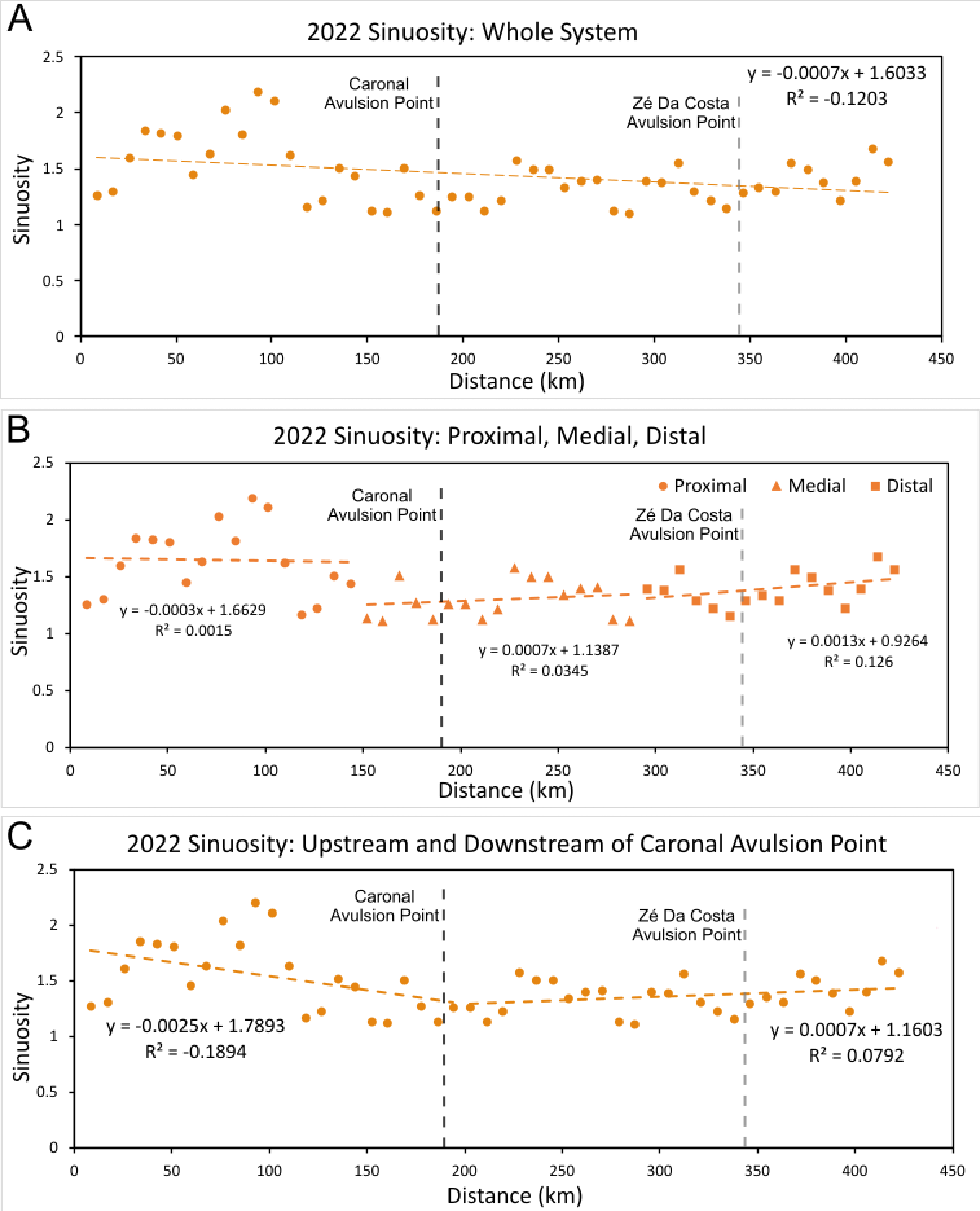

Figure 3.8. 2022 sinuosity across the whole system (A), in proximal, medial, and distal zones (B), and upstream and downstream of the Caronal avulsion point (C). Each graph displays R^2 values and equations of the line.

Table 3.7. 2022 sinuosity data with statistics and R^2 values over the whole system, in proximal, medial, and distal DFS zones, and upstream and downstream of the Caronal avulsion point.

	Overall Sinuosity	Max	Min	Median	Mean	SD	R^2
2022 Channel Sinuosity	1.56	2.20	1.11	1.40	1.44	0.26	-0.1203
Proximal Sinuosity	1.82	2.20	1.17	1.63	1.64	0.30	0.0015
Medial Sinuosity	1.31	1.58	1.11	1.26	1.29	0.16	0.0345
Distal Sinuosity	1.49	1.68	1.16	1.39	1.39	0.14	0.1260
Sinuosity Upstream of Avulsion Point	1.68	2.20	1.12	1.51	1.54	0.32	-0.1894
Sinuosity Downstream of Avulsion Point	1.39	1.68	1.11	1.38	1.37	0.15	0.0792

3.2.6 Active Meander Deposit Dimensions

3.2.6.1 Meander Deposit Area

Across the whole 2022 system, active meander deposit areas range in size from 0.00084 km^2 to 2.29 km^2 with a median area of 0.029 km^2, a mean of 0.37 km^2, and a standard deviation of 0.50 km^2 (Table 3.8). Active meander deposit area generally decreases downstream as demonstrated by a linear trendline with a moderate negative correlation (R^2 = -0.50) (Figure 3.9A).

In the proximal DFS zone, active meander deposit areas range in size from 0.22 km^2 to 2.29 km^2, with a median of 0.98 km^2, a mean of 0.92 km^2, and a standard deviation of 0.46 km^2 (Table 3.8). There is no correlation in meander deposit size downstream in the proximal zone as demonstrated by theR^2 value (R^2 = 0.07) (Figure 3.9B). In the medial zone, meander deposit areas range in size from 0.0022 km^2 to 1.17 km^2, with a median of 0.027 km^2, a mean of 0.16 km^2, and a standard deviation of 0.27 km^2 (Table 3.8). Meander deposit area generally decreases downstream in the medial zone as demonstrated by a linear trendline with a moderate negative correlation (R^2 = -0.46) (Figure 3.9B). In the distal zone, meander deposit areas range in size from 0.00084 km^2 to 0.017 km^2, with a median of 0.0034 km^2, a mean of 0.0063 km^2, and a standard deviation of 0.0051 km^2 (Table 3.8). Meander deposit area generally decreases downstream in the distal zone demonstrated by a linear trendline with a moderate negative correlation (R^2 = -0.50) (Figure 3.9B).

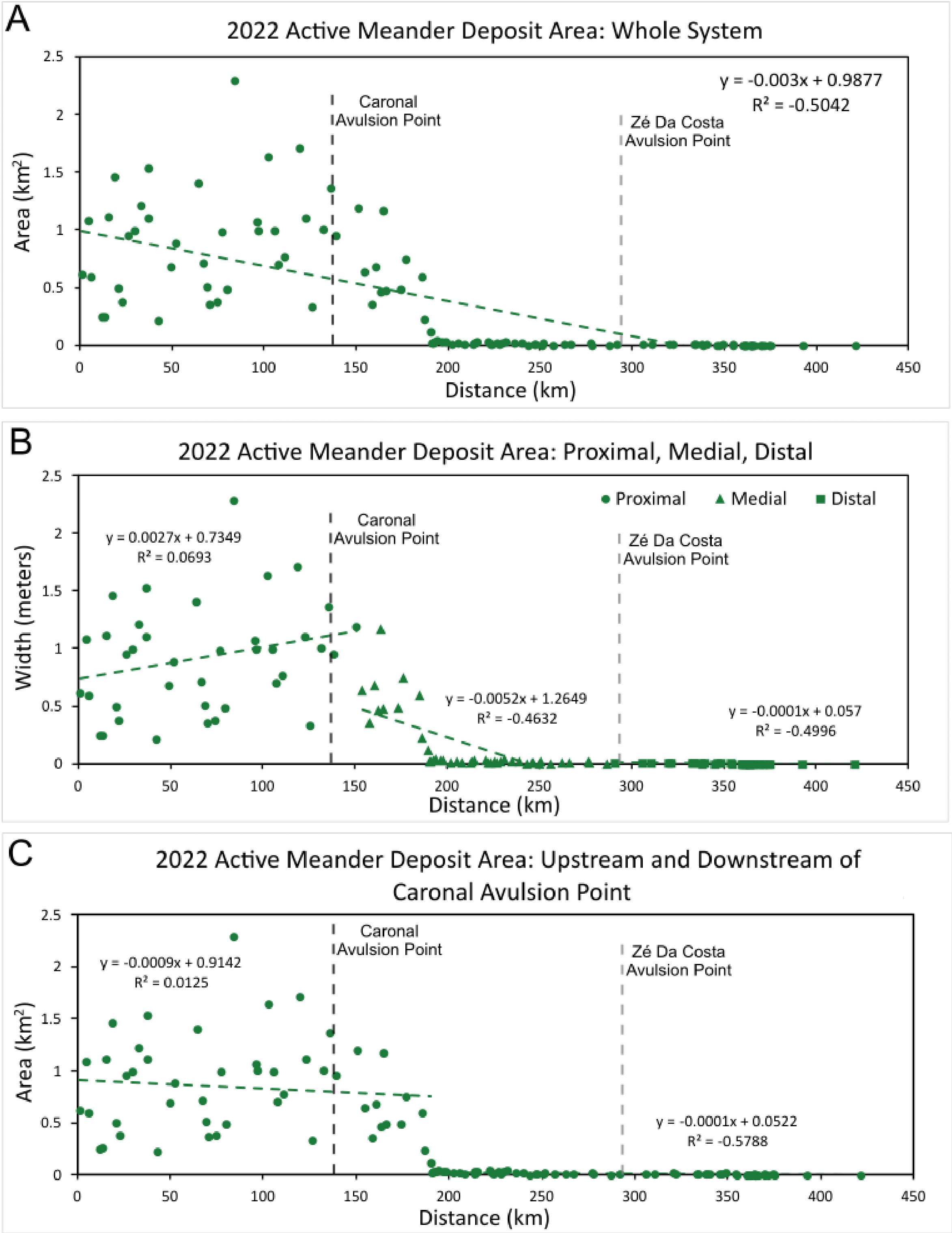

Figure 3.9. Active meander deposit area across the whole system (A), in proximal, medial, and distal zones (B), and upstream and downstream of the Caronal avulsion point (C). Each graph displays R^2 values and equations of the line.

Upstream of the Caronal avulsion point, meander deposit areas range in size from 0.12 km^2 to 2.29 km^2, with a median of 0.75 km^2, a mean of 0.84 km^2, and a standard deviation of 0.45 km^2 (Table 3.8). There is no correlation in meander deposit size upstream of the avulsion point as demonstrated by the R^2 value (R^2 = 0.10) (Figure 3.9C). Downstream of the Caronal avulsion point, meander deposit areas range in size from 0.00084 km^2 to 0.049 km^2, with a median of 0.011 km^2, a mean of 0.014 km^2, and a standard deviation of 0.012 km^2 (Table 3.8). Meander deposit areas generally decrease in size downstream as demonstrated by a linear trendline with a moderate negative correlation (R^2 = -0.58) (Figure 3.9C).

3.2.6.2 Meander Deposit Length

Across the whole 2022 system, active meander deposit lengths range from 12.37 m to 1917.22 m, with a median of 77.26 m, a mean of 377.01 m, and a standard deviation of 457.18 m (Table 3.8). There is a general downstream decrease in deposit length across the whole system, as demonstrated by a linear trendline with a moderate negative correlation (R^2 = -0.56) (Figure 3.10A).

In the proximal DFS zone, active meander deposit lengths range from 332.75 m to 1917.22 m, with a median of 812.12 m, a mean of 865.25 m, and a standard deviation of 405.55 m (Table 3.8). There is no correlation in the proximal zone as demonstrated by the R^2 value ($R^2 < 0.01$) (Figure 3.10B). In the medial zone, meander deposit lengths range from 25.91 m to 1196.94 m, with a median of 71.77 m, a mean of 207.92 m, and a standard deviation of 282.20 m (Table 3.8). Meander deposit lengths generally decrease in the medial zone as demonstrated by a linear trendline with a moderate negative correlation (R^2 = -0.44) (Figure 3.10B). In the distal zone, active meander deposit lengths range from 12.37 m to 75.64 m, with a median of 34.31 m, a mean of 35.15m, and a standard deviation of 16.63 m (Table 3.8). Deposit lengths continue to decrease downstream in the distal zone as demonstrated by a linear trendline with a moderate negative correlation (R^2 = -0.37) (Figure 3.10B).

Upstream of the Caronal avulsion point, meander deposit lengths range from 266.31 m to 1917.22 m, with a median of 693.93 m, a mean of 810.52 m, and a standard deviation of 394.58 m (Table 3.8). There is no correlation in this portion of the river, as demonstrated by the R^2 value (R^2 = 0.04) (Figure 3.10C). Downstream of the Caronal avulsion point, lengths range from 12.37 m to 151.07 m, with a median of 44.24 m, a mean of 50.22 m, and a standard deviation of 27.41 m (Table 3.8). Deposit lengths generally decrease downstream of the avulsion point as demonstrated by a linear trendline with a moderate negative correlation (R^2 = -0.47) (Figure 3.10C).

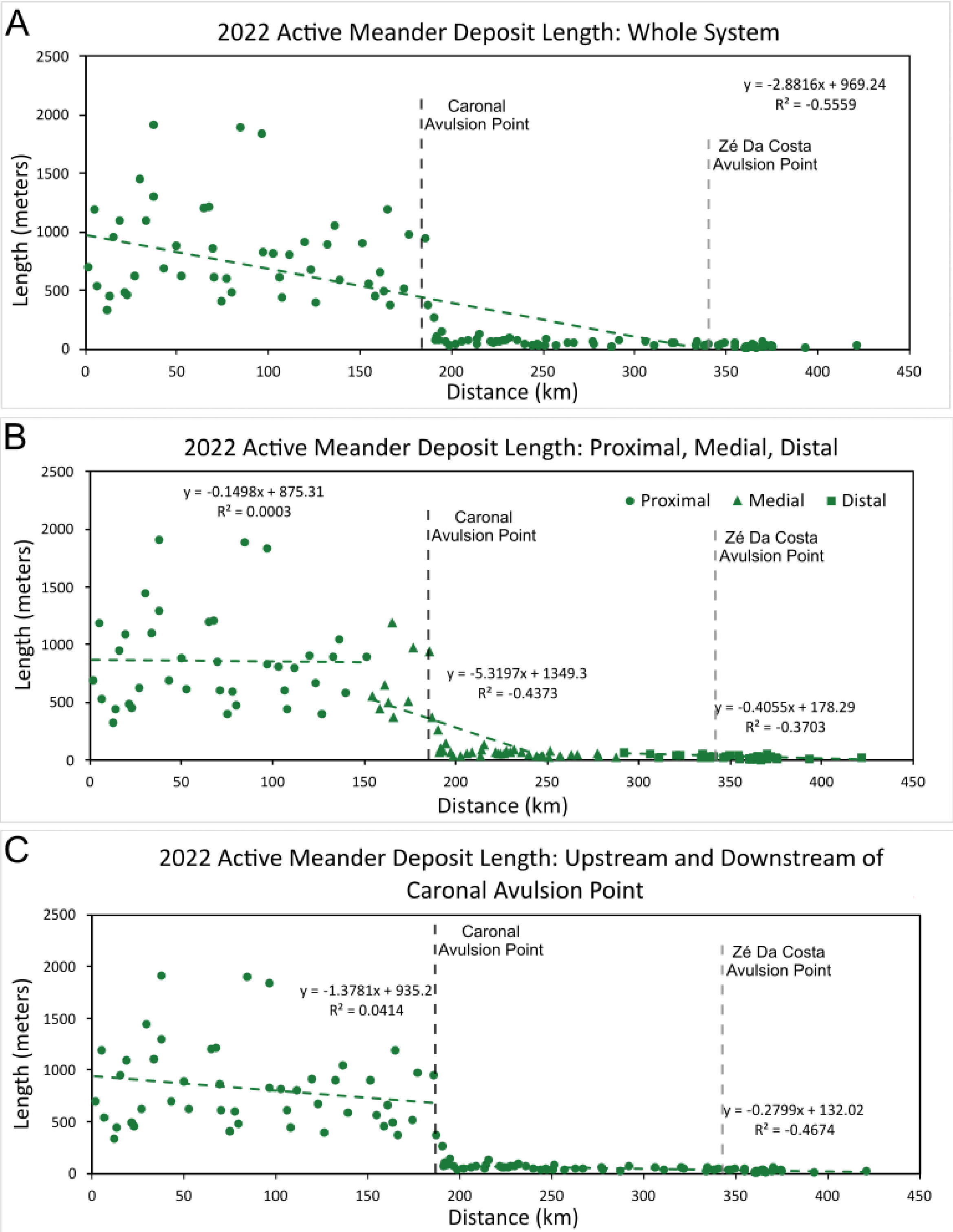

Figure 3.10. Active meander deposit length across the whole system (A), in proximal, medial, and distal zones (B), and upstream and downstream of the Caronal avulsion point (C). Each graph displays R^2 values and equations of the line.

3.2.6.3 Meander Deposit Width

Across the whole 2022 system active meander deposit widths range from 43.32 m to 2522.15 m, with a median of 383.67 m, a mean of 692.54 m, and a standard deviation of 631.06 m (Table 3.8). Deposit width generally decreases downstream across the active system as demonstrated by a linear trendline with a moderate negative correlation (R^2 = -0.58) (Figure 3.11A).

In the proximal DFS zone, active meander deposit widths range from 384.03 m to 2522.15 m, with a median of 1269.68 m, a mean of 1343.08 m, and a standard deviation of 528.74 m (Table 3.8). There is no correlation in width data in the proximal zone as demonstrated by the R^2 value (R^2 = 0.07) (Figure 3.11A). In the medial zone, widths range from 75.56 m to 1761.36 m, with a median of 364.19 m, a mean of 536.1 m, and a standard deviation of 420.68 m (Table 3.8). Meander deposit widths steadily decrease downstream in the medial zone as demonstrated by a linear trendline with a strong negative correlation (R^2 = -0.64) (Figure 3.11A). In the distal zone, widths range from 43.32 m to 319.01 m, with a median of 102.96 m, a mean of 147.29 m, and a standard deviation of 81.73 m (Table 3.8). Meander deposit widths generally decrease downstream in the distal zone as demonstrated by a linear trendline with a moderate negative correlation (R^2 = -0.48) (Figure 3.11A).

Upstream of the Caronal avulsion point, meander deposit widths range from 384.03 m to 2522.15 m, with a median of 1267.12 m, a mean of 1301.75 m, and a standard deviation of 501.43 m (Table 3.8). There is high no correlation in meander deposit widths upstream of the avulsion point as demonstrated by the R^2 value (R^2 < 0.01) (Figure 3.11C). Downstream of the Caronal avulsion point, meander deposit widths range from 43.32 m to 712.69 m, with a median of 233.43 m, a mean of 233.3 m, and a standard deviation of 134.95 m (Table 3.8). There is a steady decrease in meander deposit widths downstream of the avulsion point as demonstrated by a linear trendline with a strong negative correlation (R^2 = -0.61) (Figure 3.11C).

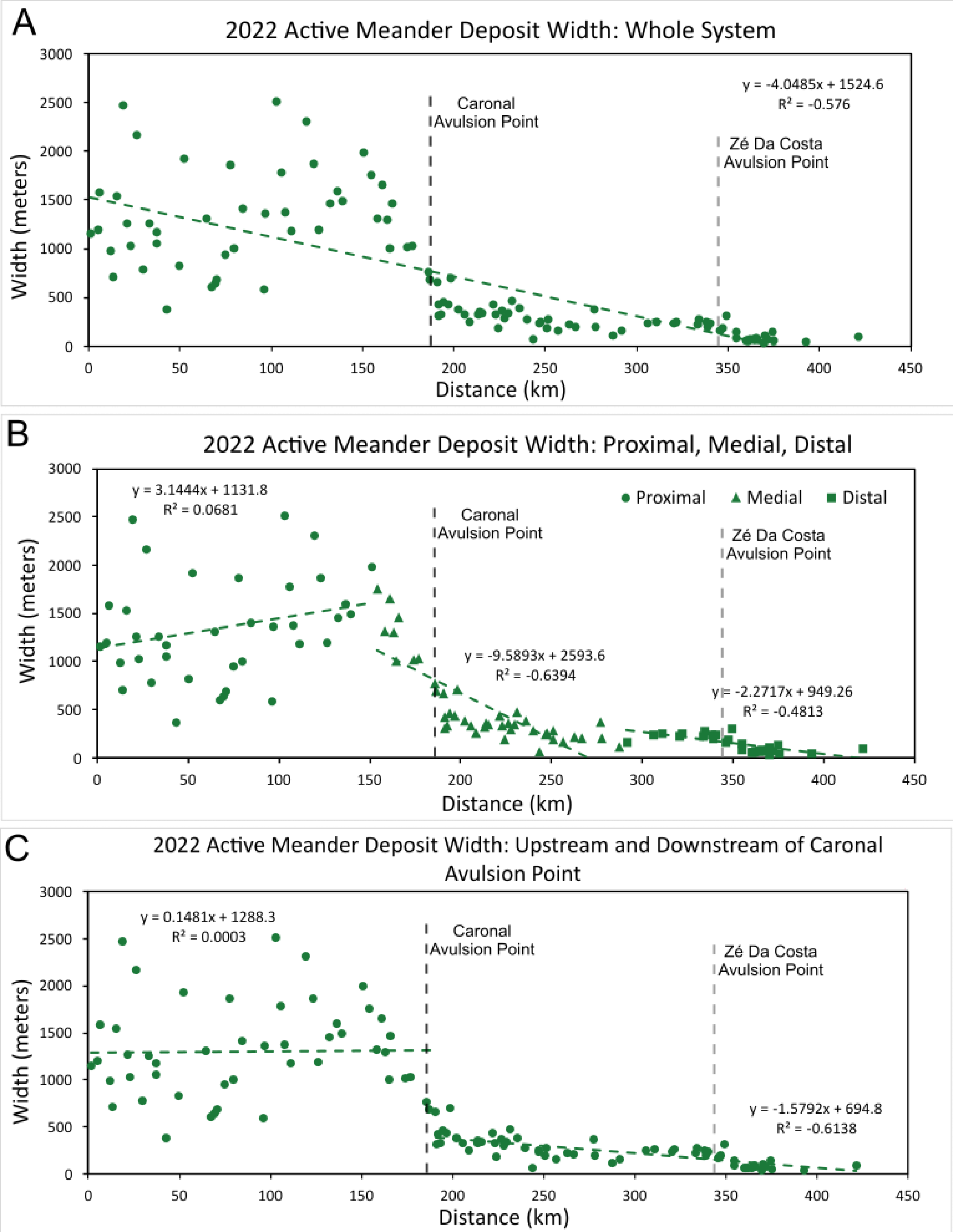

Figure 3.11. Active meander deposit width across the whole system (A), in proximal, medial, and distal zones (B), and upstream and downstream of the Caronal avulsion point (C). Each graph displays R^2 values and equations of the line.

Table 3.8. Active meander deposit area, length, and width data with statistics and R^2 values over the whole system, in proximal, medial, and distal DFS zones, and upstream and downstream of the Caronal avulsion point.

	Max	Min	Median	Mean	SD	R^2
Active Deposit Area (km^2)	2.29	0.00084	0.029	0.37	0.50	-0.5042
Proximal Area	2.29	0.22	0.98	0.92	0.46	0.0693
Medial Area	1.17	0.0022	0.027	0.16	0.27	-0.4632
Distal Area	0.017	0.00084	0.0034	0.0063	0.0051	-0.4996
Area Upstream of Avulsion Point	2.29	0.12	0.75	0.84	0.45	0.0125
Area Downstream of Avulsion Point	0.049	0.00084	0.011	0.014	0.012	-0.5788
Active Deposit Length (m)	1917.22	12.37	77.26	377.01	457.18	-0.5559
Proximal Length	1917.22	332.75	812.12	865.25	405.55	0.0003
Medial Length	1196.94	25.91	71.77	207.92	282.20	-0.4373
Distal Length	75.64	12.37	34.31	35.15	16.63	-0.3703
Length Upstream of Avulsion Point	1917.22	266.31	693.93	810.52	394.58	0.0414
Length Downstream of Avulsion Point	151.07	12.37	44.24	50.22	27.41	-0.4674
Active Deposit Width (m)	2522.15	43.32	383.67	692.54	631.06	-0.5670
Proximal Width	2522.15	384.03	1269.68	1343.08	528.74	0.0681
Medial Width	1761.36	75.56	364.19	536.10	420.68	-0.6394
Distal Width	319.01	43.32	102.96	147.29	81.73	-0.4813
Width Upstream of Avulsion Point	2522.15	384.03	1267.12	1301.75	501.43	0.0003
Width Downstream of Avulsion Point	712.69	43.32	233.43	233.30	134.95	-0.6138

3.2.7 Abandoned Meander Deposit Dimensions

Abandoned meander deposits are differentiated from active meander deposits as they are not attached to the active channel (the 2022 channel) and are not influenced by the Caronal avulsion as they are much larger than active deposits. As such, abandoned meander deposits are not compared upstream and downstream of the Caronal avulsion point. Further details on the differentiation between active and abandoned deposits, and information on how these deposit measurements were collected can be found in methods section 2.4.

3.2.7.1 Meander Deposit Area

Across the whole 2022 system abandoned meander deposit areas range in size from 0.024 km^2 to 1.24 km^2, with a median of 0.24 km^2, a mean of 0.30 km^2, and a standard deviation of 0.21 km^2 (Table 3.9). There is a slight downstream decrease in meander deposit area as demonstrated by a linear trendline with a very weak negative correlation (R^2 = -0.13) (Figure 3.12A).

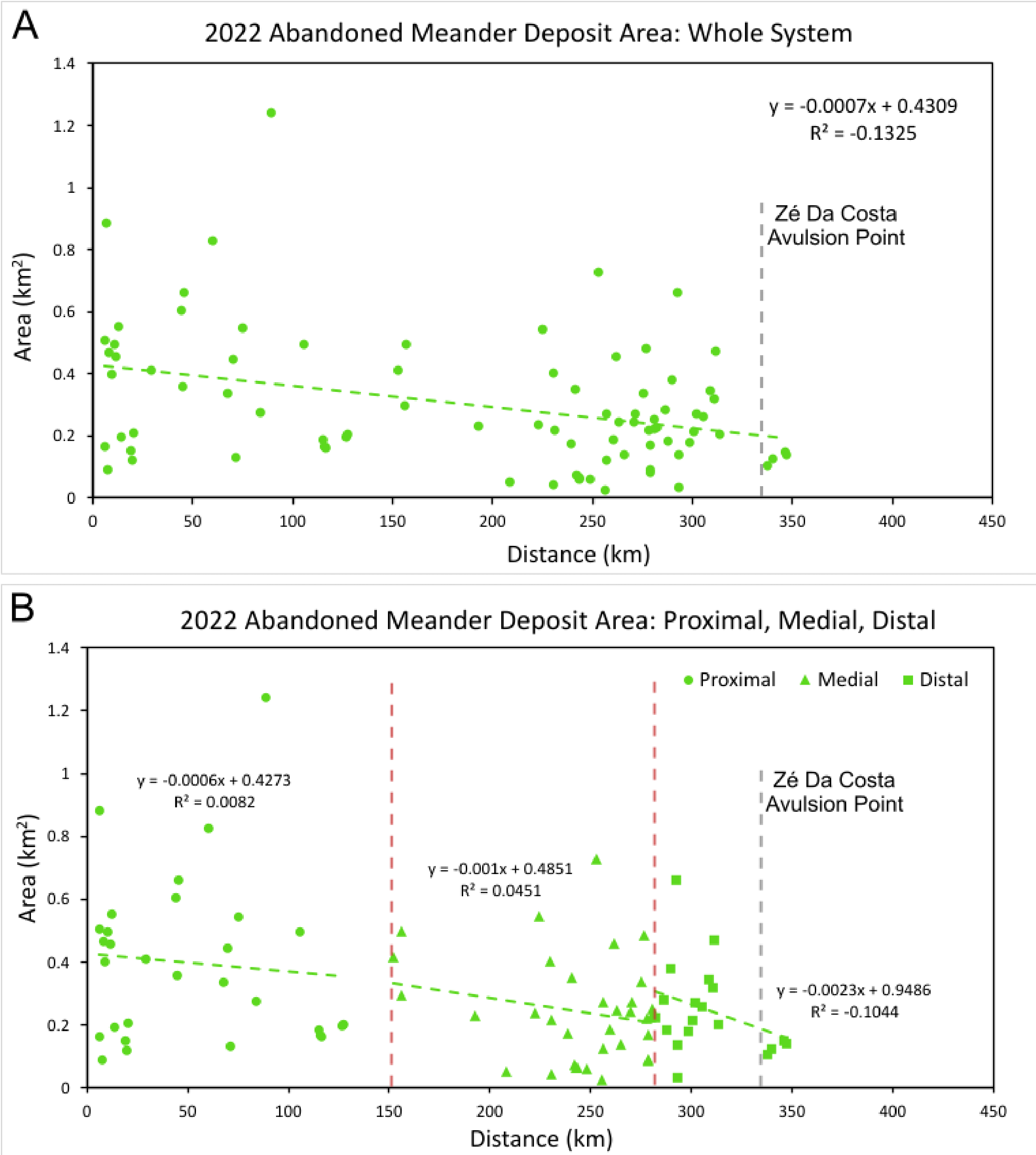

Figure 3.12. Abandoned meander deposit area across the whole system (A), and in proximal, medial, and distal DFS zones (B). Each graph displays R^2 values and equations of the line. The Zé Da Costa avulsion point is also marked by a grey dashed line. Red dashed-lines are used to delineate the three DFS zones as a cluster of data points between the medial and distal zones makes it more difficult to identify the boundary between these zones.

In the proximal DFS zone, abandoned meander deposit areas range in size from 0.092 km^2 to 1.24 km^2, with a median of 0.38 km^2, a mean of 0.40 km^2, and a standard deviation of 0.26 km^2 (Table 3.9). There is no correlation in area in the proximal zone, as demonstrated by the R^2 value ($R^2 < 0.01$) (Figure 3.12B). In the medial zone, meander deposit areas range in size from 0.024 km^2 to 0.73 km^2, with a median of 0.23 km^2, a mean of 0.24 km^2, and a standard deviation of 0.16 km^2 (Table 3.9). There is no correlation in deposits as demonstrated by the R^2 value ($R^2 = 0.04$) (Figure 3.12B). In the distal zone, meander deposit areas range in size from 0.033 km^2 to 0.66 km^2, with a median of 0.22 km^2, a mean of 0.25 km^2, and a standard deviation of 0.14 km^2 (Table 3.9). There is also no correlation in meander deposit size demonstrated by the R^2 value ($R^2 = 0.01$) (Figure 3.12B).

3.2.7.2 Meander Deposit Length

Across the whole 2022 system abandoned meander deposit lengths range from 166.29 m to 1306.71 m, with a median of 498.08 m, a mean of 542.58 m, and a standard deviation of 259.21 m (Table 3.9). There is no correlation in meander length data across the 2022 system as demonstrated by the R^2 value ($R^2 = 0.02$) (Figure 3.13A).

In the proximal DFS zone, abandoned meander deposit lengths range from 218.21 m to 1306.71 m, with a median of 671.79 m, a mean of 696.64 m, and a standard deviation of 286.77 m (Table 3.9). There is no correlation in meander deposit length data as demonstrated by the R^2 value ($R^2 = 0.01$) (Figure 3.13B). In the medial zone, meander deposit lengths range from 168.95 m to 979.17 m, with a median of 480.76 m, a mean of 460.82 m, and a standard deviation of 205.34 m (Table 3.9). There is also no correlation in the medial zone as demonstrated by the R^2 value ($R^2 = 0.02$) (Figure 3.13B). In the distal zone, meander deposit lengths range from 166.29 m to 735.31 m, with a median of 412.71 m, a mean of 445.63 m, and a standard deviation of 171.38 m (Table 3.9). Meander deposit lengths decrease slightly downstream in the distal zone as demonstrated by a linear trendline with a very weak negative correlation ($R^2 = -0.16$) (Figure 3.13B).

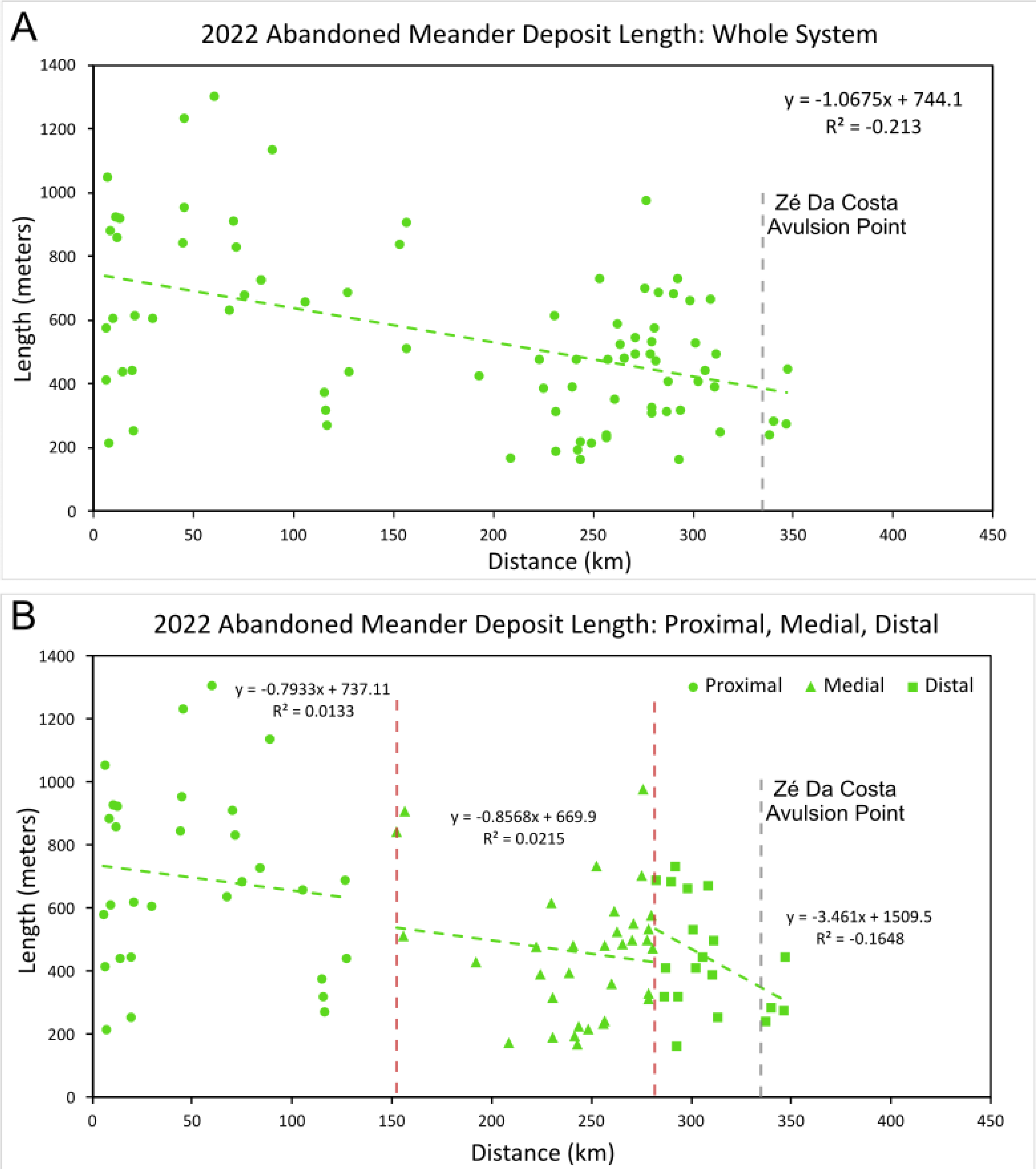

Figure 3.13. Abandoned meander deposit length across the whole system (A), and in proximal, medial, and distal DFS zones (B). Each graph displays R^2 values and equations of the line. The Zé Da Costa avulsion point is also marked by a grey dashed line. Red dashed-lines are used to delineate the three DFS zones as a cluster of data points between the medial and distal zones makes it more difficult to identify the boundary between these zones.

3.2.7.3 Meander Deposit Width

Across the whole 2022 system abandoned meander deposit widths range from 142.86 m to 1355.22 m, with a median of 615.95 m, a mean of 638.80 m, and a

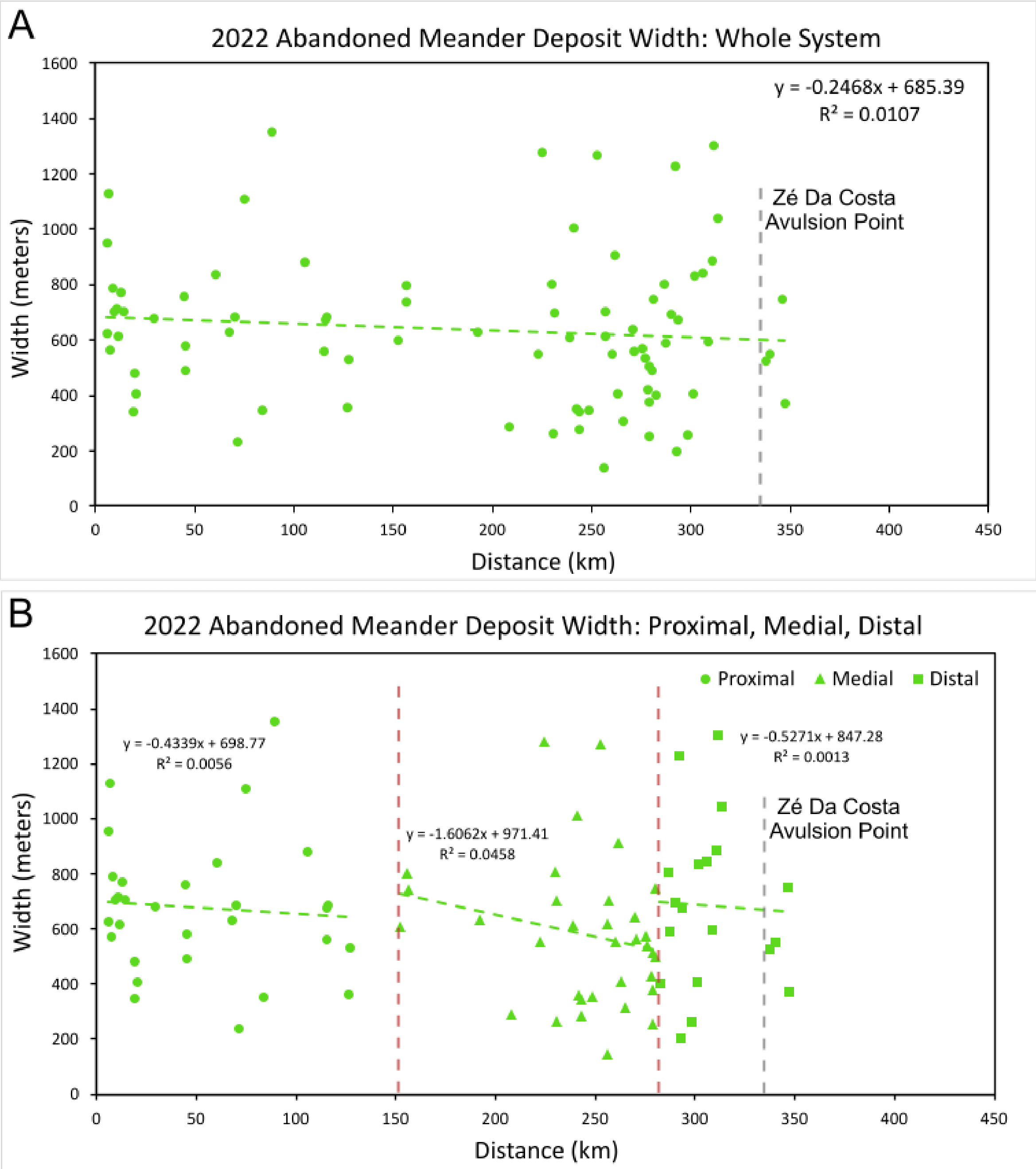

Figure 3.14. Abandoned meander deposit width across the whole system (A), and in proximal, medial, and distal DFS zones (B). Each graph displays R^2 values and equations of the line. The Zé Da Costa avulsion point is also marked by a grey dashed line. Red dashed-lines are used to delineate the three DFS zones as a cluster of data points between the medial and distal zones makes it more difficult to identify the boundary between these zones.

standard deviation of 267.82 m (Table 3.9). There is no correlation in meander deposit width data across the system as demonstrated by the R^2 value (R^2 = 0.01) (Figure 3.14A).

In the proximal DFS zone, abandoned meander deposit widths range from 238.58 m to 1355.22 m, with a median of 680.13 m, a mean of 676.63 m, and a standard deviation of 241.20 m (Table 3.9). There is no correlation in meander deposit width data in the proximal zone, as demonstrated by the R^2 value ($R^2 < 0.01$) (Figure 3.14B). In the medial zone, meander deposit widths range from 142.86 m to 1281.96 m, with a median of 559.80 m, a mean of 579.46 m, and a standard deviation of 263.68 m (Table 3.9). There is no correlation in width data in the medial zone as demonstrated by the R^2 value ($R^2 = 0.05$) (Figure 3.14B). In the distal zone, meander deposit widths range from 203.81 m to 1307.38 m, with a median of 675.95 m, a mean of 685.24 m, and a standard deviation of 293.86 m (Table 3.9). There is no correlation in meander deposit width data in the distal zone as demonstrated by the R^2 value ($R^2 < 0.01$) (Figure 3.14B).

Table 3.9. Abandoned meander deposit data for area, length, and width with statistics and R^2 values over the whole system and in proximal, medial, and distal DFS zones.

	Max	Min	Median	Mean	SD	R^2
Abandoned Deposit Area (km^2)	1.24	0.024	0.24	0.30	0.21	-0.1325
Proximal Area	1.24	0.092	0.38	0.40	0.26	0.0082
Medial Area	0.73	0.024	0.23	0.24	0.16	0.0451
Distal Area	0.66	0.033	0.22	0.25	0.14	-0.1044
Abandoned Deposit Length (m)	1306.71	166.29	498.08	542.58	259.21	-0.2130
Proximal Length	1306.71	218.21	671.79	696.64	286.77	0.0133
Medial Length	979.17	168.95	480.76	460.82	205.34	0.0215
Distal Length	735.31	166.29	412.71	445.63	171.38	-0.1648
Abandoned Deposit Width (m)	1355.22	142.86	615.95	638.80	169.56	0.0107
Proximal Width	1355.22	238.58	680.13	676.63	241.20	0.0056
Medial Width	1281.96	142.86	559.80	579.46	263.68	0.0458
Distal Width	1307.38	203.81	675.95	685.24	293.86	0.0013

3.2.8 Summary of 2022 Taquari DFS (During Avulsion)

Within the 2022 system, there are many downstream trends present across variables. Firstly, the elevation of the 2022 channel decreases downstream steadily with no obvious convex or concave profile except for a slight concave profile in the distal zone where the Taquari DFS reaches the axial Paraguay Fluvial System. The slope gradient is highest in the proximal zone (-0.00027 m/m; Figure 3.4, Table 3.3) and upstream of the Caronal avulsion point (-0.00028 m/m) and lowest in the distal zone (-0.00018 m/m), and downstream of the Caronal avulsion point (-0.00022 m/m).

For 2022 channel width, there is also a steady decrease in channel width downstream across the whole system (R^2 = -0.76; Figure 3.5A, Table 3.4) with no correlation in the proximal zone (R^2 < 0.01; Figure 3.5B, Table 3.4) and a steady decrease in width in medial (R^2 = -0.61) and distal zones (R^2 = -0.60). The largest channel width values are found in the proximal zone (maximum width = 309.88 m; Table 3.4) with the lowest width values found in the distal zone (minimum width = 15.26 m) as the channel experiences a significant decrease in width downstream of the Caronal avulsion point. Compared upstream and downstream of the avulsion point, there is a slight decrease in channel width upstream of the avulsion point (R^2 = -0.14 Figure 3.5C, Table 3.4) and only a general decrease in channel width downstream of the avulsion point (R^2 = -0.30) which differs from the steady decrease in channel width observed in medial and distal zones. Upstream and downstream of the avulsion point there is also a large difference in mean 2022 channel width as mean width changes from 217.75 m upstream of the avulsion point to 34.11 m downstream of the avulsion point (Table 3.4).

Active channel belt width also steadily decreases in width downstream (R^2 = -0.77; Figure 3.6A, Table 3.5), with a general decrease in width in proximal, medial and distal zones (R^2 = -0.59, -0.54, and -0.46, respectively; Figure 3.6B, Table 3.5). Downstream of the Caronal avulsion point, there is a more general decrease in width downstream (R^2 = -0.26; Figure 3.6C, Table 3.5) compared to upstream of the avulsion point (R^2 = -0.54). Similar to 2022 channel width, the largest active channel belt width values are found in the proximal zone (maximum width = 3693.40 m; Table 3.5) with the lowest width values in the distal zone (minimum width = 47.32 m). There is also a large difference in mean active channel belt width upstream and downstream and downstream of the avulsion point as mean width upstream of the avulsion point is 2158.27 m whereas downstream of the avulsion point mean width is 184.95 m (Table 3.5).

Channel belt width shares the same width dimensions as the active channel belt width upstream of the Caronal avulsion point and downstream of the Zé da Costa avulsion point. However, the general trends observed downstream for the channel belt are different as there is only a general decrease in channel belt width downstream (R^2 = -0.48; Figure 3.7A, Table 3.6). The proximal zone has the same downstream trends as the active channel belt width (R^2 = -0.59; Figure 3.7B, Table 3.6). The medial zone shows a slight increase in channel belt width downstream (R^2 = 0.14), whereas the distal zone shows a steady decrease in channel belt width downstream (R^2 = -0.73). This decrease in width in the distal zone is similar to the decrease in width downstream of the Caronal avulsion point (R^2 = -0.77; Figure 3.7C, Table 3.6). Upstream of the Caronal avulsion, however, there is only a general decrease in width downstream (R^2 = -0.51). The channel belt has the same maximum and minimum width values as the active channel belt (3693.40 m and 47.32 m, respectively; Table 3.6).

For 2022 channel sinuosity, there is a slight decrease in sinuosity downstream (R^2 = -0.12; Figure 3.8A, Table 3.7) and no correlation in proximal and medial zones (R^2 < 0.01 and 0.03, respectively (Figure 3.8B, Table 3.7)). The distal zone shows a very slight increase in sinuosity downstream (R^2 = 0.13). There is also a slight decrease in sinuosity upstream of the Caronal avulsion point (R^2 = -0.19; Figure 3.8C, Table 3.7), contrasting the high variability in the proximal and medial zones. Downstream of the avulsion point there is no correlation in sinuosity (R^2 = -0.08). Similar to the previously described variables in the 2022 system, the highest sinuosity values are found in the proximal zone (maximum sinuosity = 2.20; Table 3.7). However, the lowest sinuosity values are found in the medial zone (minimum sinuosity = 1.11) instead of the distal zone (minimum sinuosity = 1.16).

For active meander deposit dimensions, there is a general decrease in meander deposit area, length, and width (R^2 = -0.50, -0.56, and -0.58, respectively (Figure 3.9A, Figure 3.10A, Figure 3.11A, Table 3.8)). Within each DFS zone, deposit area, length, and width show no correlation in the proximal zone (R^2 = 0.07, < 0.01, and 0.07, respectively (Figure 3.9B, Figure 3.10B, Figure 3.11B, Table 3.8)). In the medial zone, there is a general decrease in deposit area and length (R^2 = -0.46 and -0.44, respectively), and a steady decrease in deposit width (R^2 = -0.64). Similarly, in the distal zone, there is a general decrease in meander deposit area, length, and width (R^2 = -0.50, -0.37, -0.48, respectively). Upstream of the Caronal avulsion point, there is no correlation in meander dimensions (R^2 = 0.01 for area, 0.04 for length, and < 0.01 for width (Figure 3.9C, Figure 3.10C, Figure 3.11C, Table 3.8)) compared to downstream of the avulsion point where there is a general decrease in meander deposit area and length (R^2 = -0.58 and -0.47, respectively) and a steady decrease in deposit width downstream (R^2 = -0.61). The largest deposit dimensions are found in the proximal zone (2.29 km^2 for area, 1917.22 m for length, and 2522.15 m for width; Table 3.8) and the smallest deposit dimensions are found in the distal zone (0.00084 km^2 for area, 12.37 m for length, and 319.01 m for width). The active meander deposits are another example of an active variable that experiences a large decrease in dimensions downstream of the Caronal avulsion point. Upstream of the avulsion point the mean area of active deposits is 0.84 km^2 whereas downstream mean area is 0.014 km^2 (Table 3.8).

For abandoned meander deposit dimensions, there is only a slight decrease in deposit area and length downstream (R^2 = -0.13 and -0.21, respectively (Figure 3.12A, Figure 3.13A, Table 3.9) and no correlation in deposit width downstream (R^2 = 0.01; Figure 3.14A, Table 3.9). For deposit area, length, and width, there is no correlation in the proximal zone (R^2 < 0.01, 0.01, < 0.01, respectively (Figure 3.12B, Figure 3.13B, Figure 3.14B, Table 3.9) and the medial zone (R^2 = 0.05, 0.02, and 0.05, respectively). There is a slight decrease in deposit area and length in the distal zone (R^2 = -0.10 and -0.16, respectively) and no correlation in deposit width in the distal zone (R^2 < 0.01). Similar to the active deposits, the proximal zone has the highest values for area, length, and width (maximum = 1.24 km^2, 1306.71 m, and 1355.22 m, respectively (Table 3.9)). However, for deposit area and width, the lowest values are in the medial zone (minimum = 0.024 km^2 and 142.86 m, respectively) and for deposit length the lowest value is in the distal zone (166.29 m) which is only slightly smaller than the medial zone (168.95 m).

3.3 2022 Taquari DFS Comparisons: Ratios

On the 2022 Taquari DFS, 2022 channel width is compared to active channel belt width to understand the change in width dimensions downstream across both of these variables. Similarly, the active channel belt width is compared to the channel belt width downstream to understand the difference in width between these two channel belts. The width of each channel belt represents the change in migration capacity of the active channel following a decrease in discharge in the channel (as outlined in methods section 2.3). Therefore, this allows a better understanding of the adjustment of a channel belt as channel discharge changes, as will be discussed further in the following discussion chapter.

3.3.1 2022 Channel Width and 2022 Active Channel Belt Width

Across the whole 2022 system, the ratio between 2022 channel width and active channel belt width ranges from 0.05 to 0.41, with a median of 0.14, a mean of 0.16, and a standard deviation of 0.08 (Table 3.10). The ratio between active channel width and active channel belt width generally increases downstream as the active channel belt becomes closer in width to the active channel. This is demonstrated by a linear trendline with a moderate positive correlation (R^2 = 0.41) (Figure 3.15A).

In the proximal DFS zone, the ratio between 2022 channel width and active channel belt width ranges from 0.05 to 0.17, with a median of 0.09, a mean of 0.11, and a standard deviation of 0.04 (Table 3.10). The ratio increases downstream as demonstrated by a linear trendline with a moderate positive correlation (R^2 = 0.50) (Figure 3.15B). In the medial zone, the ratio between 2022 channel width and active channel belt width ranges from 0.09 to 0.35, with a median of 0.17, a mean of 0.17, and a standard deviation of 0.07 (Table 3.10).

The ratio increases downstream as demonstrated by a linear trendline with a moderate positive correlation (R^2 = 0.46) (Figure 3.15B). In the distal zone, the ratio between 2022 channel width and active channel belt width ranges from 0.11 to 0.41, with a median of 0.19, a mean of 0.21, and a standard deviation of 0.09 (Table 3.10). The ratio shows no correlation in this zone as demonstrated by the R^2 value (R^2 = 0.08) (Figure 3.15B).

Upstream of the Caronal avulsion point, the ratios range from 0.05 to 0.17, with a median of 0.10, a mean of 0.11, and a standard deviation of 0.03 (Table 3.10). The ratio increases slightly downstream as demonstrated by a linear trendline with a weak positive correlation (R^2 = 0.20) (Figure 3.15C). Downstream of the Caronal avulsion point, the ratios range from 0.10 to 0.41, with a median of 0.19, a mean of 0.21, and a standard deviation of 0.08 (Table 3.10). The ratio shows no correlation downstream of the avulsion point as demonstrated by the R^2 value (R^2 = 0.05) (Figure 3.15C).

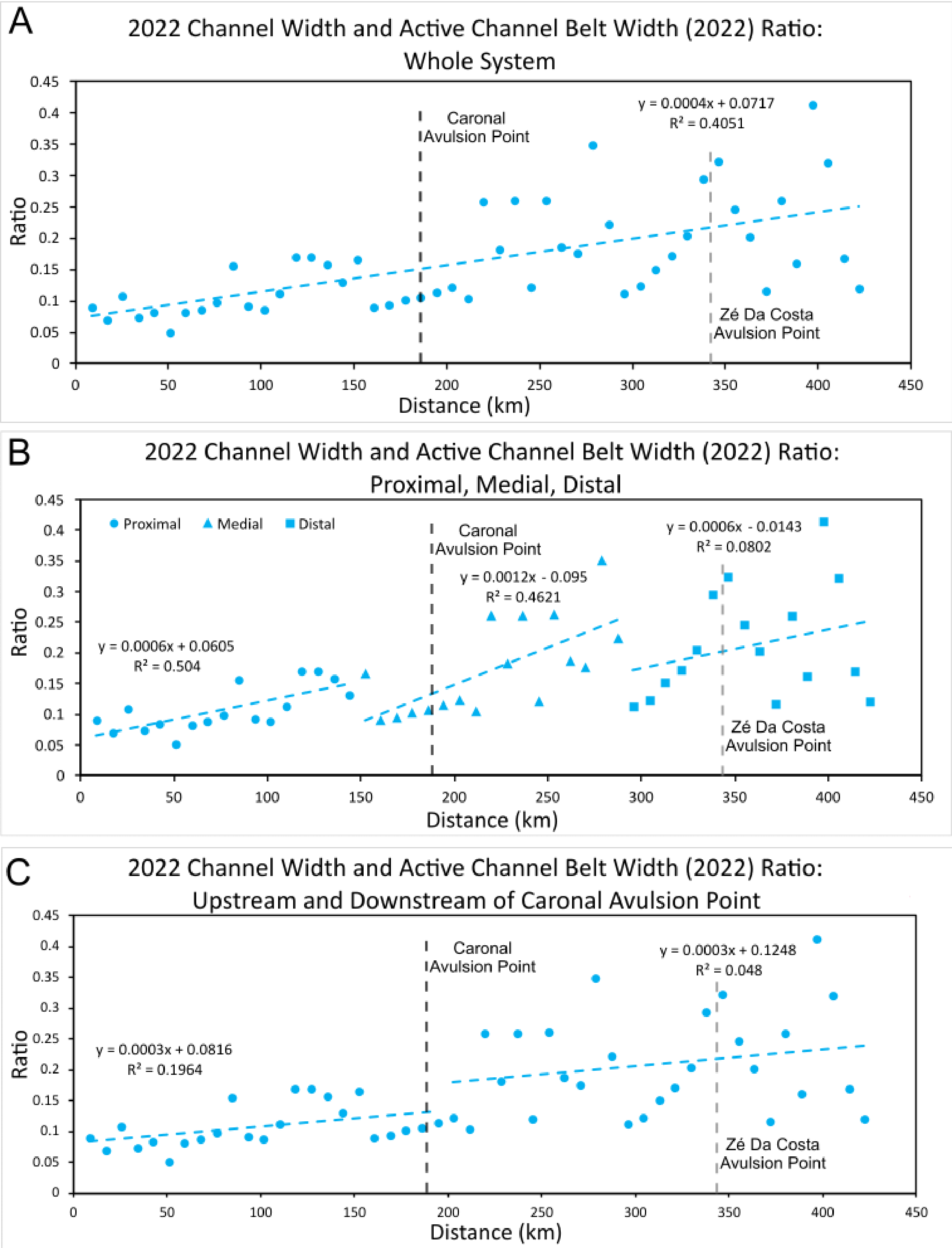

Figure 3.15. Ratio between 2022 channel width and 2022 active channel belt width across the whole system (A), in proximal, medial, and distal DFS zones (B), and upstream and downstream of the Caronal avulsion point (C). Each graph displays R^2 values and equations of the line.

3.3.2 2022 Active Channel Belt Width and 2022 Channel Belt Width

Across the whole 2022 system, the ratio between active channel belt width and channel belt width ranges from 0.04 to 1.00, with a median of 1.00, a mean of 0.68, and a standard deviation of 0.42 (Table 3.10). The active channel belt and the channel belt are the same width upstream of the Caronal avulsion point and downstream of the Zé da Costa avulsion point making the ratio in these reaches 1:1 (Figure 3.16A). Between both avulsion points the channel belts differ in width, however, there are slight negative and positive skews in the medial and distal DFS zones, respectively, where these zones include areas where the ratio is 1.00. Across the whole 2022 system, the ratio between active channel belt width and channel belt width decreases slightly downstream due to the negative skew in data upstream of the Caronal avulsion point and the positive skew in the data downstream of the Zé da Costa avulsion point. This is demonstrated by a linear trendline with a very weak negative correlation (R^2 = -0.11) (Figure 3.16A).

In the proximal DFS zone, the ratio between active channel belt width and channel belt width is 1.00 across the whole zone (Table 3.10). In the medial zone, the ratio ranges from 0.04 to 1.00, with a median of 0.11, a mean of 0.39, and a standard deviation of 0.42 (Table 3.10). As outlined previously, the active channel belt and the channel belt separate into two separate channel belts in the medial zone. This results in a slight negative skew in data as the ratio starts at 1.00 and decreases downstream as the width of both of the channel belts change. As the active channel belt becomes smaller than the channel belt downstream, the ratio shows a sharp decrease from 1.00 (upstream of the avulsion point) to being fairly consistently below ~0.20 (downstream of the avulsion point). This sharp decrease in ratio is demonstrated by a linear trendline with a strong negative correlation (R^2 = -0.72), and the low ratio downstream of the avulsion point is demonstrated by the low median value (0.11) (Figure 3.16B). In the distal zone, the ratio ranges from 0.17 to 1.00, with a median of 1.00, a mean of 0.65, and a standard deviation of 0.40 (Table 3.10). In the distal zone, the channel belts combine again downstream of the Zé da Costa avulsion point as the ratio becomes 1.00 therefore causing a slight positive skew in data (Figure 3.16B). Due to the skew in data, there is a sharp increase in

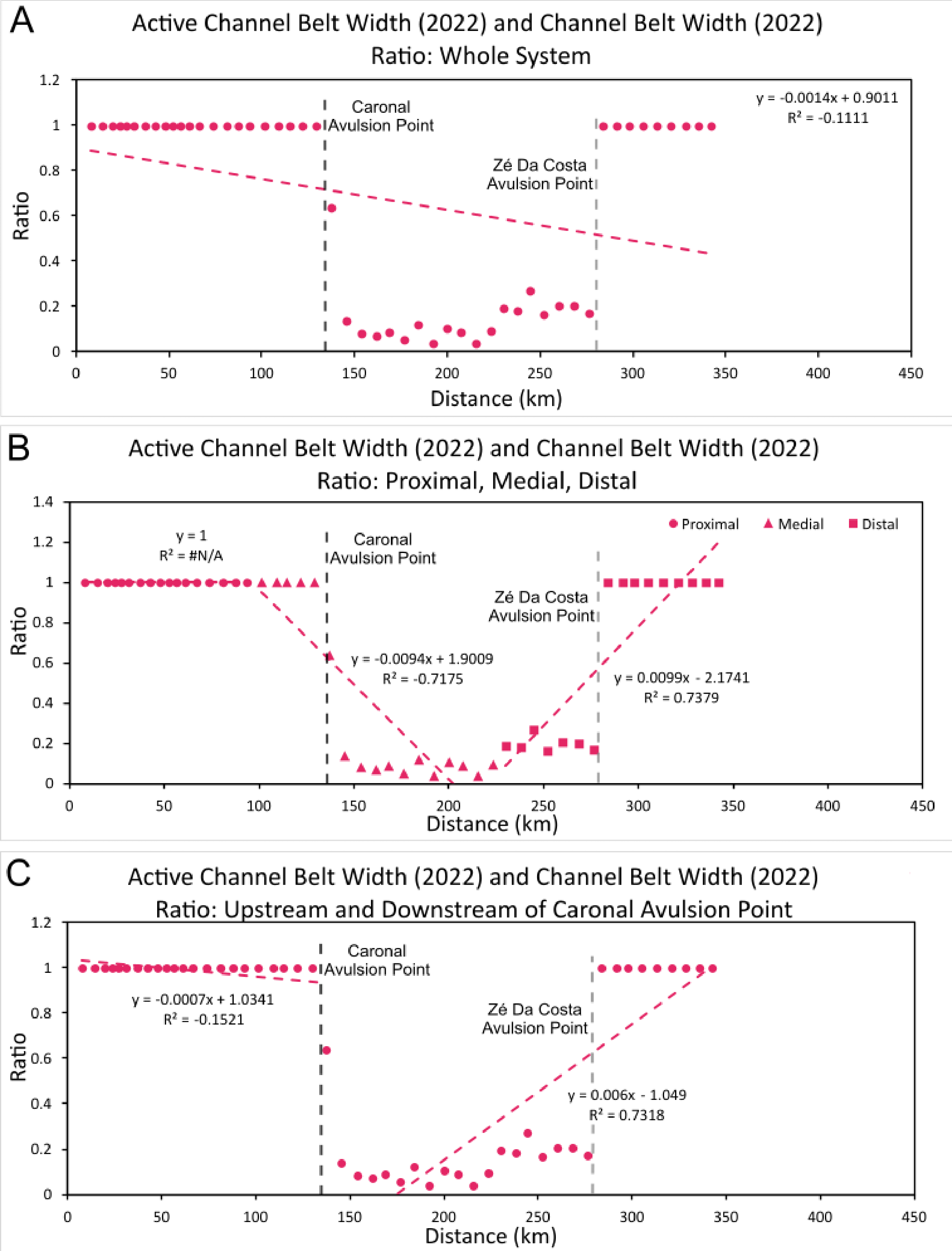

Figure 3.16. Ratio between 2022 active channel belt width and 2022 channel belt width across the whole system (A), in proximal, medial, and distal DFS zones (B), and upstream and downstream of the Caronal avulsion point (C). Each graph displays R^2 values and equations of the line.

ratio downstream as the channel belts become closer in width again. This is demonstrated by a linear trendline with a strong positive correlation ($R^2 = 0.74$) (Figure 3.16B).

Upstream of the Caronal avulsion point, both channel belts are the same width. However, one outlying data point with a ratio ~0.60 marks where the channel belts split into two separate channel belts resulting in slightly negatively skewed data. As such, the ratio between active channel belt width and channel belt width ranges from 0.64 to 1.00, with a median of 1.00, a mean of 0.98, and a standard deviation of 0.07 (Table 3.10). As a result of the outlying datapoint, there is a slight downstream decrease in ratio demonstrated by a linear trendline with a weak negative correlation (R^2 = -0.15) (Figure 3.16C). Downstream of the Caronal avulsion point, both channel belts become the same width again downstream of the Zé da Costa avulsion point resulting in positively skewed data (Figure 3.16C). Downstream of the Caronal avulsion point, ratios range from 0.04 to 1.00, with a median of 0.18, a mean of 0.42, and a standard deviation of 0.41 (Table 3.10). As a result of the positively skewed data, the ratio increases sharply downstream as demonstrated by a linear trendline with a strong positive correlation (R^2 = 0.73) (Figure 3.16C).

Table 3.10. Ratio and statistics data for 2022 channel width and 2022 active channel belt width, and 2022 active channel belt width and 2022 channel belt width across the whole system, in proximal, medial, and distal DFS zones and upstream and downstream of the Caronal avulsion point with R^2 and p-values.

	Max	Min	Median	Mean	SD	R^2	Mann-Whitney
2022 Channel Width/ 2022 Active Channel Belt Width Ratio	0.41	0.05	0.14	0.16	0.08	0.4051	p < 0.01
Proximal Ratio	0.17	0.05	0.09	0.11	0.04	0.5040	p < 0.01
Medial Ratio	0.35	0.09	0.17	0.17	0.07	0.4621	p < 0.01
Distal Ratio	0.41	0.11	0.19	0.21	0.09	0.0802	p < 0.01
Ratio Upstream of Avulsion Point	0.17	0.05	0.10	0.11	0.03	0.1964	p < 0.01
Ratio Downstream of Avulsion Point	0.41	0.10	0.19	0.21	0.08	0.0480	p < 0.01
2022 Active Channel Belt Width/ 2022 Channel Belt Width Ratio	1.00	0.04	1.00	0.68	0.42	0.1110	p = 0.01
Proximal Ratio	1.00	1.00	1.00	1.00	0.00	#N/A	p = 1.00
Medial Ratio	1.00	0.04	0.11	0.39	0.42	-0.7175	p < 0.01
Distal Ratio	1.00	0.17	1.00	0.65	0.40	0.7379	p = 0.31
Ratio Upstream of Avulsion Point	1.00	0.64	1.00	0.98	0.07	-0.1521	p = 1.00
Ratio Downstream of Avulsion Point	1.00	0.04	0.18	0.42	0.41	0.0480	p < 0.01

3.4 2022 Taquari DFS Comparisons: Statistics

Statistical analyses of data were carried out to look for relationships between variables. The non-parametric Mann-Whitney test was used due to the non-normal distribution of data for each variable. This test calculates a p-value which indicates whether the difference in medians between each dataset is statistically significant (Minitab, 2024). For all variables compared, the Mann-Whitney test was carried out at a 95% confidence interval. A p-value of < 0.05 indicates a statistically significant relationship where there is a 5% chance that this relationship is random or there is in fact no difference in variables. The lower the p-value ($p < 0.05$) the less likely it is that the relationship between the variables is random (Minitab, 2024).

3.4.1 2022 Channel Width and 2022 Active Channel Belt Width

2022 channel width and active channel belt width were compared to test for a statistically significant relationship with the null hypothesis stating that the two datasets belong to the same population. The p-value is < 0.01 therefore the difference between the medians of these two datasets is statistically significant and the null hypothesis can be rejected. The result of this statistical test reveals that as 2022 channel width changes downstream, active channel belt width also

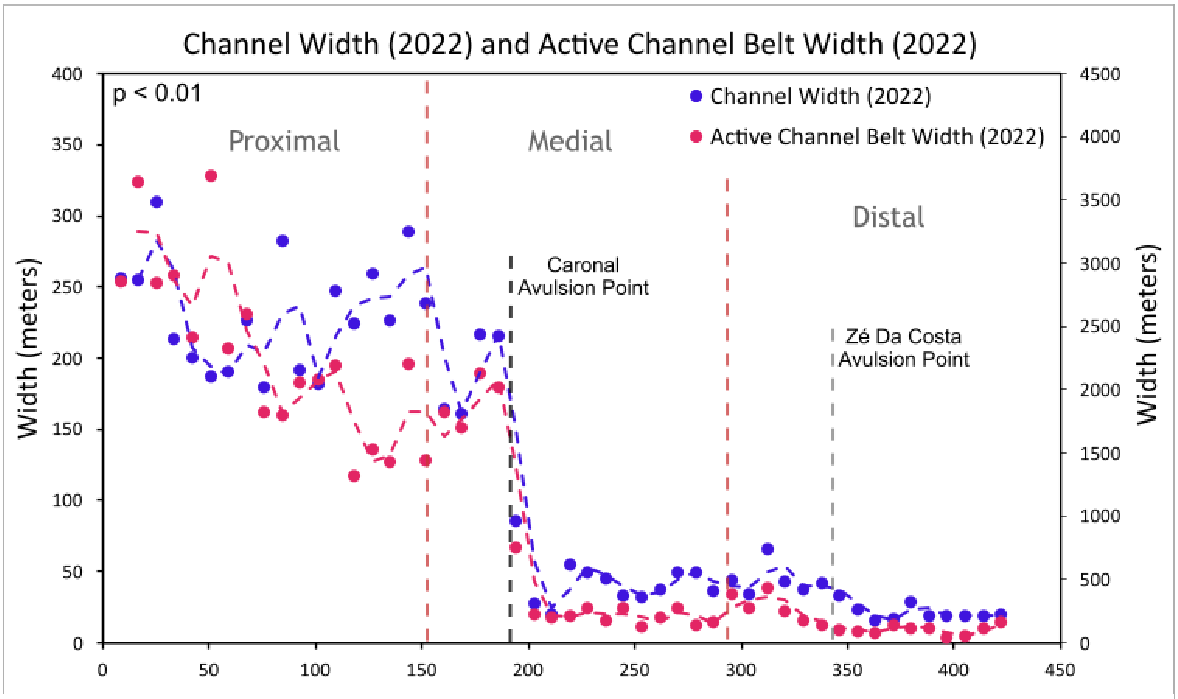

Figure 3.17. Comparison between 2022 channel width and 2022 active channel belt width with the p-value. Red dashed-lines delineate proximal, medial, and distal DFS zones. The location of the Caronal avulsion point and the Zé da Costa avulsion point are also marked by grey dashed-lines.

changes in relation to the channel. 2022 channel width and active channel belt width were also compared between proximal, medial, and distal DFS zones, and upstream and downstream of the Caronal avulsion point. For each of these comparisons the p-value is < 0.01 which indicates a statistically significant relationship is present in each area downstream (Figure 3.17; Table 3.10).

3.4.2 Active Channel Belt Width and 2022 Channel Belt Width

Active channel belt width and channel belt width were compared with the null hypothesis stating that the two datasets belong to the same population. The p-value is 0.01 therefore the difference between the medians of these two datasets is statistically significant and the null hypothesis can be rejected. The result of this statistical test reveals that as active channel belt width changes downstream the difference in width between these channel belts remains significant. Analyses were done across proximal, medial, and distal DFS zones for each, and upstream and downstream of the Caronal avulsion point. These analyses revealed that there is only a statistically significant relationship in the medial zone ($p < 0.01$) and downstream of the avulsion point ($p < 0.01$). The proximal and distal DFS zones, and the reach of the system upstream of the avulsion point have p-values greater than the 0.05 confidence interval ($p = 1.00$, $p = 0.31$, and $p = 1.00$, respectively). In the proximal zone, and upstream of the

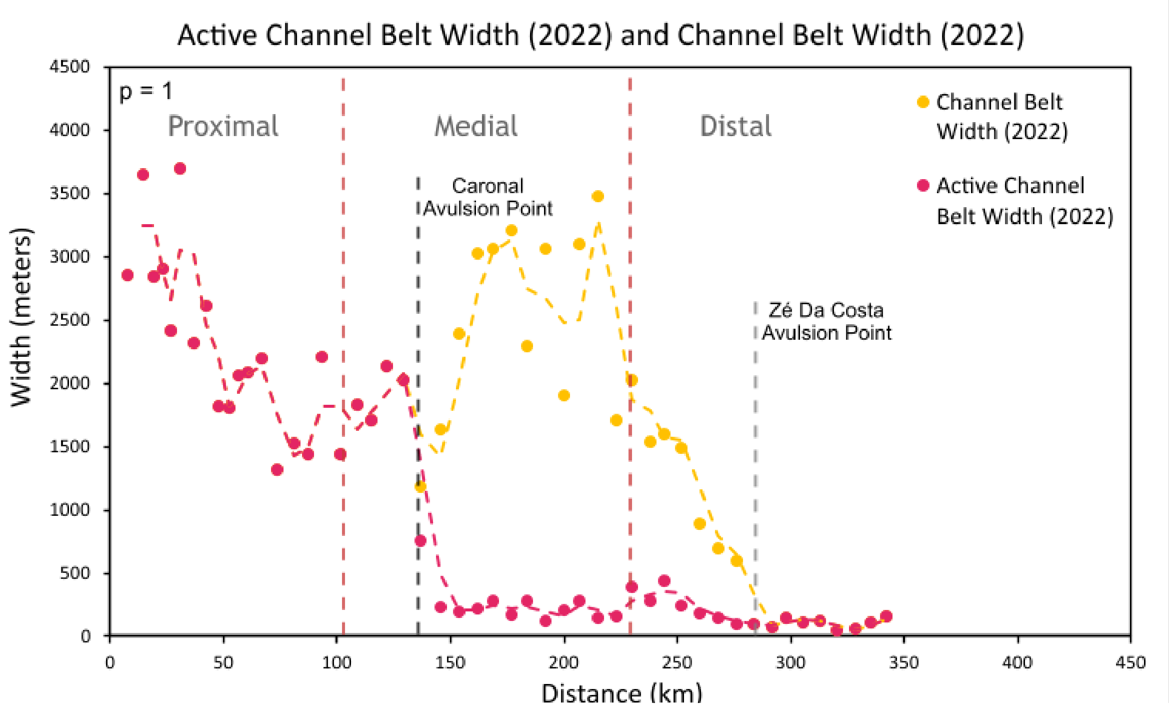

Figure 3.18. Comparison between 2022 active channel belt width and 2022 channel belt width with the p-value. Red dashed-lines delineate proximal, medial, and distal DFS zones. The location of the Caronal avulsion point and the Zé da Costa avulsion point are also marked by grey dashed-lines.

avulsion point the ratio is 1:1 so there is no difference in width observed. However, in the distal zone the two channel belts are separated initially before combining downstream of the Zé da Costa avulsion point, as previously mentioned (Figure 3.18; Table 3.10). Figure 3.18 is useful in visualising the difference in width between the active channel belt and the channel belt between the Caronal avulsion point and the Zé da Costa avulsion point where there is a large difference in width.

3.5 Summary of 2022 Taquari DFS Comparisons: Ratios and Statistics

The ratio between 2022 channel width and active channel belt width generally increases downstream across the whole system (R^2 = 0.41; Figure 3.15A, Table 3.10), and in proximal and medial DFS zones (R^2 = 0.50 and 0.46, respectively (Figure 3.15B, Table 3.10)). In the distal zone, however, there is high variability in the ratio (R^2 = 0.08). The 2022 channel is closest in width to the active channel belt in the distal zone (ratio = 0.41; Table 3.10) with the largest difference in width in the proximal zone (ratio = 0.05). Upstream of the Caronal avulsion point, there is a general increase in ratio downstream (R^2 = 0.20; Figure 3.15C, Table 3.10) compared to downstream of the avulsion point where there is no correlation in ratio (R^2 = 0.05). A statistically significant relationship is present between 2022 channel width and active channel belt width across the whole system, as well as in each DFS zone, and upstream and downstream reaches of the Caronal avulsion point ($p < 0.01$; Table 3.10).

The ratio between active channel belt width and channel belt width has a very slight decrease in ratio downstream (R^2 = -0.11; Figure 3.16A, Table 3.10) across the whole system. In the proximal zone the ratio is 1.00 across the whole zone. In the medial zone, there is a slight negative skew in data where the ratio is 1.00 upstream of the Caronal avulsion point and results in a sharp decrease in ratio downstream (R^2 = -0.72; Figure 3.16B, Table 3.10). In the distal zone there is a slight positive skew in data as the ratio is 1.00 downstream of the Zé da Costa avulsion point and results in a sharp increase in ratio downstream (R^2 = 0.74). The maximum ratio between active channel belt width and channel belt width is found where both channel belts have the same width and the ratio is 1.00 (Table 3.10). The minimum ratio, however, is found in the medial zone (0.04) where active channel belt width is significantly smaller than channel belt width. Upstream of the Caronal avulsion point there is a similar slight negative skew in data (R^2 = -0.15; Figure 3.16C, Table 3.10) as the ratio starts at 1.00 upstream of the avulsion point then decreases slightly where the channel belt polygons are split into separate polygons at the avulsion point. Downstream of the avulsion point, where there is a slight positive skew in data, the ratio shows a sharp increase downstream (R^2 = 0.73). There is a statistically significant relationship between active channel belt width and channel belt width in the medial DFS zone and downstream of the Caronal avulsion point. However, there is no relationship in the proximal zone (p = 1.00; Table 3.10), the distal zone (p = 0.31), or upstream of the Caronal avulsion point (p = 1.00) as there is too much similarity in width in these reaches.

3.6 Comparison Between the 1985 Taquari DFS (Pre-avulsion) and the 2022 Taquari DFS (During Avulsion)

This section will compare 1985 DFS data to 2022 DFS data to compare DFS dimensions before the initiation of the Caronal avulsion (which initiated between 1996 to 1997) to DFS dimensions during the Caronal avulsion. The only two variables measured across both the 1985 and 2022 systems are channel width and sinuosity. However, a comparison between 1985 channel width and 2022 channel belt width was carried out to understand whether a relationship exists between the larger 1985 channel and the 2022 channel belt which has a much larger width than the 2022 active channel belt downstream of the Caronal avulsion point.

3.6.1 Ratios

3.6.1.1 2022 Channel Width and 1985 Channel Width

Across the whole system, the ratio between 2022 channel width and 1985 channel width ranges from 0.08 to 1.01, with a median of 0.38, a mean of 0.51, and a standard deviation of 0.29 (Table 3.11). The ratio steadily decreases downstream as the difference in width between the 2022 channel width and the 1985 channel width increases, as demonstrated by a linear trendline with a strong negative correlation (R^2 = -0.65) (Figure 3.19A).

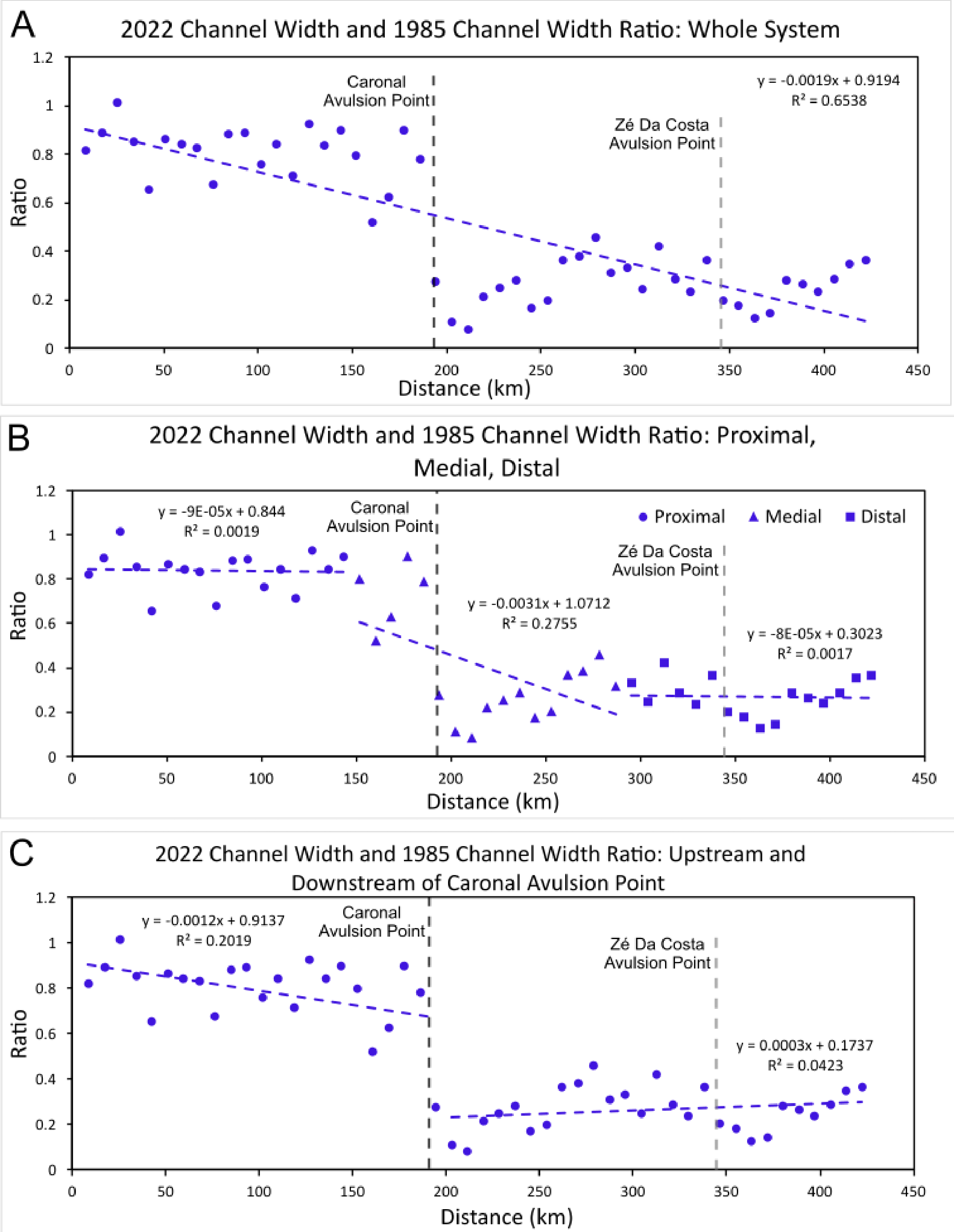

Figure 3.19. Ratio between 2022 channel width and 1985 channel width across the whole system (A), in proximal, medial, and distal DFS zones (B), and upstream and downstream of the Caronal avulsion point (C).

In the proximal DFS zone, the ratio between 2022 channel width and 1985 channel width ranges from 0.66 to 1.01, with a median of 0.85, a mean of 0.84, and a standard deviation of 0.09 (Table 3.11). There is no correlation in ratio in the proximal zone as demonstrated by the R^2 value ($R^2 < 0.01$) (Figure 3.19B). In the medial zone, the ratio ranges from 0.08 to 0.90, with a median of 0.31, a mean of 0.40, and a standard deviation of 0.24 (Table 3.11). There is slight decrease in ratio downstream as the difference in channel width increases, this is demonstrated by a linear trendline with a moderate negative correlation (R^2 = -0.28) (Figure 3.19B). In the distal zone, the ratio ranges from 0.12 to 0.42, with a median of 0.28, a mean of 0.27, and a standard deviation of 0.08 (Table 3.11). The ratio shows no correlation in the distal zone as demonstrated by the R^2 value (R^2 < 0.01) (Figure 3.19B).

Upstream of the Caronal avulsion point, the ratio between 2022 channel width and 1985 channel width ranges from 0.28 to 1.01, with a median of 0.84, a mean of 0.79, and a standard deviation of 0.15 (Table 3.11). There is a slight decrease in ratio downstream as demonstrated by a linear trendline with a weak negative correlation (R^2 = -0.20) (Figure 3.19C). Downstream of the Caronal avulsion point, the ratio ranges from 0.08 to 0.46, with a median of 0.27, a mean of 0.27, and a standard deviation of 0.09 (Table 3.11). The ratio shows no correlation downstream of the avulsion point as demonstrated by the R^2 value (R^2 = 0.04) (Figure 3.19C).

3.6.1.2 2022 Sinuosity and 1985 Sinuosity

Across the whole system, the ratio between 2022 sinuosity and 1985 sinuosity ranges from 0.75 to 1.48, with a median of 1.05, a mean of 1.07, and standard deviation of 0.16 (Table 3.11). Across the system the ratio shows no correlation downstream, as demonstrated by the R^2 value (R^2 = 0.03) (Figure 3.20A).

In the proximal DFS zone, the ratio between 2022 sinuosity and 1985 sinuosity ranges from 0.75 to 1.40, with a median of 1.04, a mean of 1.06, and a standard deviation of 0.14 (Table 3.11). The ratio shows no correlation in the proximal zone, as demonstrated by the R^2 value (R^2 < 0.01) (Figure 3.20B). In the medial zone, the ratio ranges from 0.78 to 1.32, with a median of 1.04, a mean of 1.05, and a standard deviation of 0.12 (Table 3.11). The ratio continues to show no correlation, as demonstrated by the R^2 value (R^2 = 0.03) (Figure 3.20B). In the distal zone, the ratio ranges from 0.81 to 1.47, with a median of 1.09, a mean of 1.11, and a standard deviation of 0.19 (Table 3.11). There is a general increase in ratio in the distal zone as the 2022 channel becomes more sinuous than the

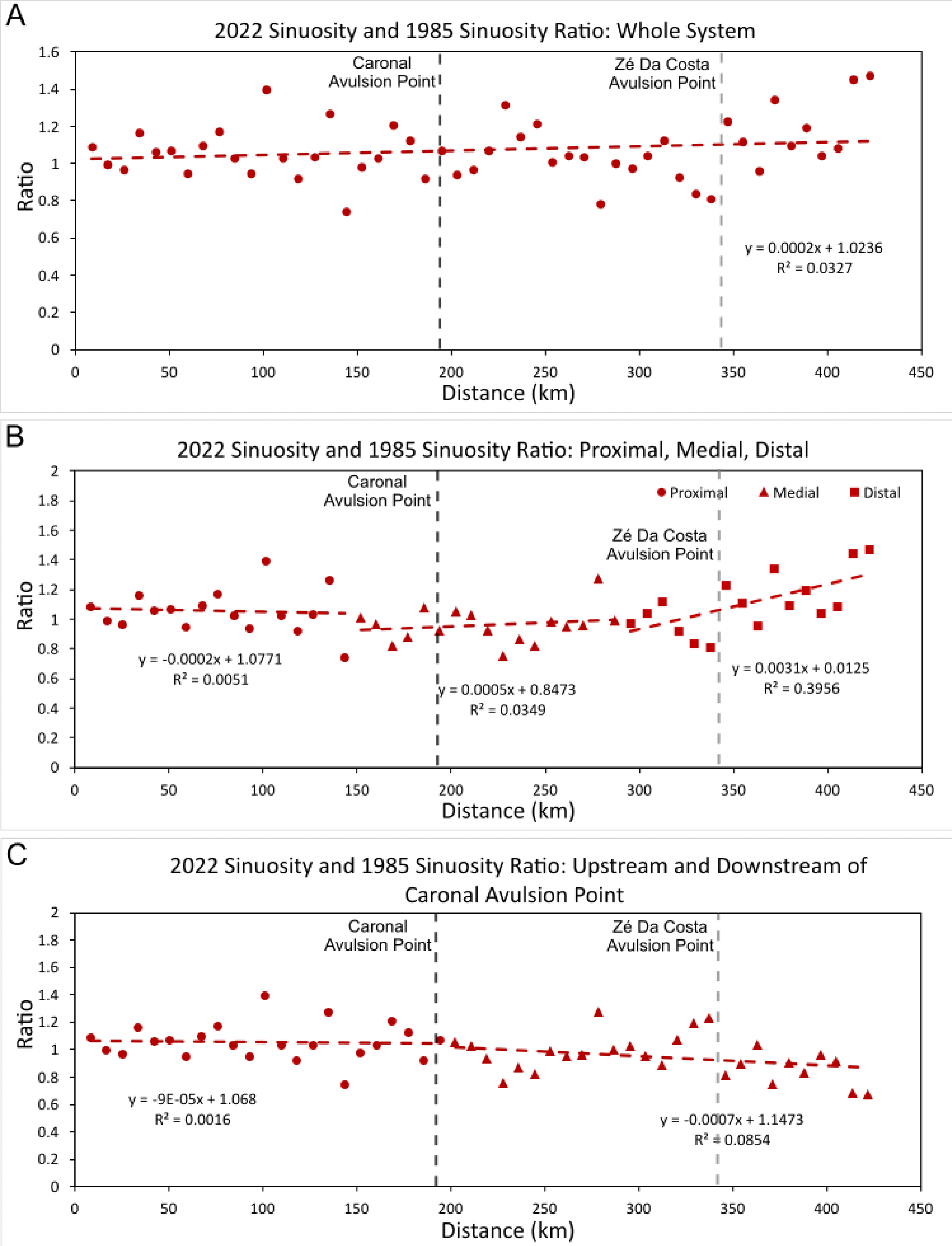

Figure 3.20. Ratio between 2022 channel sinuosity and 1985 channel sinuosity across the whole system (A), in proximal, medial, and distal DFS zones (B), and upstream and downstream of the Caronal avulsion point (C).

1985 channel. This is demonstrated by a more moderate positive correlation in data (R^2 = 0.40) (Figure 3.20B).

Upstream of the Caronal avulsion point, the ratio between 2022 sinuosity and 1985 sinuosity ranges from 0.75 to 1.40, with a median of 1.04, a mean of 1.06, and a standard deviation of 0.13. The ratio shows no correlation upstream of the avulsion point ($R^2 < 0.01$) (Figure 3.20C). Downstream of the avulsion point the ratio ranges from 0.78 to 1.48, with a median of 1.05, a mean of 1.09, and a standard deviation of 0.17. Ratio continues to show no correlation downstream of the avulsion point, as demonstrated by the R^2 value ($R^2 = 0.09$) (Figure 3.20C).

3.6.1.3 1985 Channel Width and 2022 Channel Belt Width

There is a large positive skew in this data as the 1985 channel becomes larger than the 2022 channel belt downstream of the Zé da Costa avulsion point in the distal DFS zone (Figure 3.21A). The 1985 channel was compared to the 2022 channel belt to explore the relationship between a larger pre-avulsion channel (from 1985) and the channel belt, which generally has a greater width than the active channel belt width. However, as outlined in methods section 2.3, the channel belt and the active channel belt are the same width downstream of the Zé da Costa avulsion point resulting in the channel belt becoming smaller than the 1985 channel downstream of this point. Due to the lack of evidence of a larger channel belt existing alongside the currently active channel belt, which is created by the smaller active channel, the channel belt is mapped to be the same extent as the active channel belt downstream of the Zé da Costa avulsion point (Figure 2.3E).

Across the whole system, the ratio between 1985 channel width and 2022 channel belt width ranges from 0.03 to 1.73, with a median of 0.13, a mean of 0.28, and a standard deviation of 0.39 (Table 3.11). The ratio remains relatively low downstream until the Zé da Costa avulsion point, where there is a sharp increase in ratio as the difference in size between the channel and the channel belt reduces and the 1985 channel eventually becomes larger than the 2022 channel belt. The positive skew in the data downstream results in a linear trendline with a weak positive correlation ($R^2 = 0.29$) (Figure 3.21A).

In the proximal DFS zone, the ratio between 1985 channel width and 2022 channel belt width ranges from 0.06 to 0.24, with a median of 0.11, a mean of 0.13, and a standard deviation of 0.04 (Table 3.11). The ratio remains low but generally increases downstream as demonstrated by a linear trendline with a moderate positive correlation ($R^2 = 0.47$) (Figure 3.21B). In the medial zone, the

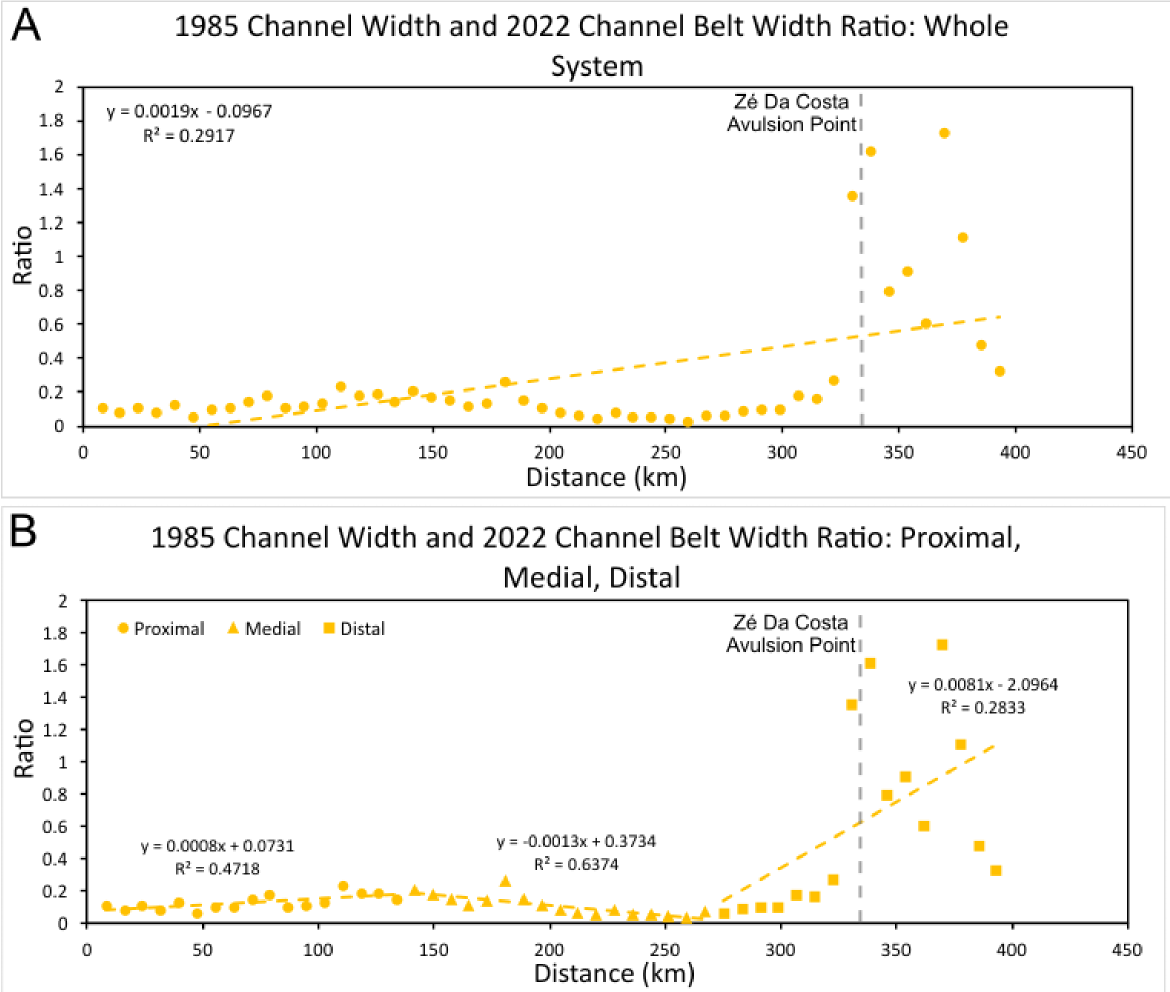

Figure 3.21. Ratio between 1985 channel width and 2022 channel belt width across the whole system (A) and in proximal, medial, and distal DFS zones (B).

ratio ranges from 0.03 to 0.26, with a median of 0.09, a mean of 0.11, and a standard deviation of 0.06 (Table 3.11). The ratio also remains low but shows a steady decrease downstream as demonstrated by a linear trendline with a strong negative correlation (R^2 = -0.64) (Figure 3.21B). In the distal zone, the ratio ranges from 0.07 to 1.73, with a median of 0.40, a mean of 0.62, and a standard deviation of 0.55 (Table 3.11). As outlined above, the 1985 channel becomes larger in width than the 2022 channel belt downstream of the Zé da Costa avulsion point. As such, there is an increase in ratio downstream in the distal zone demonstrated by a linear trendline with a weak positive correlation (R^2 = 0.28) (Figure 3.21B).

3.6.2 Statistics

3.6.2.1 2022 Channel Width and 1985 Channel Width

2022 channel width and 1985 channel width are compared to understand the change in channel width on the Taquari DFS since initiation of the Caronal avulsion (1996 to 1997). As outlined in methods section 2.2, the 1985 channel represents a channel which existed before the initiation of the avulsion whereas the 2022 channel represents a channel which is currently experiencing the avulsion and, as a result, a decrease in discharge downstream as flow is diverted to the avulsion channel. A Mann-Whitney test was carried out with a null hypothesis that there is no significant difference in width between both channels. The p-value is < 0.01 therefore the difference between the medians of each dataset is statistically significant and the null hypothesis can be rejected. 2022 channel width and 1985 channel width were then compared between proximal, medial and distal DFS zones, and in DFS reaches upstream and downstream of the Caronal avulsion point. The p-value is < 0.01 for each DFS reach compared, indicating that the widths of both channels are statistically different and there has been a clear change in channel width following the

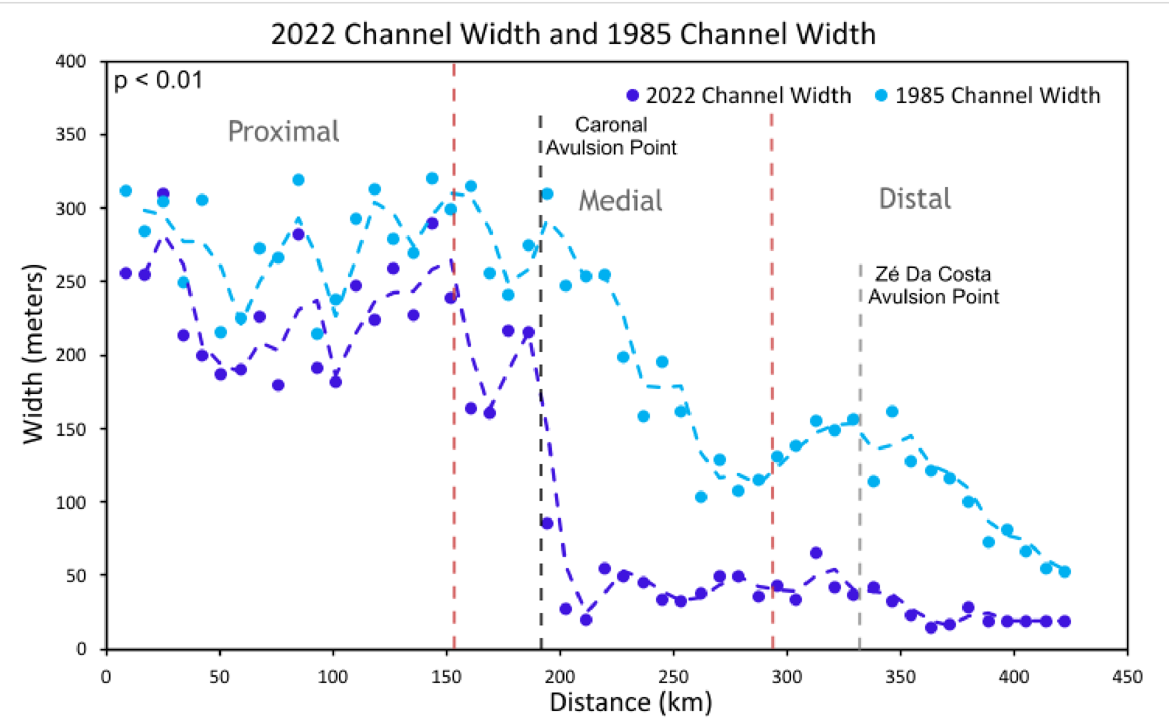

Figure 3.22. Comparison between 2022 channel width and 1985 channel width across the whole system with the p-value. Red dashed-lines delineate proximal, medial, and distal DFS zones. The location of the Caronal avulsion point and the Zé da Costa avulsion point are also marked by grey dashed-lines.

avulsion (Figure 3.22; Table 3.11). This result indicates that there has been a significant change in channel width on the Taquari DFS between 1985 and 2022.

3.6.2.2 2022 Sinuosity and 1985 Sinuosity

2022 channel sinuosity and 1985 channel sinuosity were compared using a Mann-Whitney test with a null hypothesis stating that the two datasets belong to the same population. The p-value is 0.08 which is greater than the 5% confidence interval (> 0.05), therefore it can be concluded that the two datasets have no statistically significant differences, and the null hypothesis cannot be rejected. This indicates that between 1985 and 2022 no significant changes in channel sinuosity have occurred (Figure 3.23; Table 3.11).

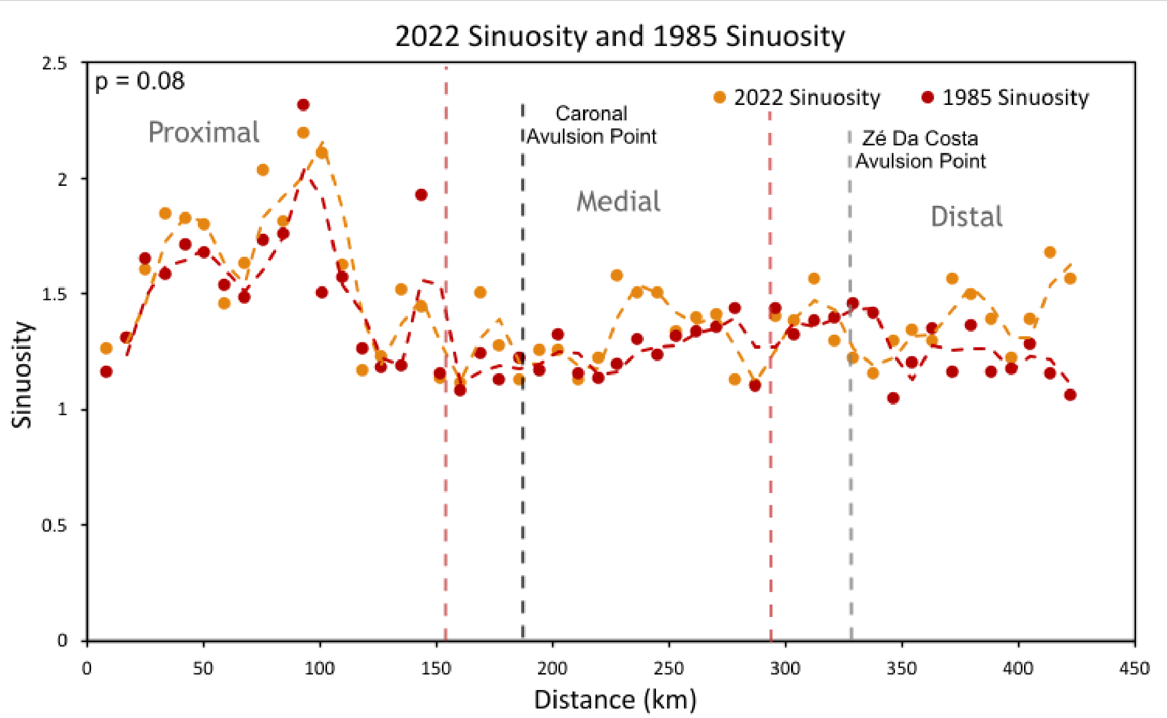

Figure 3.23. Comparison between 2022 channel sinuosity and 1985 channel sinuosity across the whole system with the p-value. Red dashed-lines delineate proximal, medial, and distal DFS zones. The location of the Caronal avulsion point and the Zé da Costa avulsion point are also marked by grey dashed-lines.

3.6.2.3 1985 Channel Width and 2022 Channel Belt Width

As previously outlined, 1985 channel width and 2022 channel belt width were compared to understand whether a relationship exists between two variables which have not been influenced by the Caronal avulsion. A Mann-Whitney test was carried out with a null hypothesis that there is no significant difference in width between the 1985 channel and the 2022 channel belt. The p-value is < 0.01 therefore the relationship between these variables is statistically significant and the null hypothesis can be rejected. 1985 channel width and 2022 channel belt width were then compared between proximal, medial and distal DFS zones. In the proximal and medial DFS zones the p-value is < 0.01, indicating a statistically significant relationship as 1985 channel width decreases downstream along with 2022 channel belt width. However, in the distal zone, the p-value is 0.17 as the 1985 channel width becomes larger than the 2022 channel belt width, as previously outlined. There is no statistically significant relationship in the distal zone as the 1985 channel cannot be compared to the 2022 channel belt in this locality (Figure 3.24; Table 3.11).

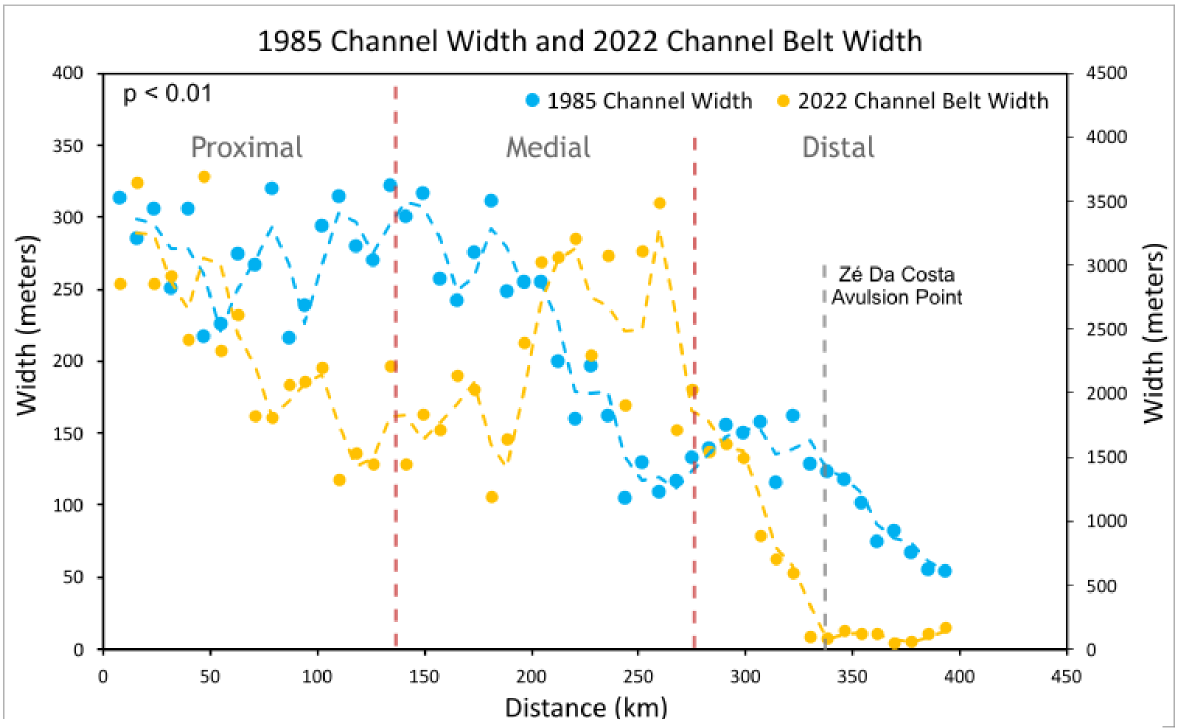

Figure 3.24. Comparison between 1985 channel width and 2022 channel belt width across the whole system with the p-value. Red dashed-lines delineate proximal, medial, and distal DFS zones. The location of the Caronal avulsion point and the Zé da Costa avulsion point are also marked by grey dashed-lines.

3.6.3 Summary of the Comparison Between the 1985 Taquari DFS and 2022 Taquari DFS: Ratios and Statistics

The ratio between 2022 channel width and 1985 channel width decreases steadily downstream across the whole system (R^2 = -0.65; Figure 3.19A, Table 3.11) with no correlation in ratio in proximal and distal zones (R^2 < 0.01 for each DFS zone (Figure 3.19B, Table 3.11)). The medial zone has a slight decrease in ratio downstream (R^2 = -0.28). The ratio is lowest in the medial zone (0.08; Table 3.11), followed closely by the distal zone (0.12). The highest ratio is in the proximal zone (1.01) where the 2022 channel width is slightly larger than the 1985 channel width. Upstream of the Caronal avulsion point, there is a slight decrease in ratio downstream (R^2 = -0.20; Figure 3.19C, Table 3.11) and downstream of the avulsion point there is no correlation in data (R^2 = 0.04). There is a statistically significant relationship between 2022 channel width and 1985 channel width across the whole system, including each DFS zone, and upstream and downstream reaches of the Caronal avulsion point ($p < 0.01$; Figure 3.22; Table 3.11).

Table 3.11. Ratios and statistics data for the 2022 DFS and 1985 DFS comparison where 2022 channel width is compared to 1985 channel width; 2022 sinuosity is compared to 1985 sinuosity; and 1985 channel width is compared to 2022 channel belt width. Variables are compared across the whole system, in proximal, medial, and distal DFS zones, and upstream and downstream reaches of the Caronal avulsion point.

	Max	Min	Median	Mean	SD	R^2	Mann-Whitney
2022 Channel Width/ 1985 Channel Width Ratio	1.01	0.08	0.38	0.51	0.29	-0.6538	p < 0.01
Proximal Ratio	1.01	0.66	0.85	0.84	0.09	0.0019	p < 0.01
Medial Ratio	0.90	0.08	0.31	0.40	0.24	-0.2755	p < 0.01
Distal Ratio	0.42	0.12	0.28	0.27	0.08	0.0017	p < 0.01
Ratio Upstream of Avulsion Point	1.01	0.28	0.84	0.79	0.15	-0.2019	p < 0.01
Ratio Downstream of Avulsion Point	0.46	0.08	0.27	0.27	0.09	0.0423	p < 0.01
2022 Sinuosity/ 1985 Sinuosity Ratio	1.48	0.75	1.05	1.07	0.16	0.0327	p = 0.08
Proximal Ratio	1.40	0.75	1.04	1.06	0.14	0.0051	p = 0.47
Medial Ratio	1.32	0.78	1.04	1.05	0.12	0.0210	p = 0.39
Distal Ratio	1.48	0.81	1.09	1.11	0.19	-0.3956	p = 0.07
Ratio Upstream of Avulsion Point	1.40	0.75	1.04	1.06	0.13	0.0016	p = 0.42
Ratio Downstream of Avulsion Point	1.48	0.78	1.05	1.09	0.17	0.0854	p = 0.04
1985 Channel Width/ 2022 Channel Belt Width Ratio	1.73	0.03	0.13	0.28	0.39	0.2917	p < 0.01
Proximal Ratio	0.24	0.06	0.11	0.13	0.04	0.4718	p < 0.01
Medial Ratio	0.26	0.03	0.09	0.11	0.06	-0.6374	p < 0.01
Distal Ratio	1.73	0.07	0.40	0.62	0.55	0.2833	p = 0.11

The ratio between 2022 sinuosity and 1985 sinuosity shows no correlation downstream (R^2 = 0.03; Figure 3.20A, Table 3.11) and in proximal and medial DFS zones (R^2 < 0.01 and 0.03, respectively (Figure 3.20B, Table 3.11). In the distal zone there is a general increase in ratio (R^2 = 0.40) as the 2022 channel becomes more sinuous than the 1985 channel downstream. Although the ratio is lowest in the proximal zone (0.75; Table 3.11), these channels still have a very similar sinuosity. The ratio is highest in the distal zone (1.48) where the 2022 channel is much more sinuous than the 1985 channel. In both upstream and downstream reaches of the Caronal avulsion point, the ratio between 2022 sinuosity and 1985 sinuosity shows no correlation ($R^2 < 0.01$ and 0.09, respectively (Figure 3.20C, Table 3.11). There is no statistically significant relationship present across the whole system ($p = 0.08$; Figure 3.23, Table 3.11), in proximal, medial, and distal DFS zones ($p = 0.47$, 0.39, and 0.07, respectively), or upstream of the Caronal avulsion point ($p = 0.42$). However, downstream of the avulsion point, there is a slightly more statistically significant relationship ($p = 0.04$) as this is where there is the largest difference observed between sinuosity values.

The ratio between 1985 channel width and 2022 channel belt width is slightly positively skewed and shows a slight increase downstream ($R^2 = 0.29$; Figure 3.21A, Table 3.11). In the proximal zone, the ratio remains low but shows a general increase downstream ($R^2 = 0.47$; Figure 3.21B, Table 3.11). In the medial zone the ratio also remains low but steadily decreases downstream ($R^2 = -0.64$). In the distal zone, where a slight positive skew in data exists as the 1985 channel width becomes larger than the 2022 channel belt width downstream of the Zé da Costa avulsion point, there is a weak increase in ratio downstream ($R^2 = 0.28$). The ratio is lowest in the medial zone (0.03; Table 3.11) and highest in the distal zone (1.73) where the 1985 channel width is significantly larger than the 2022 channel belt width. A statistically significant relationship is present between 1985 channel width and 2022 channel belt across the whole system, and in proximal and medial DFS zones ($p < 0.01$; Figure 3.24, Table 3.11). However, in the distal zone there is no statistically significant relationship ($p = 0.11$) as these variables cannot be compared downstream of the Zé da Costa avulsion point.

3.7 Additional Statistical Analyses

Additional statistical tests were carried out between variables which were hypothesised to have significant relationships such as 2022 channel sinuosity and active channel belt width; 1985 channel sinuosity and channel belt width; 2022 sinuosity and active meander deposit area; and 1985 sinuosity and abandoned meander deposit area. Due to the difference in dataset size between certain variables (i.e., larger dataset for meander deposit dimensions than channel width), each variable could not be compared to each other to create an overall p-value heatmap showing every relationship between variables. Therefore, these four comparisons were done instead.

3.7.1 Sinuosity and Channel Belt Width

Sinuosity was compared to channel belt width to understand whether a relationship existed between the sinuosity of the channel and the channel belt width. 2022 channel sinuosity was firstly compared to 2022 active channel belt width then 1985 channel sinuosity was compared to 2022 channel belt width. A Mann-Whitney test was carried out for each comparison with a null hypothesis that there is no relationship between variables. For 2022 channel sinuosity and 2022 active channel belt width, the p-value < 0.01 (Table 3.12) therefore the relationship is statistically significant, and the null hypothesis can be rejected. For 1985 channel sinuosity and 2022 channel belt width, the p-value < 0.01 (Table 3.12) therefore the relationship is statistically significant, and the null hypothesis can be rejected. These results indicate that where sinuosity is higher, channel belt width is also larger.

3.7.2 Sinuosity and Meander Deposit Area

Sinuosity was compared to active and abandoned meander deposit area to understand whether a relationship existed between the size of meander deposits and the sinuosity of the channel. 2022 channel sinuosity was firstly compared to active meander deposit area then 1985 channel sinuosity was compared to abandoned meander deposit area. A Mann-Whitney test was carried out with a null hypothesis that there is no relationship between these variables. For both tests carried out, the p-value < 0.01 (Table 3.12) therefore the relationship is statistically significant, and the null hypothesis can be rejected. This result shows that in areas of higher sinuosity, both active and abandoned meander deposits are larger in size (area).

3.7.3 Summary of Additional Statistical Analyses

Several statistically significant relationships were identified through additional statistical analyses of data collected on the 1985 and 2022 DFSs. Firstly, a statistically significant relationship was identified between 2022 channel sinuosity and 2022 active channel belt width and between 1985 channel sinuosity and 2022 channel belt width. These relationships show that the channel belt width is larger where the sinuosity of the channel is higher. Secondly, a statistically significant relationship was identified between 2022 channel sinuosity and active meander deposit area and between 1985 channel sinuosity and abandoned meander deposit area. These relationships show that where the sinuosity of the channel is higher, larger active and abandoned meander deposits are present.

Table 3.12. Mann-Whitney data for the comparison of: 2022 Sinuosity and Active Channel Belt Width, 1985 Sinuosity and Channel Belt Width, 2022 Sinuosity and Active Meander Deposit Area, and 1985 Sinuosity and Abandoned Meander Deposit Area.

	2022 Sinuosity / Active Channel Belt Width	1985 Sinuosity / Channel Belt Width	2022 Sinuosity / Active Meander Deposit Area	1985 Sinuosity / Abandoned Meander Deposit Area
Mann-Whitney	$p < 0.01$	$p < 0.01$	$p < 0.01$	$p < 0.01$

4 Discussion

This chapter will discuss the causes and implications of the results recorded in the previous chapter. Initially, the system scale trends associated with the river channel for the 1985 and 2022 systems will be outlined to understand general trends across the whole system. Then for the 2022 system, the changes in fluvial character upstream and downstream of the Caronal avulsion are discussed. Following this, there will be a particular focus on the spatial variability in fluvial characteristics within the modern Taquari DFS (2022) to understand relationships between variables in each DFS zone (proximal, medial, and distal). Thereafter, the temporal change in meander characteristics on the Taquari DFS between 1985 (pre-Caronal avulsion) and 2022 (during Caronal avulsion) are explored to understand the impact of the Caronal avulsion on the DFS. Finally, the implications of these results are considered.

All variables measured using the 1985 imagery are representative of the pre-avulsion system, however, some variables measured on the 2022 system are also interpreted to be representative of the pre-avulsion system (Table 4.1). These include channel belt width, hereafter referred to as pre-avulsion channel belt width, and abandoned meander deposit dimensions. Table 4.1 summarises each variable measured across 1985 and 2022 imagery outlining whether each variable is representative of the active or pre-avulsion system. As previously outlined in the methods section, 2.3, two separate channel belts were identified in satellite imagery: one representing the migration of the active channel (active channel belt); and the other representing the migration of the pre-avulsion channel (pre-avulsion channel belt). The differentiation between these two channel belts was aided by the presence of active and abandoned meander deposits found within each channel belt, respectively. Interpretations and characteristics of the active and pre-avulsion systems are outlined further below.

4.1 Interpretation of Results: System Scale

Distributive Fluvial Systems (DFS) are understood to distribute material in a radial manner due to their unconfined nature and frequent avulsion processes that occur on the DFS surface (Bull, 1968; Nichols and Fisher, 2007; Hartley et al., 2010). Common DFS characteristics associated with this radial dispersion of flow include downstream channel bifurcations; a reduction in channel size; channel presence; grain size; and discharge downstream (as a result of infiltration, evaporation, and bifurcation of channels) (Weissmann et al., 2010; Davidson et al., 2013; Weissmann et al., 2015; Owen et al., 2015; Martin et al., 2021); and an increase in floodplain presence (Weissmann et al., 2010; Hartley et al., 2010). The DFS trends observed in the pre-avulsion and active systems are outlined below.

Table 4.1. Summary table of each variable measured across 1985 and 2022 satellite imagery including: a brief summary of how the data was collected, the general downstream trends (or overall gradient), and whether the variable represents the active or pre-avulsion system.

Variable	Year of Satellite Imagery Used for Measurements	Brief Description of Variable	Overall R^2 Value or Gradient	Representative of Active or Pre-avulsion System
Elevation and Slope Gradient	2022	Elevation and slope gradient data extracted from a DTM from 2022 using the 2022 channel centreline	Gradient = -0.00025 m/m	Active
2022 Channel Sinuosity	2022	Extracted centreline from the 2022 active channel polygon	R^2 = -0.12	Active
1985 Channel Sinuosity	1985	Extracted centreline from the 1985 active channel polygon	R^2 = -0.22	Pre-avulsion
2022 Channel Width	2022	Mapped polygon of the active channel in 2022	R^2 = -0.76	Active
1985 Channel Width	1985	Mapped polygon of the active channel in 1985 (pre-Caronal avulsio)	R^2 = -0.77	Pre-avulsion
Active Channel Belt Width	2022	Mapped polygon representing the channel belt of the active channel	R^2 = -0.76	Active
Channel Belt Width (Pre-avulsion Channel Belt Width)	2022	Mapped polygon representing the channel belt of the pre-avulsion channel	R^2 = -0.48	Pre-avulsion
Active Meander Deposit Area	2022	Mapped polygons or meander deposits formed by the active channel	R^2 = -0.5	Active
Abandoned Meander Deposit Area	2022	Mapped polygons of meander deposits formed by the pre-avulsion channel and deposits which are unattached to the active channel upstream of the Caronal avulsion point	R^2 = -0.13	Pre-avulsion

4.1.1 1985 DFS (Pre-avulsion)

In the 1985 system, only active channel width (mapped using Landsat5 imagery from 1985) and sinuosity (extracted centreline from the 1985 channel polygon) are measured due to the limited resolution of the Landsat5 imagery. The 1985 active channel shows recognisable DFS characteristics downstream, such as a steady decrease in channel width (R^2 = -0.76; Figure 3.2A, Table 3.1). Channel width is expected to decrease downstream within a DFS as the flow disperses across a sedimentary basin due to bifurcation of the channel occurring downstream and avulsion (Weissmann et al., 2010; Davidson et al., 2013; Weissmann et al., 2015; Owen et al., 2015; Martin et al., 2021). There are weak trends in sinuosity across the 1985 channel with only a slight decrease in sinuosity downstream (R^2 = -0.22; Figure 3.3A, Table 3.2). This variability in sinuosity was found to be common in sinuous DFS, as noted by Davidson et al. (2013) and highlighted further below.

Schumm (1963) identified that a degree of variability in the sinuosity of a channel can exist in any channel experiencing meander cut-offs (Figure 2.6) or the development of new bends along the river. Davidson et al. (2013) identified that within a DFS, sinuosity can become more variable downstream due to an increase in channel bifurcations or when various anabranches develop along a channel. Sinuosity is understood to be higher where sediment load increases (i.e., due to the increased migration of point bars (Ahmed et al., 2019)). This relationship will be explored further in regards to DFS zone trends in section 4.2.1. It is also understood that meandering rivers (i.e., sinuous rivers) develop on lower gradient slopes, than braided systems, for example (Leopold and Wolman, 1957; Hartley et al., 2010), which will also be discussed further in section 4.2.1.

4.1.2 2022 DFS (Active)

The modern Taquari DFS is experiencing a large avulsion ~100 km down-DFS from the apex known as the Caronal avulsion (initiation between August 1996 to March 1997 (Assine, 2005; Buehler et al., 2011)). The parent channel of the avulsion (2022 active channel) is experiencing a significant decrease in discharge as flow is almost entirely diverted to the newly avulsed channel. This significant reduction in discharge and sediment supply downstream of the avulsion point has significantly influenced the dimensions of the active system variables on the Taquari DFS such as active channel width, active channel belt width, and active meander deposit dimensions, as will be detailed further below. Although variables such as pre-avulsion channel belt width, abandoned meander deposit dimensions, and sinuosity are not influenced by the Caronal avulsion, these features are all present within the 2022 system (as seen in satellite imagery from 2022) and give insights into the influences on meander characteristics downstream (Table 4.1).

4.1.2.1 2022 DFS: Gradient

In the 2022 system, the channel elevation decreases steadily downstream with a low gradient of -0.00025 m/m (Figure 3.4, Table 3.3) which is typical for a large DFS such as the Taquari. Hartley et al. (2010) identified a relationship between the length of the DFS and the gradient, for example, a DFS with a length > 100 km typically has a gradient < 0.005 m/m with larger DFS typically having much lower gradients. The Taquari DFS has an apex to toe length of ~250 km, which is considered to be a large DFS (megafan), thus the very low overall gradient of -0.00025 m/m can be explained by this relationship. Assine (2005) found a very similar decrease in elevation along the DFS from apex to toe (190 m to 85 m) to that found in this study (~187 m to 85 m). However, a slightly steeper gradient was observed by both Assine and Porsani et al. (2005) (-0.00036 m/m) than in this study (-0.00025 m/m). It is not understood whether this represents a change in gradient along the active channel as it is unclear where Assine and Porsani (2005) have measured this gradient from, or if it is due to data source differences.

In addition, this study observed a change in gradient on the DFS between the zone upstream of the Caronal avulsion point (-0.00028 m/m; Table 3.3) and downstream of the avulsion point (-0.00022 m/m). Upstream of the avulsion point, the active channel is incised into the DFS surface causing confinement of the active channel belt; this incision is interpreted to be the result of a drop in base level (Assine 2005; Buehler et al., 2011). The Caronal avulsion point marks the boundary between the confined portion of the DFS (upstream) and the unconfined portion of the DFS (downstream) (Figure 1.7). The point at which there is a change from the confined to unconfined setting on the Taquari DFS is referred to as the 'intersection point' (Assine, 2005; Porsani, 2005; Weissmann et al., 2010; and Buehler et al., 2011). Upstream of the intersection point, in the confined DFS reach, deposition on the DFS is limited by the confined active channel belt. Downstream of the intersection point, where flow is unconfined, channel migration is no longer restricted and frequent avulsion processes are able to build DFS stratigraphy (Assine, 2005; Buehler et al., 2011). Where the channel is confined, it has a steeper gradient as the river tries to reach its new equilibrium profile through incision into the DFS surface. However, where the channel becomes unconfined, avulsion processes are able to spread the sediment load further across the DFS surface therefore showing a slightly lower gradient downstream of the avulsion point.

4.1.2.2 2022 DFS: Active Channel Width

The 2022 active channel width decreases downstream (R^2 = -0.76; Figure 3.5A, Table 3.4) as is hypothesised to occur on a DFS (e.g., Weissmann et al. 2010). However, there is a significant decrease in the 2022 channel width downstream of the Caronal avulsion point as a result of the diversion of flow from the parent channel to the new Caronal avulsion channel (Figure 2.1). It is surprising that the 2022 channel has the same R^2 value as the 1985 channel (R^2 = -0.76; Figure 3.2, Table 3.1) considering the significant decrease in width experienced in the 2022 channel. However, this further highlights how a DFS can still experience a decrease in channel width downstream as a result of different conditions (i.e., while experiencing an avulsion). It is also important to note that meandering rivers can experience variability in width due to different localised factors (i.e., erosion and deposition of channel banks with different cohesive properties) (Hooke, 2023). For example, a channel bank may be stabilised due to vegetation and by consequence may experience less erosion than a less cohesive bank that is more vulnerable to erosion processes. It is therefore more likely to experience a change in channel width due to this (Hooke, 2023).

Buehler et al. (2011) studied the evolution of the Caronal avulsion on the Taquari DFS using satellite imagery and observed a clear decrease in channel width in the parent channel as discharge and sediment was diverted from the parent channel to the newly avulsed channel. Buehler et al. (2011) observed that the average width of the parent channel downstream of the avulsion point decreased from 168 m in 1988 (pre-avulsion) to 88 m in 2008 (around 11 years after the initiation of the Caronal avulsion). This study recognises a further decrease in the mean width of the parent channel (active channel) downstream of the avulsion point to ~34 m in 2022 (around 25 years after the initiation of the avulsion) (Table 3.4). If flow continues to be diverted to the new avulsion channel then channel width will continue to decrease downstream in the parent channel. This may have further implications on the active channel belt width and meander deposit dimensions, as will be explored further in this chapter.

Despite the clear overall decrease in active channel width downstream, when the active channel is split upstream and downstream of the Caronal avulsion point there is a much weaker correlation in channel width in both upstream and downstream reaches of the channel. Upstream of the Caronal avulsion point, active channel width has a degree of variability (SD = 47.94 m; Table 3.4) and shows a very slight decrease in width downstream (R^2 = -0.14; Figure 3.5C, Table 3.4). Channel width would be expected to decrease downstream on a DFS as a result of infiltration, evaporation and channel bifurcations which distribute flow and sediment across a DFS. However, due to the confinement of the channel belt upstream of the avulsion point, bifurcation and sediment distribution processes cannot occur the same way they do when unconfined. This results in the retention of high volumes of discharge and sediment within the channel belt and may contribute to the variability in channel width as channel morphology changes frequently as a result of the constant sediment load.

Where the channel becomes unconfined downstream of the avulsion point, a much steadier decrease in channel width would be expected as typical DFS distribution patterns resume, however, there is still only a general decrease in active channel width downstream with some variability (R^2 = -0.30; Figure 3.5C, Table 3.4). This suggests that there are further fluctuations in channel width downstream, however, the low standard deviation (13.18 m; Table 3.4) suggests that the width of the active channel does not vary widely. It is unknown why there is no clear decrease in channel width downstream of the avulsion point, however, trends in channel width will be explored further in section 4.2.1.2 where active channel width is observed for each DFS zone.

4.1.2.3 2022 DFS: Active Channel Belt Width

A decrease in 2022 active channel belt width is observed (R^2 = -0.77; Figure 3.6A, Table 3.5) with a similar significant decrease in width downstream of the Caronal avulsion point to the 2022 active channel. It is clear that the avulsion has diverted flow from the active channel resulting in a reduction in the channel size and power, therefore as the migration rate of the channel decreases, so too does active channel belt width. Observations of satellite imagery show that active meander deposits are created over a smaller area downstream within the active channel belt reflecting the decrease in discharge, sediment supply, and, in turn, stream power.

Despite the degree of variability in active channel width upstream of the avulsion point, active channel belt width generally decreases downstream in this reach of the DFS (R^2 = -0.54; Figure 3.6C, Table 3.5). Although channel belt width is expected to decrease on a DFS, this is understood to be associated with a decrease in channel width and therefore migration rate downstream which would reduce the size of the channel belt. Since this is not the case however, further analysis of satellite imagery was conducted to understand whether there was an additional control on active channel belt width.

It was observed on satellite imagery that the sinuosity of the active channel decreases slightly towards the Caronal avulsion point resulting in a straighter section of channel in this location. This was backed using the data collected in this study which shows a decrease in sinuosity downstream towards the avulsion point. This slight decrease in sinuosity then results in a decrease in the migration of the channel and smaller channel belt downstream.

In addition, the agricultural activity which is primarily restricted to the terraces above the confined active channel belt, often cultivates land very close to the active channel. This results in some parts of the mapped active channel belt polygon being straighter to reflect the boundary between the channel belt and the cultivated land (Figure 2.3B). Most of the confined active channel belt extent remains undisturbed by this agricultural activity, however, it is clear that in some portions of the active channel belt that the boundary between the confined channel belt and the terraces above the channel belt is hidden by farmland which overlaps with both areas (Figure 2.3B).

Despite the observed downstream trends in active channel belt width upstream of the Caronal avulsion point, downstream of the avulsion point there is a less obvious downstream decrease in active channel belt width (R^2 = -0.26; Figure 3.6C, Table 3.5). As outlined in 4.1.2.2, the active channel width remains fairly consistent downstream of the avulsion point without any obvious downstream trends. As there is no significant decrease in active width downstream then there is no clear decrease in the migration rate of the channel which is reflected in the active channel belt width.

4.1.2.4 2022 DFS: Pre-avulsion Channel Belt Width

From satellite imagery analysis, it is clear that a separate channel belt exists downstream of the Caronal avulsion point which is the product of a much bigger river with a much higher discharge and a greater migration rate (Figure 2.3). It is worth noting again (as initially outlined in methods section 2.3), that the active channel belt and pre-avulsion channel belt are the same width upstream of the Caronal avulsion point and downstream of the Zé da Costa avulsion point (Figure 2.3; Figure 3.18). The pre-avulsion channel belt was seen to be a misfit with regards to the modern active channel and active channel belt system downstream of the avulsion point, with little recent fluvial activity being observed. This prompted the interpretation of this channel belt as belonging to a channel that was present pre-avulsion. It is clear that the pre-avulsion channel belt has not been influenced by the change in discharge in the 2022 active channel as a result of the Caronal avulsion, this reveals that this is a clear product of a higher discharge river that existed on the DFS (pre-avulsion channel) previously.

A statistically significant relationship was found between pre-avulsion channel belt width and 1985 channel width (which is a pre-avulsion channel) as $p < 0.01$ (Figure 3.24; Table 3.11). This shows that where there is a decrease in 1985 channel width then the pre-avulsion channel belt width also decreases downstream. This would suggest that as the migration rate of the 1985 channel reduces, it creates a smaller pre-avulsion channel belt. The 1985 active channel is much larger than the 2022 active channel as it did not experience an avulsion, therefore it is a good example of a pre-avulsion channel which would have had the migration capacity to create a larger channel belt. It is worth noting however, that the pre-avulsion channel may have experienced changes in flow regime over long time periods (i.e., in response to larger climatic changes or hydrological events) which may have impacted the migration capacity of the pre-avulsion channel. For example, in the Powder River (USA), an extreme flood in 1923 reduced the migration rate of the channel in the two decades following the event (Schook et al., 2017; Hooke, 2023). Similarly, a 1978 flood in the Powder River reduced the peak annual flows by 48% and contributed to a reduction in channel width by 53% between the years of 1939 to 2013 (Schook et al., 2017; Hooke, 2023). This is why it is important to note that the 1985 channel shows fluvial characteristics from one point in time and that the pre-avulsion channel belt that is present in the 2022 system may have been created by many previous versions of the river (i.e., with different discharge).

Evidence of the frequent migration of this larger pre-avulsion channel is observed through the vast preservation of abandoned meander deposits within the pre-avulsion channel belt (Figure 2.4). Due to the frequent migration of the pre-avulsion channel over a larger unconfined area, preservation potential is increased thus showing the extent of the pre-avulsion channel belt. It is important to note that the preserved abandoned deposits within the pre-avulsion channel belt are the deposits of a system that could be influenced by much longer time scale controls (i.e., temporal changes in hydrological conditions as mentioned in the previous paragraph).

Although the pre-avulsion channel belt would be expected to decrease steadily downstream as pre-avulsion channel width and migration rate decrease downstream, there is only a general decrease in channel belt width observed downstream across the whole system (R^2 = -0.48; Figure 3.7A, Table 3.6). This may be the result of the change from the confined to unconfined portion of the DFS as there is a general decrease in pre-avulsion channel belt width upstream of the avulsion point then a very slight increase in pre-avulsion channel belt width downstream of the avulsion point before there is a further decrease in channel belt width downstream. The decrease in pre-avulsion channel belt width upstream of the avulsion point (where the pre-avulsion channel belt is the same width as the active channel belt) has been previously outlined in section 4.1.2.3. Downstream of the avulsion point, the pre-avulsion channel belt experiences a slight increase in width due to the channel becoming unconfined and free to migrate across the DFS surface. Then, downstream of this point, there is a clear decrease in pre-avulsion channel belt width (R^2 = -0.77; Figure 3.7C, Table 3.6) which is likely due to the decrease in discharge and migration rate of the pre-avulsion channel, in line with processes that operate on DFS. Downstream trends in pre-avulsion channel belt width are explored further in section 4.2.1.4 where the trends in each DFS zone are discussed.

4.1.2.5 2022 DFS: Sinuosity

Sinuosity shows very weak downstream trends in the 2022 channel, which is common in DFS (Davidson et al., 2013), as a very slight decrease in sinuosity is observed downstream (R^2 = -0.12; Figure 3.8, Table 3.7). The sinuosity of a channel can change frequently as meander cut-offs straighten sections of the river which then begin to re-meander over time, for example (Schumm, 1963; Hooke, 2023). However, the 2022 active channel experienced a significant decrease in discharge and sediment supply following the initiation of the Caronal avulsion, which reduces the migration capacity of the active channel. This should result in very little change in sinuosity over time as active migration is reduced. This is apparent when the overall sinuosity of the 1985 channel (1.55; Table 3.2) is compared to overall sinuosity of the 2022 channel (1.56; Table 3.7) and very little change in sinuosity is observed (Figure 3.23). This temporal change is explored further in section 4.3.2.

The sinuosity of the 2022 channel upstream of the Caronal avulsion point shows a slight downstream decrease in sinuosity (R^2 = -0.19; Figure 3.8, Table 3.7) which may reflect an increase in meander cutoffs towards the Caronal avulsion point where the channel is observed to be straighter in satellite imagery. Downstream of the avulsion point, sinuosity shows no correlation (R^2 = -0.08) which also reflects the typical lack of downstream trends in sinuosity observed where meander cutoffs occur and the channel re-meanders over time. Buehler et al. (2011) found that the sinuosity of the active channel in 2008 did not change following the Caronal avulsion, remaining 1.28 for the overall channel reach downstream of the avulsion point. Similarly, this study found that there has not been a large increase in sinuosity in the active channel in 2022 as the sinuosity increased to 1.39 (Table 3.7).

4.1.2.6 2022 DFS: Active Meander Deposit Dimensions

There is a general decrease in active meander deposit area (R^2 = -0.5; Figure 3.9; Table 3.8), deposit length (R^2 = -0.56; Figure 3.10; Table 3.8), and deposit width (R^2 = -0.57; Figure 3.11; Table 3.8) downstream in the 2022 system which this study hypothesised would occur due to the decrease in fluvial channel dimensions typical to a DFS. A significant decrease in active meander deposit dimensions is also observed in response to the decrease in discharge, and therefore sediment supply, downstream of the Caronal avulsion point. Davidson et al. (2013) observed a similar downstream decrease in active point bar dimensions on a sinuous DFS in Uzbekistan (Amudar'ya DFS), representing a decrease in lateral channel migration downstream. As the channel width decreased downstream, the point bar dimensions also decreased downstream (Davidson et al., 2013).

Ahmed et al. (2019) found that the growth of point bar deposits has a direct influence on channel sinuosity as an increase in sediment supply in a channel increases the growth rate of point bar deposits and therefore increases the sinuosity of a channel as point bars grow through channel migration. The relationship between changes in sinuosity and the size of active meander deposits downstream is explored further in section 4.2.1. This study found a statistically significant relationship between active meander deposit area and 2022 active channel sinuosity ($p < 0.01$; Table 3.12) showing that the sinuosity is directly influenced by the size of the meander deposit on the inside bend of the meander. This shows that as channel migration occurs (processes driven by erosion and deposition) that the resulting growth of deposits then increases the channel sinuosity.

There is a very clear decrease in active meander deposit dimensions between DFS reaches upstream and downstream of the Caronal avulsion point with significantly larger deposits observed upstream, as compared to downstream of the avulsion point (Figure 3.9, Table 3.8). Upstream of the avulsion point active meander deposits are largest, due to the high discharge and sediment supply downstream of the DFS apex. These deposits also show no correlation in deposit area, length, and width downstream (R^2 = 0.01, 0.04, and < 0.01, respectively (Figure 3.9; Figure 3.10; Figure 3.11; Table 3.8)) as deposits preserved within the confined active channel belt experience frequent reworking.

Downstream of the avulsion point however, there is a clear decrease in active meander deposit dimensions as discharge and sediment supply decrease downstream on the DFS (R^2 = -0.58 for area, -0.47 for length, and -0.61 for width (Figure 3.9; Figure 3.10; Figure 3.11; Table 3.8)). This clear decrease in dimensions downstream shows the impact of decreasing discharge downstream on a DFS as the flow has a lower sediment transport capacity downstream and therefore deposits smaller point bars. Upstream of the Caronal avulsion point mean area of the active meander deposits is 0.84 km^2 whereas downstream of the avulsion point mean area is 0.014 km^2 (Table 3.8). This is due to the decrease in sediment deposition downstream which results in a reduction in point bar growth.

4.1.2.7 2022 DFS: Abandoned Meander Deposit Dimensions

There is a clear difference between active meander deposits and abandoned meander deposits in the 2022 system, as the abandoned meander deposits have no significant downstream trends in area, length, or width. Abandoned meander deposit area and length have a slight downstream decrease in dimensions (R^2 = -0.13 and –0.21, respectively (Figure 3.12; Figure 3.13; Table 3.9)) and meander deposit width shows no correlation downstream (R^2 = 0.01; Figure 3.14; Table 3.9). Similar to the pre-avulsion channel belt, the abandoned meander deposits have not been influenced by the downstream decrease in discharge in the active channel as a result of the Caronal avulsion, as the abandoned deposits are unattached to the 2022 active channel. Therefore there is no significant decrease in abandoned meander deposit dimensions downstream of the avulsion point.

As the abandoned meander deposits do not represent a specific point in time like the active meander deposits do; they are representative of deposits which were formed before the initiation of the Caronal avulsion when the channel had a much higher discharge and sediment supply downstream. Larger abandoned meander deposits are seen to be preserved within the pre-avulsion channel belt as the larger pre-avulsion channel had the capacity to migrate further across the DFS surface and thus occupy the same area less frequently. This resulted in less reworking of deposits and an increase in preservation potential.

4.1.3 Summary of the 2022 DFS: System Scale

System scale trends within the 2022 Taquari DFS include:

- A decrease in elevation and slope gradient downstream similar to what would be expected on a DFS the size of the Taquari. A slight decrease in gradient is observed downstream of the Caronal avulsion point where the channel is no longer incised/ confined and is able to migrate further across the DFS surface and distribute sediment through increasingly frequent avulsion processes (Figure 3.4).

- A decrease in active channel width downstream, which is expected on a DFS, and a significant decrease in channel width downstream of the Caronal avulsion point as flow is diverted into the new avulsion channel (Figure 3.5).

- A decrease in active channel belt width as active channel width decreases, and a significant decrease in active channel belt width downstream of the Caronal avulsion point as the active channel loses discharge and migration capacity reduces (Figure 3.6).

- A general decrease in pre-avulsion channel belt width and a significant difference in size between the active channel belt and the pre-avulsion channel belt (Figure 3.7; Figure 3.18). The pre-avulsion channel belt was clearly formed by a much larger pre-avulsion channel with a much higher discharge and migration capacity and therefore is significantly larger in size than the active channel belt.

- A decrease in the dimensions of active meander deposits downstream, with a significant decrease in dimensions downstream of the Caronal avulsion point where the migration and deposition of the active channel is reduced (Figure 3.9). There is a clear difference between the active and abandoned meander deposit dimensions as they are associated with the active system (experiencing the avulsion) and the pre-avulsion system (where channel dimensions were much larger), respectively.

- A lack of overall downstream trends for the abandoned meander deposits as they are associated with the migration history of a pre-avulsion channel where discharge and sediment supply in the channel were much higher (Figure 3.12). This allowed for the deposition and increased preservation of abandoned meander deposits over a large area on the DFS surface. The lack of downstream trends also confirms that the abandoned meander deposits are not influenced by the Caronal avulsion, as they show no significant change in size downstream of the avulsion point and have clearly been deposited before the avulsion occurred.

- No correlation in the sinuosity of the 2022 active channel downstream, which is expected on a DFS as: meander cut-offs, channel bifurcations, and anabranches occur downstream (Figure 3.8). Sinuosity is higher in areas where larger active meander deposits are present, as channel migration controls the growth of meander deposits (which are larger where discharge and sediment supply is higher).

- A clear difference between DFS reaches upstream and downstream of the Caronal avulsion point as the largest dimensions in active variables (active channel width, active channel belt width, and active meander deposit dimensions) are found where discharge and sediment supply is highest on the system (upstream of the avulsion point).

- No correlation downstream in active channel width and active meander deposit dimensions upstream of the avulsion point due to the high discharge and sediment supply causing frequent channel migration and reworking of deposits (Figure 3.5C; Figure 3.9C).

- A general decrease in active channel belt width upstream of the avulsion point due to a slight decrease in sinuosity downstream which brings the active channel belt closer to the active channel (Figure 3.6C).

- A significant decrease in the dimensions of the active variables (active channel width, active channel belt width, and active meander deposit dimensions) downstream of the avulsion point, as discharge and sediment supply decrease significantly as a result of flow being almost entirely diverted to the newly avulsed channel.

- No influence from the Caronal avulsion point on the pre-avulsion variables (pre-avulsion channel belt width and abandoned meander deposit dimensions) downstream of the avulsion point (Figure 3.7; Figure 3.12). The dimensions of these variables are much larger than the active variables and are not influenced by the decrease in discharge and sediment supply downstream of the avulsion point.

- A clear downstream decrease in pre-avulsion channel belt width downstream of the avulsion point which may be associated with the decrease in migration capacity of the pre-avulsion channel.

- No influence of the Caronal avulsion on sinuosity, either upstream or downstream of the avulsion point.

4.2 Spatial Variability Patterns in Fluvial Characteristics in the Modern Taquari DFS

4.2.1 DFS Zone Trends

DFS have been previously quantified by splitting the DFS into recognisable zones (proximal, medial, and distal) (i.e., Hirst 1991, Weissmann et al., 2013; Davidson et al., 2013; Owen et al., 2015; and Martin et al., 2021). These studies provide a model/ framework for further DFS quantification (i.e., the modern DFS model). In this study, proximal, medial, and distal DFS zones are split into equal thirds to observe changes across each zone, as to date no other method is proposed to be used to define each zone on modern systems (Williams, 2023). When creating a DFS model it is important to consider that larger scale trends do not show the spatial variations that exist at smaller scales (i.e., between bends in a reach of a river (Hooke, 2023)). Due to the highly sensitive nature of meandering systems, quantifying changes in meander characteristics within each DFS zone enables greater understanding of trends that occur downstream across a DFS. It is important to note that these systems are highly sensitive to erosion and deposition processes, which are influenced by changes in discharge and sediment supply.

4.2.1.1 DFS Zone Trends: Gradient

Gradient decreases downstream in each DFS zone with the highest gradient in the proximal zone (-0.00027 m/m), decreasing in the medial zone (-0.00025 m/m), with the lowest gradient in the distal zone (-0.00018 m/m) (Table 3.3). This decrease in gradient on a sinuous DFS has been previously observed by Davidson et al. (2013) and Hartley et al. (2010) who identified that a low gradient sinuous river is typically associated with low sediment supply. It can therefore be assumed that as sediment supply and discharge decrease downstream so too does gradient.

The high gradient in the proximal zone of the Taquari DFS is likely associated with the high sediment supply typical to the proximal DFS zone, where high volumes of the coarsest grained sediment are deposited when the flow from the confined valley enters the sedimentary basin (Weissmann et al., 2013). Although flow is typically unconfined on the DFS surface, the active channel of the Taquari is incised for the first 100 km stretch downstream of the DFS apex (i.e., the proximal zone) until the Caronal avulsion point (Assine, 2005; Buehler et al., 2011). This results in an increase in gradient in the confined portion of the DFS as the channel adjusts to the change in base level (Assine, 2005).

In the medial zone, the DFS goes from confined to unconfined (Figure 3.1) as the modern depositional lobe exists downstream of the Caronal avulsion point. This change from confinement to unconfinement may result in a decrease in gradient downstream as sediment load in the active channel decreases significantly downstream of the Caronal avulsion point (i.e., where the DFS becomes unconfined), and sedimentation processes reduce.

In the distal zone, the gradient is lowest due to a further decrease in discharge and sediment supply downstream. Although the active channel did not display such a clear downstream decrease in channel width downstream of the avulsion point, it is clear that channel width is lowest in the distal zone, therefore it can be assumed that discharge and sediment load in the channel are also lowest in this zone. The low gradient in the distal zone may also be a result of avulsion processes (i.e., the Zé da Costa avulsion (1988 to 1999; Figure 1.7)), which can result in the wider distribution of sediment across the DFS surface and reduce sedimentation within the channel (Assine, 2005; Weissmann et al., 2013).

4.2.1.2 DFS Zone Trends: Active Channel Width (2022)

Active channel width shows no correlation in the proximal zone ($R^2 < 0.01$; Figure 3.5B, Table 3.4), then shows a more steady decrease in width in medial and distal zones ($R^2 = -0.61$ and -0.60, respectively (Figure 3.5B)). Active channel width also shows a very weak correlation upstream of the Caronal avulsion point (Figure 3.5B; Figure 3.5C). This is where the active channel belt is confined due to the incision of the active channel and thus prevents typical DFS bifurcation and sediment distribution processes, as outlined in section 4.1.2.2. As a result of this channel belt confinement, high volumes of sediment remain within the active channel belt and contribute to the frequent changes in channel morphology due to constant erosion and deposition within the channel.

Discharge and sediment load on a DFS is highest in the proximal zone as flow enters the sedimentary basin from the catchment area and deposits high volumes of the coarsest material at the site where the flow becomes unconfined (Weissmann et al., 2013). As the high sediment supply, importantly in conjunction with the lateral confinement of the channel on the Taquari DFS, prevents bifurcation and sediment distribution processes which would occur on a typical unconfined DFS, this reduces the likelihood of the proximal zone of the Taquari following conventional DFS models.

Despite the general consistency observed in active channel width downstream of the Caronal avulsion point (section 4.1.2.2), the medial and distal zones show a more steady decrease in width downstream in each zone. The channel reach downstream of the avulsion point is a better indicator of overall trends in channel width downstream, however, it is not known why there is not a more steady decrease in width downstream. To better understand this downstream consistency in channel width, more information would be required on local changes in erosion and deposition rates within the channel which influence the channel morphology (Lane et al., 1996).

In the medial zone, active channel width shows a steadier decrease in width downstream which would be typical to a DFS. However, as the Caronal avulsion occurs in the medial zone this may result in a slightly negatively skewed downstream trend as the channel width decreases significantly downstream of the avulsion point (Figure 3.5B). The avulsion has had a significant impact on active channel width as mean width reduces from 230.86 m in the proximal zone to 89.6 m in the medial zone (Table 3.4). As flow is diverted to the avulsion channel, the remaining discharge in the active channel decreases further downstream resulting in the very low mean channel width of 30.08 m in the distal zone (where the lowest width value is ~15 m).

As previously mentioned Buehler et al. (2011) also observed a significant decrease in the width of the parent channel (active channel) downstream of the Caronal avulsion point due to the partial diversion of flow to the newly avulsed channel. Various bifurcations also occur downstream along the active channel which further reduces discharge in the channel in medial and distal zones. The decrease in width observed in the distal zone is most similar to a typical DFS model as avulsions become more common (i.e., the Zé da Costa) and various bifurcations reduce the channel width further downstream.

4.2.1.3 DFS Zone Trends: Active Channel Belt Width

The active channel belt shows a general decrease in width downstream in the proximal, medial, and distal DFS zones (R^2 = -0.59, -0.50, -0.46, respectively (Figure 3.6C; Table 3.5)). As outlined in section 4.2.1.3, active channel belt width is expected to decrease downstream on a typical DFS as DFS bifurcation processes reduce the active channel width downstream, resulting in a decrease in migration capacity and therefore channel belt width. However, the active channel does not show clear downstream trends in width in the proximal zone (R^2 < 0.01, Figure 3.5B, Table 3.4), which would be associated with these typical DFS bifurcation processes. Although the decrease in active channel belt width cannot be explained by a decrease in active channel width, analysis of satellite imagery (initially outlined in section 4.1.2.3) revealed additional factors (i.e., a decrease in sinuosity in the active channel and agricultural activity on the terraces above the confined channel belt) which may have influenced the active channel belt extent.

The fluctuations in sinuosity in addition to the difficulty outlining the confined active channel belt, highlight variability in DFS characteristics which may need to be considered in a modern DFS model. The proximal zone does however show the largest active channel belt width across the whole DFS (despite the confinement), which is a recognisable characteristic of the proximal DFS zone (Weissmann et al., 2013). On a typical DFS, the proximal zone has the widest channel belt reflecting the high discharge and sediment supply entering the DFS from the catchment area where frequent avulsion processes create highly amalgamated sandy channel bodies (Weissmann et al., 2010; Hartley et al., 2010; Weissmann et al., 2013; Weissmann et al., 2015; Martin et al., 2021).

In medial and distal DFS zones active channel belt width continues to decrease in size downstream with a significant decrease in active channel belt width downstream from the proximal to medial, and distal zones (mean width = 2264.19 m, 580.56 m, 155.02 m, respectively (Figure 3.6B, Table 3.5)) showing the decrease in discharge and sediment supply downstream. As the medial zone includes the Caronal avulsion point (upstream of which, the active channel belt width is significantly larger than the width downstream of this point), then this may increase the mean width in this zone slightly as there is a negative skew in data. The part of the medial zone downstream of the avulsion point and the distal zone show the significant changes in active channel belt width once the discharge reduces in the active channel as a result of the avulsion. As flow is diverted to the new avulsion channel, the discharge in the channel is significantly reduced and therefore has a much smaller migration capacity. The reduction in size of the active channel belt width clearly shows the impact of the reduction in channel width and stream power as a result of a decrease in discharge and sediment supply.

Although there is a general decrease in active channel belt width in medial and distal zones, this differs from the DFS reach downstream of the Caronal avulsion point which shows a weaker negative correlation in active channel belt width (R^2

= -0.26; Figure 3.6C, Table 3.5) (as outlined in section 4.1.2.3). The DFS reach downstream of the avulsion point is a better indicator of the overall trends in the system, which likely shows weaker trends due to the weak negative correlation observed in active channel width downstream of the avulsion point. Despite the negative skew in data in the medial zone, the distal zone has no skew and displays a downstream decrease in active channel belt width which is most similar to typical DFS trends.

4.2.1.4 DFS Zone Trends: Pre-avulsion Channel Belt Width

As initially outlined in methods section 2.3, and subsequently in section 4.1.2.4, the pre-avulsion channel belt and the active channel belt have the same width upstream of the Caronal avulsion point, and downstream of the Zé da Costa avulsion point. These two channel belts were identified (and differentiated) within the 2022 satellite imagery, which showed that two distinct channel belts were present, representing the migration capacity of different channels (pre-avulsion channel and active channel). The migration of the active channel is revealed by the active channel belt; a significant change in active channel belt dimensions are seen downstream of the Caronal avulsion point, which is not observed for the pre-avulsion channel belt. The pre-avulsion channel belt reveals the migration history of the pre-avulsion channel, which had a much higher discharge prior to the initiation of the Caronal avulsion. As previously outlined (section 4.1.2.4), the active 2022 channel is a misfit in regards to the pre-avulsion channel belt downstream of the Caronal avulsion point and could not have created a channel belt of this size with such a low discharge (and therefore migration capacity).

In the proximal zone, pre-avulsion channel belt width has a general decrease in width downstream (R^2 = -0.59; Figure 3.7B, Table 3.6), in the medial zone there is a weaker correlation (R^2 = 0.14) with a very slight increase in width downstream, and in the distal zone there is steady decrease in width (R^2 = -0.73). In the proximal DFS zone, the pre-avulsion channel belt is the same width as the active channel belt therefore the interpretations for this zone are the same, which was outlined earlier in section 4.2.1.3 above.

The medial DFS zone contains part of the pre-avulsion channel belt, which is located upstream of the Caronal avulsion point (where it is the same width as the active channel belt) and downstream of the avulsion point (where it is much larger than the active channel belt). There is a very slight increase in pre-avulsion channel belt width in the medial zone which is unexpected on a DFS as channel belt width is expected to decrease downstream (Weissmann et al., 2013). However, this is due to the pre-avulsion river moving from confinement to unconfinement, thus mimicking what would typically be observed in a proximal zone where a river becomes unconfined downstream of the apex of the system. The Caronal avulsion point marks the intersection point between the confined portion of the DFS (upstream) and the unconfined portion (downstream) where the modern lobe of deposition exists (Assine, 2005; Porsani et al., 2005; Weissmann et al., 2010; Buehler et al., 2011). Where the pre-avulsion channel is able to migrate freely across the DFS surface in the medial zone, recognisable DFS trends are observed including evidence of avulsive behaviour (i.e., paleochannels observed in figure 1.1) and channel migration, as highlighted by the vast preservation of abandoned meander deposits within the pre-avulsion channel belt (Weissmann et al., 2013). Within a DFS, evidence of avulsion processes are often preserved within a channel belt and its floodplains (Sahoo et al., 2020; Martin et al., 2021).

In this study, the preservation of abandoned meander deposits in the medial zone of the pre-avulsion channel belt demonstrates how frequent avulsions and channel migration processes can form meander deposits over a wide area. These deposits become preserved on the DFS surface as channel migration continues or the river avulses to a new area on the DFS. Within the rock record, the medial zone of a DFS is identified through isolated channel deposits which are increasingly separated by floodplain deposits (i.e., finer grained overbank deposits) downstream (Weissmann et al., 2013; Martin et al., 2021). As the majority of the abandoned meander deposits are isolated within the channel belt (and therefore separated by floodplain deposits) then it can be assumed that this DFS zone would fit a typical DFS model.

In the distal zone, there is a much steadier decrease in pre-avulsion channel belt width downstream which is more typical of a DFS model where the channel belt width would decrease as channel width decreases (Weissmann et al., 2013).

However, this may be due to a negative skew in the data where the pre-avulsion channel belt width becomes the same size as the active channel belt width downstream of the Zé da Costa avulsion point and therefore experiences a further decrease in width. These channel belts are the same width downstream of the avulsion point as there was no evidence in satellite imagery which revealed a larger channel belt which showed the migration of the pre-avulsion channel. This is likely because the avulsion occurred and shifted the position of the channel on the DFS to its current location (i.e., 2022 active channel) and a new channel belt was created for the active channel. The channel belt that exists downstream of the Zé da Costa avulsion point (where the active channel belt and pre-avulsion channel belt are the same width), is very close in width to the active channel as it reflects the reduced migration capacity of the distal channel once the discharge reduced following the Caronal avulsion.

4.2.1.5 DFS Zone Trends: Sinuosity

As previously outlined in section 4.1.2.5, sinuosity shows no downstream trends across a DFS due to bifurcation processes and anabranches occurring downstream (Davidson et al., 2013). In addition, the frequency of meander cutoffs and re-meandering can change the sinuosity of a channel (Schumm, 1963) as well as the growth of point bar deposits which can also increase the sinuosity of a channel (Ahmed et al., 2019). In proximal, medial, and distal DFS zones, there is no correlation in sinuosity downstream in each zone ($R^2 < 0.01$, $= 0.03$, and 0.13, respectively (Figure 3.8B; Table 3.7)).

The proximal DFS zone has a higher variability in sinuosity in comparison to medial and distal zones (SD = 0.30, 0.16, and 0.14, respectively (Table 3.7)), which is likely associated with the large discharge and sediment supply in the proximal zone which increases the migration capacity of the channel. The proximal zone also has the highest sinuosity values across the whole DFS (overall sinuosity is 1.82 in the proximal zone, 1.31 in the medial zone and 1.49 in the distal zone (Table 3.7)), which is likely associated with the growth of large active meander deposits, which are largest in size in the proximal zone (Table 3.8).

Google Earth Timelapse Tool is used to visualise the growth of meanders over time in the proximal zone to understand how sinuosity increases with meander growth (Figure 4.1). Figure 4.1 shows the growth of three meander bends over time in the active channel; the sinuosity of the channel can be seen to increase between 1985 and 2021 as the meander deposits grow in size. Sinuosity and active meander deposit data can be found in tables 3.7 and 3.8, respectively.

Figure 4.1. The growth of three separate meander bends between 1985 and 2022 showing the increased distance between apex of each meander bend over time as the deposits migrate and increase the sinuosity of the channel. The white dashed lines show the direction of growth of each meander and the slight rotation of the top two meander bends between image A and B. There is very little change observed between images B and C despite the similar length in time between these images as between images A and B. Source of images: Google Earth (Timelapse Tool).

Although there is a higher migration capacity of the channel in the proximal zone, the active channel belt is still confined resulting in more frequent meander cutoffs (both chute and neck cutoffs) occurring as the channel cannot migrate freely across the DFS surface. As previously outlined, Ahmed et al. (2019) found that sinuosity in a channel can increase more rapidly where point bars are growing rapidly (i.e., where discharge and sediment supply are higher). Thus the confined portion of the system is still receiving high sediment loads but due to confinement is having to rapidly redistribute the sediment over a smaller area.

In medial and distal DFS zones, the sinuosity of the channel is much lower than in the proximal zone with the sinuosity in the distal zone being slightly higher than in the medial zone (mean sinuosity = 1.64 in the proximal zone, 1.29 in the medial zone, and 1.39 in the distal zone (Table 3.7)). It is clear from satellite imagery that many meander cutoffs have occurred over time in the medial and distal zones; this is also evidenced by the vast preservation of abandoned meander deposits.

In the distal zone, sinuosity increases slightly from the medial zone which may be the result of the further decreasing gradient of the DFS which is at its lowest in the distal zone (-0.00018 m/m; Table 3.3). Changes in slope, discharge, and sediment supply downstream can all influence sinuosity across a DFS, however slope in particular is a key influence on sinuosity as higher sinuosity channels are typically found on lower gradient slopes (Leopold and Wolman, 1957; Hartley et al., 2010). On the Taquari DFS, it can be assumed that as sedimentation decreases downstream (due to a reduction in discharge and sediment supply) and is lowest in the distal zone, then the gradient also decreases resulting in favourable conditions for the formation of a more sinuous channel (i.e., low slope conditions).

4.2.1.6 DFS Zone Trends: Active Meander Deposit Dimensions

This study hypothesises that a decrease in channel width, and therefore discharge and sediment supply, downstream would result in a decrease in meander deposit dimensions downstream on the Taquari DFS. It is clear that within each DFS zone, changes in deposit dimensions have occurred as a result of a decrease in discharge and sediment supply downstream of the Caronal avulsion point. In the proximal DFS zone, active meander deposit area, length, and width show no correlation downstream (R^2 = 0.07, < 0.01, 0.07, respectively (Figure 3.9B; Figure 3.10B; Figure 3.11B; Table 3.8)). The lack of correlation in active meander deposit dimensions is largely influenced by the high sediment supply in the proximal zone which results in frequent deposition and reworking of deposits. This is well understood on the DFS as large amalgamated sand deposits are a common characteristic of the proximal DFS zones (Weissmann et al., 2013; Owen et al., 2015; Hartley et al., 2018). This is due to the fact that high volumes of sediment are deposited where the river becomes unconfined at the apex of the DFS (Weissmann et al., 2010; Hartley et al., 2010; Weissmann et al., 2013; Weissmann et al., 2015; Martin et al., 2021). The confinement of the active channel belt in the proximal zone may increase the amount of reworking of meander deposits as the channel migrates over a smaller area more frequently. The largest meander deposit dimensions are also observed in the proximal zone due to this high sediment supply and the rapid deposition of material downstream of the apex of the DFS.

In the medial DFS zone, active meander deposit dimensions generally decrease downstream (R^2 = -0.46 for area, -0.44 for length and -0.64 for width (Figure 3.9B; Figure 3.10B; Figure 3.11B; Table 3.8)). The medial zone experiences a significant decrease in active channel width downstream of the Caronal avulsion point where discharge and sediment load decrease in the channel. This decrease in discharge and sediment load in the medial zone results in a clear reduction in meander deposit dimensions as sedimentation reduces, therefore showing the influence of changing channel width on meander dimensions. When considering the mean area of active meander deposits between proximal, medial, and distal zones, mean area in the proximal zone is 0.92 km^2 whereas in the medial zone and distal zones mean area decreases significantly to 0.16 km^2 and 0.00063 km^2, respectively (Table 3.8). The decrease in discharge and sediment supply in the active channel downstream of the avulsion point has a very clear influence on the size of meander dimensions due to the fact that the stream power decreases and loses the capacity to carry higher volumes of sediment downstream, which, in turn, form smaller deposits.

The distal zone also has a general decrease in meander dimensions downstream as R^2 = -0.50 for area, -0.37 for length, and -0.48 for width (Figure 3.9B; Figure 3.10B; Figure 3.11B; Table 3.8). Meander dimensions are smallest in the distal zone and clearly reflect the smaller volume of sediment carried to distal reaches of the DFS where discharge is at its lowest. The downstream decrease in active point bar (meander deposit) dimensions on a sinuous DFS was also noted by Davidson et al. (2013) who recognised a relationship between declining channel width and point bar size downstream.

Four examples of active meander deposit areas measured in ArcGIS are displayed in Figure 4.2; changes in active meander dimensions (Table 3.8) are visualised and reveal a relationship between deposit length and width. As deposits become smaller downstream on the DFS they are observed to wrap more tightly around the meander bend with less protrusion into the channel forming a more crescent shaped deposit (Figure 4.2D and E). This likely reflects the decrease in migration rate downstream as the point bar deposit is unable to grow further into the channel (through lateral migration processes) and instead the deposit is observed to grow longer in the downstream direction.

These observations in satellite imagery are backed using data collected in this study as they examine where meander deposit width (measured perpendicular to deposit migration direction) becomes larger than deposit length (measured parallel to deposit migration direction) downstream (Table 3.8). As active meander deposits decrease in size downstream, they change shape from a more

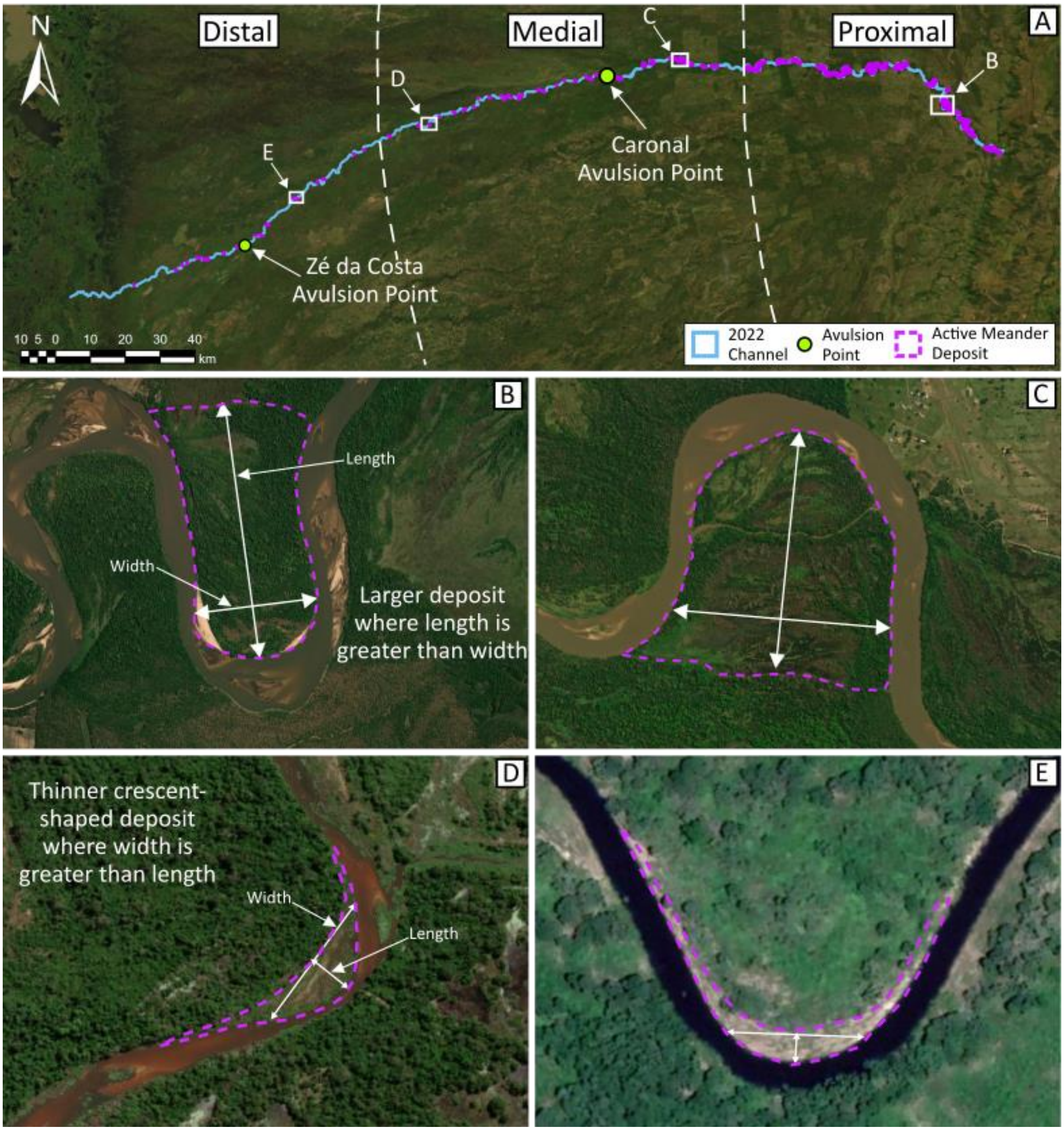

Figure 4.2. The change in active meander deposit shape downstream across the Taquari DFS (A) as discharge and sediment load decrease. Images B and C show a proximal meander deposit and a medial meander deposit (upstream of the Caronal avulsion point), respectively, where deposit length is greater than deposit width and the deposit shape is large and more rounded due to higher discharge and sediment supply upstream of the avulsion point. Images D and E show a medial and distal meander deposit, respectively, which are much thinner, crescent-shaped deposits which form more tightly round the meander bend as discharge and sediment supply decrease downstream.

rounded deposit (where deposit length and width are more similar) to a more crescent shaped deposit (where deposit width becomes larger than length downstream) (Figure 4.2). For active meander deposits in the proximal zone, where deposit length is greater than width, this is interpreted to reflect the higher migration rate of the channel as the deposit is able to increase in length due to lateral migration.

Davidson et al. (2013), however, observed a different relationship in a sinuous DFS where meander deposit length was larger than deposit width downstream and the ratio of deposit length to width decreased downstream. This may be a reflection of the higher migration rate downstream in the channel studied by Davidson et al. (2013), where the point bar deposit is able to migrate further through lateral migration. In this study, the significant decrease in discharge downstream of the Caronal avulsion point has a large influence on the migration capacity of the channel and prevents the rapid growth of point bars (active meander deposits).

4.2.1.7 DFS Zone Trends: Abandoned Meander Deposit Dimensions

There is a significant difference in downstream trends between active and abandoned meander deposit dimensions as the abandoned deposits have no significant downstream trends in deposit area, length, and width in any DFS zone. The proximal zone shows no correlation in abandoned meander deposit area, length, and width downstream (R^2 < 0.01, = 0.01, < 0.01, respectively (Figure 3.12B, Figure 3.13B, Figure 3.14B, Table 3.9)) similar to the lack of correlation observed in active meander deposit dimensions in the proximal zone. However, abandoned deposits show no downstream trends in medial and distal zones in comparison to the downstream trends observed for the active deposit dimensions in these DFS zones. Abandoned deposit area, length, and width show no correlation downstream in the medial zone (R^2 = 0.05, 0.02, 0.05, respectively) and in the distal zone (R^2 = 0.01, -0.16, < 0.01, respectively) highlighting that these deposits are not associated with a single period of deposition where general downstream trends would likely be observed. Instead, the abandoned meander deposits represent a long period of deposition where channel migration occurred over a wide area facilitating the preservation of deposits within the channel belt.

Abandoned meander deposits were interpreted to be the deposits of the pre-avulsion channel (as outlined in section 4.1.6.2) as they showed no significant change in dimensions downstream of the Caronal avulsion point. In addition, abandoned meander dimensions are significantly larger than the active deposit dimensions downstream of the avulsion point where it is clear that these are the deposits of a channel with a much higher discharge and sediment load (the pre-avulsion channel). The mean area of abandoned meander deposits in the proximal zone are much smaller than the mean area of the active deposits in the proximal zone (likely due to the frequent reworking of abandoned deposits due to channel belt confinement). It is worth noting that in medial and distal zones the abandoned deposit dimensions are often much larger than active deposit dimensions.

Abandoned meander deposit dimensions are largest in the proximal zone (mean area = 0.40 km^2 (Table 3.9)) where the discharge and sediment load is highest on a DFS. However, due to the confinement of the active channel belt it is likely that these deposits have experienced frequent reworking as the channel has a much smaller area to migrate over. The medial and distal DFS zones have a very similar mean area of abandoned meander deposits (0.24 km^2 and 0.25 km^2, respectively (Table 3.9)), with the distal zone having a slightly larger mean area. This further highlights the lack of downstream trends in abandoned meander deposit dimensions as there is no clear decrease in deposit dimensions downstream, which was a notable characteristic that was observed in the active meander deposit dimensions.

The slight difference in mean area between the medial and distal zones may reflect the increase in preservation potential downstream as the migrating channel has a greater area to migrate over in the distal zone. Where the channel has a greater area to migrate, deposits are reworked less frequently and are thus able to be preserved on the DFS surface. Additionally, the medial zone has been found to show the highest variability in terms of channel to floodplain ratio, as found in a study of the Huesca DFS, Spain by Martin et al. (2021). This variability may be explained by the preservation of abandoned meander deposits with a range in dimensions on the DFS surface alongside active meander deposits within the active channel belt. In this case, the preservation of deposits on a

DFS is dependent on the frequency of channel migration and the migration capacity.

4.2.2 Summary of DFS Trends in the 2022 Taquari DFS

The objectives of this study, initially set out in Chapter 1, section 1.2, were to firstly quantify spatial changes in active and abandoned variables on the 2022 Taquari DFS at system scale and DFS zone scale using satellite imagery. Secondly, to compare changes in channel width and sinuosity between 1985 and 2022 imagery to understand temporal changes which occurred following the Caronal avulsion. Thirdly, to compare active and abandoned variables on the 2022 DFS upstream and downstream of the Caronal avulsion point to explore the impact of the avulsion. Then finally, to create a database where active and abandoned meander deposit dimensions are quantified spatially across a DFS.

4.2.2.1 Proximal Zone

- The slope gradient is highest in the proximal zone (in comparison to medial and distal zones) as this reflects where the discharge and sediment supply is highest on the DFS as coarse grained sandy material is deposited rapidly downstream of the DFS apex. The confinement of the active channel belt also increases the gradient of the DFS in the proximal zone as the active channel adjusts to a drop in base level.

- The high sediment supply which is common in the proximal zone results in the largest dimensions for: active channel width, active channel belt width, active meander deposit dimensions, and abandoned meander deposit dimensions.

- The high sediment supply also results in a lack of downstream trends in active channel width, active meander dimensions, and abandoned meander dimensions due to frequent channel migration and reworking of deposits within the confined active channel belt.

- Sinuosity also shows a lack of downstream trends in the proximal zone, likely due to frequent meander cutoffs in the confined active channel belt, however sinuosity is also highly variable across the whole DFS.

- Active channel belt width is the only variable that shows a general downstream decrease in dimensions in the proximal zone which is assumed to be associated with a slight decrease in sinuosity towards the medial zone where the migration rate, and therefore active channel belt width, reduces.

4.2.2.2 Medial Zone

- In the medial zone, there is a further decrease in gradient downstream as the active channel goes from a confined to an unconfined setting at the Caronal avulsion point and sediment can be distributed across the DFS surface through migration processes.

- There is a significant decrease in: active channel width, active channel belt width, and active meander deposit dimensions downstream of the avulsion point as a result of the diversion of flow from the parent channel to the newly avulsed channel. This highlights the influence of discharge and sediment supply on meander deposit dimensions as there is a general decrease in dimensions downstream of the avulsion point as channel width reduces.

- The large difference in active and abandoned meander deposit dimensions is observed more clearly in the medial zone as abandoned meander deposits are significantly larger than active deposits downstream of the avulsion point.

- The abandoned deposits have no trends in dimensions downstream and are clearly the deposits of a larger pre-avulsion channel, which was able to migrate further across the DFS surface preserving deposits in the pre-avulsion channel belt.

- The pre-avulsion channel belt is also much larger than the active channel belt in the medial zone (downstream of the avulsion point) and does not show a decrease in channel belt width which would be expected on a DFS. This is due to the slight decrease in active/pre-avulsion channel belt width slightly upstream of the avulsion point then the growth of the pre-avulsion channel belt once it becomes unconfined.

- Sinuosity continues to be variable in the medial zone and has the lowest sinuosity value across the whole DFS which may be a reflection of previous meander cutoffs that did not re-meander.

4.2.2.3 Distal Zone

- The distal zone has the lowest gradient on the DFS and this is evidenced by the reduced sedimentation rate in these distal reaches and the increase in avulsions (i.e., the Zé da Costa) which distribute finer grained sediment further across the DFS surface.

- There is a further decrease in: active channel width, active channel belt width, active meander deposit dimensions as well as a decrease in the pre-avulsion channel belt width in the distal zone.

- Abandoned meander deposits continue to show no trends in dimensions downstream. Abandoned meander deposits are also better preserved in the distal zone than in the medial zone as the migrating channel has a greater area to migrate over and thus reworks deposits less frequently; this is highlighted by the slightly larger mean area of distal abandoned deposits.

- Sinuosity increases very slightly in the distal zone which may be due to the lower gradient slope as this is understood to develop a more sinuous planform.

4.3 Temporal Change in Fluvial Characteristics in the Taquari DFS Between 1985 and 2022

4.3.1 Changes in Channel Width

There has been a clear decrease in channel width in the main channel of the Taquari DFS between 1985 and 2022 as discharge in the channel continues to decrease as flow is diverted to the newly avulsed channel at the Caronal avulsion point. Satellite imagery from 1985 shows the active channel in full flow before the initiation of the Caronal avulsion (between 1996 and 1997); the 1985 channel is therefore referred to as a pre-avulsion channel. The 1985 channel is a stable channel that does not have any active avulsions, therefore it can be directly compared to the 2022 channel which experiences the avulsion to quantify changes in channel width over time. The 1985 channel shows typical DFS trends such as a decrease in channel width downstream (Figure 3.2A); comparing the 2022 channel to the 1985 channel shows the impact of the avulsion on the parent channel (2022 active channel) (Figure 3.22).

A statistically significant relationship was found between 2022 channel width and 1985 channel width ($p < 0.01$; Figure 3.22, Table 3.11) showing that there has been a significant decrease in channel width between 1985 and 2022. As the Caronal avulsion continues to divert flow to the avulsed channel, the width of the parent channel will continue to decrease. As initially outlined in section 4.1.2.2, a study on the Caronal avulsion by Buehler et al. (2011) found that the average width in the parent channel downstream of the Caronal avulsion point decreased around 80 m between 1988 to 2008 (from 168 m to 88 m). This study found that between 1985 and 2022 the mean width of the parent channel downstream of the avulsion point decreased around 104 m from 138.5 m to 34.11 m (Table 3.4). Although there may be slight differences, in the flow regime, between the 1985 channel examined in this study and the 1988 channel studied by Buehler et al. (2011), it is clear in both studies that the decrease in width in the parent channel is significant and reflects the huge diversion of flow from the parent channel to the avulsion channel.

Across the DFS, the change in channel width between 1985 and 2022 can be understood by exploring the ratio between 2022 channel width and 1985 channel width where a general decrease in the ratio is observed downstream ($R^2 = -0.65$; Figure 3.19A; Table 3.11). This shows that the 2022 channel becomes smaller than the 1985 channel downstream, which relates to the significant decrease in discharge in the 2022 channel downstream of the Caronal avulsion point. The ratio is explored further within each DFS zone below.

In the proximal zone there is no influence from the Caronal avulsion as this zone is upstream of the avulsion point. There is similarity in width between the 1985 and 2022 channels as the mean ratio is 0.84 (Table 3.11), showing that the 2022 channel is slightly smaller than the 1985 channel. A Mann-Whitney test which was carried out to understand the relationship between channel width in 1985 and in 2022 in the proximal zone, outlined in Results section 3.6.2.1, reveals that there is a significant change in channel width between 1985 and 2022 ($p < 0.01$; Figure 3.23, Table 3.11) despite the channels being of a similar size. This is interesting as the slight decrease in channel width in 2022 can be seen to reflect a change in flow regime over this 37-year-period, or may point to, for example, hydrological differences in discharge from the catchment. However, both the 1985 and 2022 satellite images were filtered between July and September which is outside the flooding season, which indicates that there has been a general decrease in discharge from the catchment area since 1985.

Due to the lack of downstream trends in channel width in both the 1985 channel ($R^2 < 0.01$; Figure 3.2B, Table 3.1) and 2022 channel ($R^2 < 0.01$; Figure 3.5B, Table 3.4) in the proximal zone, the width ratio between these channels also shows no correlation downstream ($R^2 < 0.01$; Figure 3.19B, Table 3.11). This indicates that although there is only a small change in the mean width of the channel in the proximal zone over time, there must be changes in channel shape as the river migrates over time. This is observed on ArcGIS Pro where the 2022 channel polygon overlays the 1985 channel polygon and the evidence of channel migration is visible. Hooke (2023) outlines that the high sensitivity of meandering systems often results in changes in channel morphology and position over relatively short time periods (i.e., 2 to 5 years) in response to frequent hydrological events. Erosion and deposition processes widen and narrow channels resulting in changes in channel width and shape, however, channels are often more stable and less susceptible to erosion when vegetated channel bars and channel banks are present (Hooke, 2023).

In the medial zone the 2022 channel experiences the Caronal avulsion resulting in a wide range of ratio values from 0.08 to 0.90 with a mean of 0.40 (Table 3.11). This shows that on average, the 2022 channel width is less than half the size of the 1985 channel width as the discharge in the channel has decreased significantly. The distal zone shows a further decrease in 2022 channel width in comparison to 1985 channel width as the mean ratio is 0.27. This shows that the 1985 channel is significantly larger than the 2022 channel in the distal zone, this is observed as the mean width of the 1985 channel in the distal zone is 113.03 m (Table 3.1) whereas the mean width of the 2022 channel is 30.08 m (Table 3.4). Additionally, The Zé da Costa avulsion, initiated in 1988 after the 1985 channel was mapped, which changed the location of the active avulsion channel (which is where the current active channel is located) may have experienced a further decrease in discharge due to the flow dispersion processes of the avulsion.

4.3.2 Changes in Sinuosity

Although there are clear changes in channel width between 1985 and 2022, there is no statistically significant change in sinuosity between 1985 and 2022 across the whole DFS except for the distal zone, at the site where the Zé da Costa avulsion changed the position of the active channel. In the proximal and medial DFS zones, the sinuosity values between the 1985 and 2022 channel are very similar (as demonstrated by the p-values of $p = 0.47$ and 0.39, respectively (Table 3.11)) showing that there has been very little change in sinuosity over this 37-year-period.

A slight increase in sinuosity is observed in the proximal zone as the mean sinuosity of the active channel in 2022 is 1.64 (Table 3.7) compared to the 1985 channel, where the mean sinuosity is 1.54 (Table 3.2). This demonstrates that the channel had the capacity to migrate in the proximal zone and thus erode and deposit sediment to increase the sinuosity of the channel. As initially outlined in section 4.1.1, in areas of the DFS where the sediment load is higher (i.e., in the proximal zone), point bar migration increases and results in an increase in sinuosity (Ahmed et al., 2019). The 2022 channel polygon was compared to the 1985 channel polygon in ArcGIS Pro where the increase in sinuosity is observed to be related to the further erosion of meander bends and the deposition and migration of point bar deposits.

In the medial zone, there is only a very slight increase in sinuosity between 1985 and 2022 as the mean sinuosity increases from 1.27 (Table 3.2) to 1.29 (Table 3.7) over this period. Further investigation of the 1985 versus 2022 channel polygons in ArcGIS reveals that a number of meander cutoffs have occurred over this time period. This suggests that some parts of the medial zone have become more sinuous despite the formation of straighter sections of the channel, which form following meander cutoffs (Figure 2.6). The increase in sinuosity over time may not only relate to the growth of existing bends but also the formation of new bends in straighter channel sections (Hooke, 2023). Hooke (2023) explains that channel bank erosion can vary spatially and temporally due to the different cohesive properties of the banks (i.e., due to vegetation), as outlined in section 4.1.2.2. This results in some reaches of the river not being able to migrate as easily and as such, there is no increase in sinuosity. In the distal zone, the 2022 channel is more sinuous than the 1985 channel (increasing from 1.27 in 1985 to 1.39 in 2022). However, this is where the channel changed position on the DFS following the Zé da Costa avulsion and created a new channel which cannot be compared directly to the 1985 channel, which existed on a different location on the DFS.

The sinuosity values in the medial and distal zones of the 1985 and 2022 channel are very similar indicating that there has not been a significant change in sinuosity following the Caronal avulsion. This was also found by Buehler et al. (2011) who noted that the stretch of active channel downstream of the avulsion point did not change over the avulsion process, remaining at a value of 1.28. This study found that the overall sinuosity of the 2022 channel downstream of the Caronal avulsion has increased slightly to 1.39 which is unexpected considering the reduction in migration capacity of the 2022 channel. A potential explanation for this increase in overall sinuosity downstream of the avulsion point between 2008 (Buehler et al., 2011) and 2022 (this study) may be due to the low gradient observed in the distal zone. A low gradient is understood to provide conditions necessary for the development of a sinuous planform. As the sedimentation rate remains low in the distal zone, then this will increase the likelihood of the gradient also remaining low in this DFS reach.

In many other locations across the DFS, in particular the medial zone, the 2022 channel is observed to follow the meandering thalweg of the 1985 channel (as observed in ArcGIS Pro through comparison of the 1985 and 2022 channel polygon centrelines). In these locations, the 2022 channel is observed to follow the parts of the 1985 channel which have been carved by the pre-avulsion channel and are therefore deeper. This has resulted in the sinuosity of the pre-avulsion channel being maintained in many locations as the 2022 channel does not have the capacity to do further erosive work in the channel.

4.3.3 Changes in Channel Belt Width

Although channel width and sinuosity are the only variables that can be compared directly between 1985 and 2022 imagery, clear changes in channel belt width were observed in satellite imagery from 2022. An active channel belt and a pre-avulsion channel belt were identified on satellite imagery from 2022 showing that there has been a significant decrease in active channel belt size as the Caronal avulsion reduced the channel width of the parent channel (active channel). These two channel belts are only differentiated downstream of the Caronal avulsion point and upstream of the Zé da Costa avulsion point where it is clear that there is a change in the discharge and migration capacity of the active channel over time (Figure 3.18). It is clear that as the Caronal avulsion diverts flow from the parent channel to the avulsion channel that there is a significant decrease in channel width in the active channel downstream of the avulsion point. As channel width decreases downstream, the migration capacity of the channel also decreases. This is due to a reduction in discharge and sediment supply, and results in an active channel belt which is very close in width to the active channel.

The pre-avulsion channel belt is clearly much larger than the active channel belt downstream of the Caronal avulsion point and is the product of the migration of a much bigger pre-avulsion channel (i.e., a channel like the 1985 channel). The pre-avulsion channel belt shows that the pre-avulsion channel had a much higher discharge and was able to migrate freely across the DFS surface preserving evidence of this migration in the form of abandoned meander deposits. The preservation of abandoned meander deposits within the pre-avulsion channel belt shows how the pre-avulsion channel was able to migrate over a larger area on the DFS surface, due to its greater migration capacity, and therefore preserve meander deposits in areas of the DFS which were re-occupied by the active channel less frequently.

When abandoned meander deposits are compared to active meander deposits, they show the clear change in discharge and migration rate of the active Taquari channel once the avulsion occurs as there is an obvious size difference. Active meander deposits are formed within the active channel belt which has a significant decrease in size downstream of the Caronal avulsion point and therefore results in a significant decrease in active deposit dimensions downstream of the avulsion point. It is important to note that the active meander deposits upstream of the avulsion point are much larger than the abandoned deposits as this is where discharge and sediment load are highest in the channel, resulting in the rapid growth of active deposits and the frequent reworking of abandoned deposits. However, downstream of the avulsion point, the abandoned meander deposits are much larger than the active deposits as the decrease in discharge and sediment supply in the active channel results in very small active meander deposit dimensions downstream.

As the active channel loses the capacity to transport higher volumes of sediment into medial and distal reaches of the DFS, there is a clear decrease in the size of active deposits formed in comparison to abandoned deposits in these reaches. In the medial zone, the mean active meander deposit area is 0.16 km^2 whereas the mean abandoned meander deposit area is 0.24 km^2 (Table 3.8; Table 3.9). The medial zone includes some meander deposits which are situated upstream of the Caronal avulsion point which may increase the mean area of deposits slightly. The distal zone however, shows a much clearer decrease in active meander deposit dimensions compared to abandoned deposit dimensions as the mean active meander deposit area is 0.0063 km^2 compared to the mean abandoned meander deposit area which is 0.25 km^2. This comparison between active and abandoned meander deposits clearly shows the changes in discharge and sediment supply on the Taquari DFS following the Caronal avulsion. If the Caronal avulsion were to completely abandon the parent channel, then the active meander deposits would no longer grow and the active channel belt would also become abandoned as the avulsion channel continued to expand its own active channel belt.

4.4 Implications

This study shows that the Caronal avulsion has caused significant geomorphic change to the active channel (parent channel of the avulsion) and its active channel belt, both of which experience a significant decrease in size downstream of the avulsion point due to the diversion of discharge from the parent channel to the avulsion channel. The understanding of the geomorphic change which occurs within a river system as a result of an avulsion has important implications for the redistribution of sediment and water resources across modern DFSs (Slingerland and Smith, 2004). For example, avulsions can result in the displacement of water resources relied upon by many humans and wildlife species, and cause wide redistribution of sediment and nutrients which can impact available arable land.

In addition, the understanding of how large volumes of water and sediment are displaced on a DFS is of great importance as avulsions can pose major hazards to society. For example, avulsions can impact the availability of water resources, cause damage to critical infrastructure, and most importantly result in mass displacement of populations and loss of human life (Slingerland and Smith, 2004; Sinha et al., 2014). In 2008, a major avulsion of the Kosi River (India/Nepal) affected around 3 million people with widespread damage to villages and farmland, and the displacement of much of the local population (Chakraborty et al., 2010; Sinha et al., 2014).

Avulsions are common on DFS and are key processes in building stratigraphy as sediment is distributed across the DFS surface (Slingerland and Smith, 2004) changing the topography of the DFS and creating avulsion ridges which may trigger future avulsions (Jones and Schumm, 1999; Assine, 2005). Many avulsions have occurred on the Taquari DFS previously, as many paleochannels are preserved on the DFS surface (Assine, 2005). Avulsions within the Taquari DFS may also increase because of increased flooding and sediment generation in the catchment. Intense agricultural activity in the catchment area of the Taquari DFS removes vegetation that stabilises soil and sediment, which then becomes mobilised and enters the DFS where it is then distributed (Assine, 2005). This increase in sediment entering the DFS has the capacity to bring the river closer to an avulsion threshold over shorter timeframes (Assine, 2005; Buehler et al., 2011). On a DFS, an increase in sediment load can also change the planform type to be more braided as higher sediment load rivers typically develop more braided planforms (Leopold and Wolman, 1957; Hartley et al., 2010).

This study explores the spatial change in fluvial characteristics (i.e., channel width) and meander characteristics (i.e., deposit dimensions) on the Taquari DFS as discharge and sediment supply decrease significantly downstream of the Caronal avulsion point. Spatial trends in DFS have previously been quantified in ancient systems (i.e., Salt Wash DFS; Owen et al., 2015 and Huesca DFS; Martin et al., 2021), however, modern systems (in particular meandering DFSs) have not been quantified in great detail. This study provides a dataset on a modern DFS which shows that DFS trends including active channel width and active channel belt width generally fit an established DFS model as they are seen to decrease downstream as discharge and sediment supply decrease. There is however, a degree of variability in each variable due to local influences such as high sediment supply (i.e., where high variability in active channel width is observed in the proximal zone), and channel belt confinement due to incision (preventing typical DFS distribution processes in the proximal zone).

This study provides a unique dataset on the spatial variability of active and abandoned meander deposits on a modern DFS by filling an important literature gap, as meander characteristics have mainly been studied at reach scale (i.e., exhumed meander deposits and individual meanders across different river systems). There is a clear difference in trends downstream when it comes to the dimensions of both active and abandoned meander deposit dimensions. This is due to the fact that active meander deposits show clear downstream trends in dimensions, which are related to changes in discharge and sediment supply, whereas conversely abandoned meander deposits show no change in dimensions downstream. This occurs despite clear downstream trends being present in the pre-avulsion system from the 1985 active channel width and pre-avulsion channel belt width (downstream of the Caronal avulsion point). This is because the abandoned meander deposits are interpreted to be representative of a long period of deposition, which may encompass many changes in discharge and sediment supply over time as a result of larger-scale hydrological changes.

Although there are no downstream trends observed for the abandoned meander deposits, these deposits give a good indication of the size that an active deposit could grow to if discharge and sediment supply did not reduce over time. Therefore, where the size of abandoned meander deposits increases slightly between medial and distal zones this could be a reflection of an increase in channel sinuosity as the deposits continue to grow despite a decrease in channel width downstream. This would suggest that where sinuosity is able to increase downstream on a DFS then the decreasing channel width would not reduce deposit size as these deposits continue to grow.

The study of meander deposits (point bars) is important as these deposits have been known to host various critical resources such as, uranium and organic-rich siltstones (Berg 1968; Dalh and Hagmaier, 1976) as well as being ideal reservoirs for carbon capture and storage (CCS) (Colombera et al., 2017; Sahoo et al., 2020). This is due to the ideal geometry of meander deposits (compartmentalisation of sandstone and mudstone). The results of this study provide geologists with an idea of how subsurface reservoir dimensions (i.e., deposit shape) can vary spatially across a system. In addition, deposits of meandering rivers have been previously misinterpreted in subsurface as braided rivers. Further research such as a spatial grain size analysis of meandering distributive fluvial systems will be able to use this study on spatial variability to further constrain the dimensions of these deposits.

When considering meander deposits in the rock record as hydrocarbon reservoirs, it is important to understand that these deposits are created under a range of conditions (i.e., during an avulsion or while larger scale climatic changes occur, which influence discharge and sediment supply). Comparing the active meander deposits at one moment in time (2022) to the abandoned meander deposits, which are created over much longer time periods, shows that a range of deposit sizes can be preserved within the same zone of a DFS and therefore will appear together stratigraphically in the rock record. For example, in the medial zone, small-scale active deposits will sit stratigraphically above larger-scale abandoned deposits in the subsurface (Figure 4.3) therefore providing a range of reservoir dimensions. Frequent avulsion processes on the Taquari DFS create fine-grained mudstone deposits which will sit stratigraphically above and below sandstones in the rock record, therefore surrounding the reservoir with an impermeable seal rock (Figure 4.3).

A model of the Taquari DFS (Figure 4.3) was created to compare the pre-avulsion system to the modern system where the dimensions of active variables have significantly decreased downstream of the Caronal avulsion point. This model is useful as it shows the impact that a significant decrease in discharge and sediment supply have had on meander characteristics. It is then inferred that the subsurface dimensions of these channel deposits will decrease downstream (Figure 4.3). This, in turn, will impact the connectivity of meander deposits in subsurface which, as outlined above, have important implications for the reservoir potential of deposits (Colombera et al., 2017; Sahoo et al., 2020).

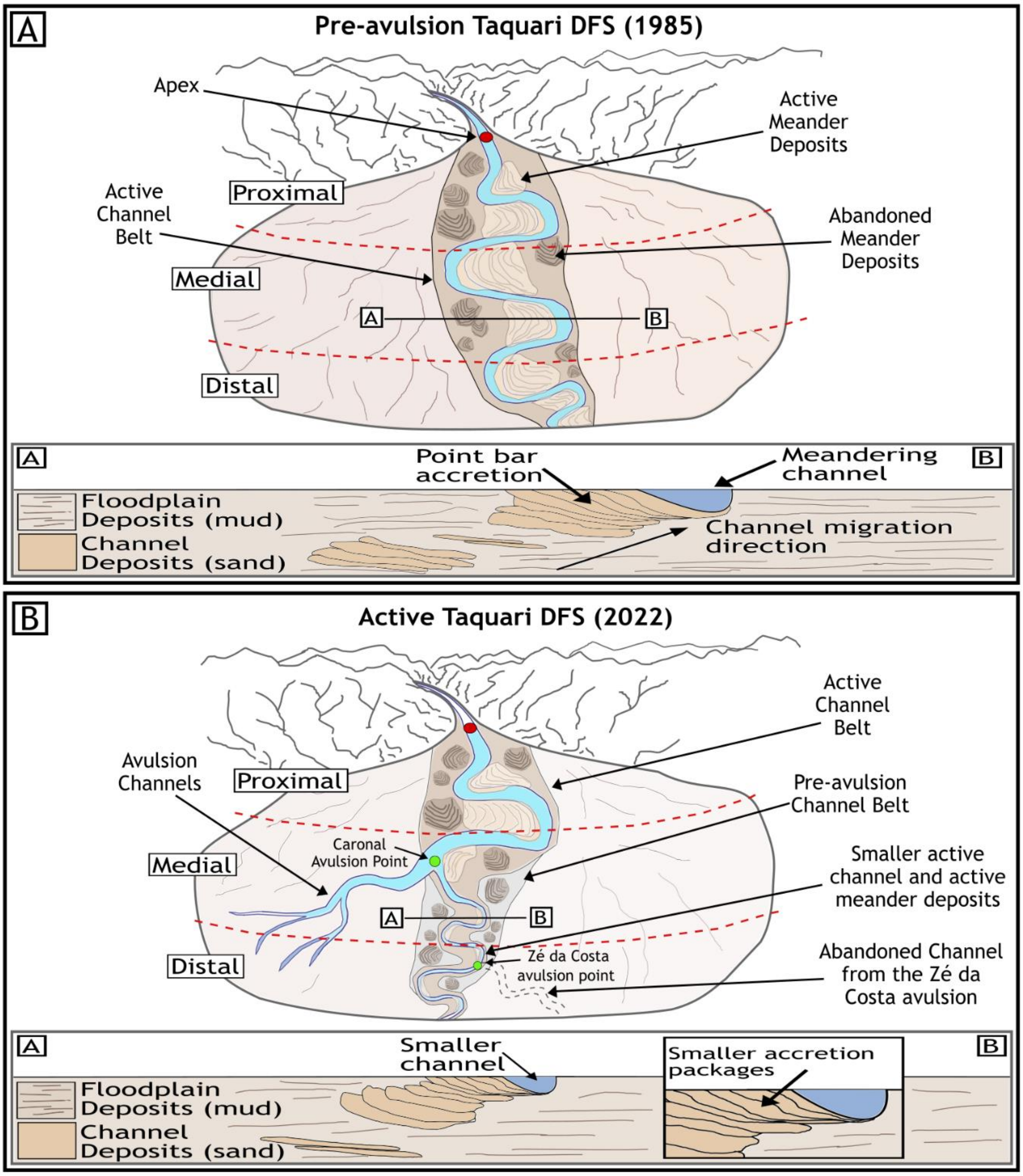

Figure 4.3. A model of the Taquari DFS before the initiation of the Caronal avulsion (A) and during the Caronal avulsion (B). Part A shows the pre-avulsion system which has a larger channel downstream with a larger active channel belt and active meander deposits. Part B shows the significant decrease in active channel width, active channel belt width, and active meander deposit dimensions downstream of the Caronal avulsion point. Abandoned meander deposits show a variability in dimensions downstream. Both models have subsurface interpretations of the change in dimensions and connectivity of point bar deposits following a change in channel width.

5 Conclusions

This study has filled a critical literature gap with regards to quantifying the spatial variability of meander characteristics within a modern DFS (i.e., from apex to toe of the Taquari DFS using satellite imagery from 2022). In addition, this study contributes to the understanding of the impact an avulsion event can have on a parent channel and its associated channel belt and meander deposits. The main findings of this study are outlined below.

- There is a decrease in active channel width, active channel gradient, active channel belt width, pre-avulsion channel belt width, and active meander deposit dimensions downstream on the 2022 Taquari DFS. There is a significant decrease in the dimensions of active variables downstream of the Caronal avulsion point as discharge and sediment supply are diverted to the avulsed channel.

- Across proximal, medial, and distal DFS zones, the largest dimensions are found in the proximal zone where there is also the highest variability across most variables (i.e., active channel width, active meander deposit dimensions, abandoned meander deposit dimensions, and active channel sinuosity) due to the high discharge and sediment supply. In the medial zone, the dimensions of active variables decrease significantly downstream of the Caronal avulsion point and generally decrease downstream. In the distal zone, the dimensions of most variables are smallest and there is also a steady downstream decrease in dimensions for most variables.

- Pre-avulsion channel belt width, although not influenced by the Caronal avulsion, does not display typical DFS characteristics at system scale due to the confinement of this channel belt in the upper DFS. Where the pre-avulsion channel belt is confined, it does not display typical DFS flow distribution processes (i.e., bifurcation) and instead shows these trends downstream of the confinement. Where the pre-avulsion channel belt is unconfined, it shows a decrease in channel belt dimensions which would be typical of a DFS.

- Active meander deposit dimensions decrease downstream with a significant decrease in dimensions downstream of the Caronal avulsion point. This shows the clear link between the decrease in discharge and sediment supply and the growth of smaller meander deposits downstream. This is an important finding as it will allow predictions to be made regarding sandstone-body dimensions downstream on a DFS as channel width decreases.

- Active meander deposits also change shape downstream on the Taquari DFS from more rounded deposits, where deposit length is often greater than deposit width, to more crescent-shaped deposits, where deposit width is often greater than deposit length. This also has important implications for sandstone-body reservoir dimensions.

- Abandoned meander deposits show no downstream trends, likely due to the formation of these deposits over long timescales where deposits are formed under a range of conditions. Abandoned deposits are also preserved over a larger area as the pre-avulsion channel was able to migrate further due to its high discharge.

- The lack of downstream trends for abandoned meander deposits could also indicate that there was an increase in sinuosity downstream in the pre-avulsion channel which resulted in the continued growth of meander deposits despite the reduction in channel width downstream.

- Across proximal, medial, and distal DFS zones, important distinctions are made between active and abandoned meander deposits. In the proximal zone, active deposits are much larger than abandoned deposits as they are still growing and are not reworked as frequently as abandoned deposits. In the medial and distal zones, abandoned meander deposits are significantly larger than active meander deposits. This is due to the abandoned deposits being formed by a larger channel and being preserved over a wider area, whereas the active deposits are formed by a smaller channel which creates smaller deposits.

- There is a clear decrease in active channel width between 1985 and 2022 on the Taquari DFS due to the Caronal avulsion. The pre-avulsion channel width (1985 channel) is observed to be significantly larger than the active channel width in 2022.

- The sinuosity of the active channel has not changed significantly between 1985 and 2022 and is variable downstream in both the 1985 and 2022 active channels. This variability in sinuosity is understood to be a typical DFS characteristic due to meander cut-offs, re-meandering, and changes in slope gradient. The only significant increase in sinuosity is observed in the proximal DFS zone where discharge and sediment supply are largest, and meander deposits grow more rapidly.

5.1 Limitations and Recommendations for Future Research

There were no significant limitations encountered while conducting this research, however, the use of satellite imagery (especially older imagery, such as 1985 Landsat imagery) is often not a high enough resolution for mapping of the system in great detail (especially in distal reaches). This was not a problem within this study as the 1985 Landsat image quality was clear enough to extract the active channel width which could then be compared to the active channel in modern imagery. Details such as channel belt width and meander deposit dimensions could not be identified however, and these were only identified in modern imagery.

Future studies should build on the research presented in this study to conduct a spatial grain size analysis of meander deposits within a meandering distributive fluvial system. This will allow better understanding of sandstone-body reservoir qualities such as porosity and permeability which are essential for hydrocarbon storage or water storage. This will also provide greater insight into the spatial subsurface connectivity of sandstone bodies which are able to convey pollutants. In addition, the further quantification of the spatial variability of meander deposits within a DFS which is not experiencing an avulsion, will give a better indication of the dimensions active deposits which are able to grow larger downstream.

List of References

Ahmed, J., Constantine, J.A. and Dunne, T., 2019. The role of sediment supply in the adjustment of channel sinuosity across the Amazon Basin. Geology, 47(9), pp.807-810.

Assine, M.L., 2005. River avulsions on the Taquari megafan, Pantanal wetland, Brazil. Geomorphology, 70(3-4), pp.357-371.

Assine, M.L., Merino, E.R., Pupim, F.D.N., Macedo, H.D.A. and Santos, M.G.M.D., 2015. The Quaternary alluvial systems tract of the Pantanal Basin, Brazil. Brazilian Journal of Geology, 45, pp.475-489.

Assine, M.L., Merino, E.R., Pupim, F.N., Warren, L.V., Guerreiro, R.L. and McGlue, M.M., 2016. Geology and geomorphology of the Pantanal basin. Dynamics of the Pantanal wetland in South America, pp.23-50.

Bebout, D.G., Loucks, R.G. and Gregory, A.R., 1978. Frio sandstone reservoirs in the deep subsurface along the Texas Gulf Coast-their potential for production of geopressured geothermal energy. University of Texas Bureau of Economic Geology.

Berg, R.R., 1968. Point-bar origin of Fall River Sandstone reservoirs, northeastern Wyoming. AAPG Bulletin, 52(11), pp.2116-2122.

BMJ, 2024. Available at: https://www.bmj.com/about-bmj/resources-readers/publications/statistics-square-one/11-correlation-and-regression ****
Brice, J.C., 1964. Channel patterns and terraces of the Loup Rivers in Nebraska. US Government Printing Office.

Boothroyd, R.J., Williams, R.D., Hoey, T.B., Tolentino, P.L. and Yang, X., 2021. National-scale assessment of decadal river migration at critical bridge infrastructure in the Philippines. *Science of the Total Environment*, *768*, p.144460.

Bryant, M., Falk, P. and Paola, C., 1995. Experimental study of avulsion frequency and rate of deposition. Geology, 23(4), pp.365-368.

Buehler, H.A., Weissmann, G.S., Scuderi, L.A. and Hartley, A.J., 2011. Spatial and temporal evolution of an avulsion on the Taquari River distributive fluvial system from satellite image analysis. Journal of Sedimentary Research, 81(8), pp.630-640.

Bull, W.B., 1968. Alluvial fans. Journal of Geological Education, 16(3), pp.101-106.

Callander, R.A., 1978. River meandering. Annual Review of Fluid Mechanics, 10(1), pp.129-158.

Chakraborty, T., Kar, R., Ghosh, P. and Basu, S., 2010. Kosi megafan: Historical records, geomorphology and the recent avulsion of the Kosi River. Quaternary International, 227(2), pp.143-160.

Chakravorty, U., Magne, B. and Moreaux, M., 2012. Resource use under climate stabilization: Can nuclear power provide clean energy?. Journal of Public Economic Theory, 14(2), pp.349-389.

Colombera, L., Mountney, N.P., Russell, C.E., Shiers, M.N. and McCaffrey, W.D., 2017. Geometry and compartmentalization of fluvial meander-belt reservoirs at the bar-form scale: Quantitative insight from outcrop, modern and subsurface analogues. Marine and Petroleum Geology, 82, pp.35-55.

Dahl, A.R. and Hagmaier, J.L., 1976. Genesis and characteristics of the southern Powder River Basin uranium deposits, Wyoming.

Daniel, J.F., 1971. Channel movement of meandering Indiana streams (No. 732). US Government Printing Office.

Davidson, S.K., Hartley, A.J., Weissmann, G.S., Nichols, G.J. and Scuderi, L.A., 2013. Geomorphic elements on modern distributive fluvial systems. Geomorphology, 180, pp.82-95.

ESRI (2024) World Imagery Overview. Available at https://www.arcgis.com/home/item.html?id=10df2279f9684e4a9f6a7f08febac2a9 (Accessed: 11/02/24).

Fielding, C.R., Ashworth, P.J., Best, J.L., Prokocki, E.W. and Smith, G.H.S., 2012. Tributary, distributary and other fluvial patterns: What really represents the norm in the continental rock record?. Sedimentary Geology, 261, pp.15-32.

Friedkin, J.F., 1945. A laboratory study of the meandering of alluvial rivers. United States Waterways Experiment Station.

Gao, P. and Li, Z., 2024. Exploring meandering river cutoffs. Geological Society, London, Special Publications, 540(1), pp.SP540-2022.

Ghinassi, M., Nemec, W., Aldinucci, M., Nehyba, S., Özaksoy, V. and Fidolini, F., 2014. Plan‐form evolution of ancient meandering rivers reconstructed from longitudinal outcrop sections. Sedimentology, 61(4), pp.952-977.

Gueneralp, I. and Marston, R.A., 2012. Process–form linkages in meander morphodynamics: Bridging theoretical modeling and real world complexity. Progress in Physical Geography, 36(6), pp.718-746.

Gurnell, A., Surian, N. and Zanoni, L., 2009. Multi-thread river channels: a perspective on changing European alpine river systems. Aquatic Sciences, 71, pp.253-265.

Hartley, A. J., Weissmann, G. S., Nichols, G. J., & Warwick, G. L. 2010, Large distributive fluvial systems: characteristics, distribution, and controls on development:Journal of Sedimentary Research, v.80(2),p.167-183.

Hartley, A.J., Owen, A., Swan, A., Weissmann, G.S., Holzweber, B.I., Howell, J., Nichols, G. and Scuderi, L., 2015. Recognition and importance of amalgamated sandy meander belts in the continental rock record. Geology, 43(8), pp.679-682.

Hartley, A.J., Owen, A., Weissmann, G.S. and Scuderi, L., 2018. Modern and ancient amalgamated sandy meander-belt deposits: recognition and controls on development. Fluvial Meanders and Their Sedimentary Products in the Rock Record, pp.349-383.

Heyvaert, V.M.A. and Walstra, J., 2016. The role of long-term human impact on avulsion and fan development. Earth Surface Processes and Landforms, 41(14), pp.2137-2152.

Hirst, J.P.P., 1991. Variations in alluvial architecture across the Oligo-Miocene Huesca fluvial system, Ebro Basin, Spain.

Hooke, J., 2023. Morphodynamics of active meandering rivers reviewed in a hierarchy of spatial and temporal scales. *Geomorphology*, *439*, p.108825.

Hu, F., Li, J., Liu, Z., Zhao, D., Wan, T. and Xu, C., 2019. Sequence and sedimentary characteristics of upper Cretaceous Sifangtai Formation in northern Songliao Baisn, northeast China: Implications for sandstone-type uranium mineralization. Ore Geology Reviews, 111, p.102927.

Ielpi, A. and Ghinassi, M., 2014. Planform architecture, stratigraphic signature and morphodynamics of an exhumed Jurassic meander plain (Scalby Formation, Yorkshire, UK). Sedimentology, 61(7), pp.1923-1960.

Inglis, C.C. and Lacey, G., 1947. MEANDERS AND THEIR BEARING ON RIVER TRAINING. MARITIME AND WATERWAYS ENGINEERING DIVISION. The Institution of Civil Engineers Engineering Division Papers, 5(17), pp.3-24.

Ivory, S.J., McGlue, M.M., Spera, S., Silva, A. and Bergier, I., 2019. Vegetation, rainfall, and pulsing hydrology in the Pantanal, the world's largest tropical wetland. Environmental Research Letters, 14(12), p.124017.

Johnston, S. and Holbrook, J., 2018. Toggling between expansion and translation: The generation of a muddy-normal point bar with an earthquake imprint. Fluvial meanders and their sedimentary products in the rock record, pp.47-80.

Jones, L.S. and Schumm, S.A., 1999. Causes of avulsion: an overview. Fluvial sedimentology VI, pp.169-178.

Knighton, D., 2014. Fluvial forms and processes: a new perspective. Routledge.

Lane, S.N., Richards, K.S. and Chandler, J.H., 1996. Discharge and sediment supply controls on erosion and deposition in a dynamic alluvial channel. Geomorphology, 15(1), pp.1-15.

Lanzoni, S., 2000a. Experiments on bar formation in a straight flume: 1. Uniform sediment. Water Resources Research, 36(11), pp.3337-3349.

Lanzoni, S., 2000b. Experiments on bar formation in a straight flume: 2. Graded sediment. Water Resources Research, 36(11), pp.3351-3363.

Leeder, M.R., 2009. Sedimentology and sedimentary basins: from turbulence to tectonics. John Wiley & Sons.

Leopold, L.B., 1962. Rivers. American Scientist, 50(4), pp.511-537.

Leopold, L. B., Wolman, M. G. 1957. River channel patterns: braided, meandering and straight. US Geol. Surv. Prof Pap. 282-B, pp. 37-86

Leopold, L.B. and Langbein, W.B., 1966. River meanders. Scientific American, 214(6), pp.60-73.

Li, J., Vandenberghe, J., Mountney, N.P. and Luthi, S.M., 2020. Grain-size variability of point-bar deposits from a fine-grained dryland river terminus, Southern Altiplano, Bolivia. Sedimentary Geology, 403, p.105663.

Louzada, R.O., Bergier, I. and Assine, M.L., 2020. Landscape changes in avulsive river systems: Case study of Taquari River on Brazilian Pantanal wetlands. Science of the Total Environment, 723, p.138067.

Louzada, R.O., Bergier, I., Roque, F.O., McGlue, M.M., Silva, A. and Assine, M.L., 2021. Avulsions drive ecosystem services and economic changes in the Brazilian Pantanal wetlands. Current Research in Environmental Sustainability, 3, p.100057.

Macquarie University, 2020, River Styles, Riffle and Pool. Available at https://riverstyles.com/?portfolio=riffle-and-pool

Martin, B., Owen, A., Nichols, G. J., Hartley, A. J., & Williams, R. D. 2021, Quantifying downstream, vertical and lateral variation in fluvial deposits: Implications from the Huesca Distributive Fluvial System:Frontiers in Earth Science,v.8, p.733.

Makaske, B., 2001. Anastomosing rivers: a review of their classification, origin and sedimentary products. Earth-Science Reviews, 53(3-4), pp.149-196.

Makaske, B., Maathuis, B.H., Padovani, C.R., Stolker, C., Mosselman, E. and Jongman, R.H., 2012. Upstream and downstream controls of recent avulsions on the Taquari megafan, Pantanal, south-western Brazil. Earth Surface Processes and Landforms, 37(12), pp.1313-1326.

Makaske, B., Lavooi, E., de Haas, T., Kleinhans, M.G. and Smith, D.G., 2017. Upstream control of river anastomosis by sediment overloading, upper Columbia River, British Columbia, Canada. Sedimentology, 64(6), pp.1488-1510.

Miall, A.D., 2014. Fluvial depositional systems (Vol. 14, p. 316). Cham: Springer International Publishing.

Micheli, E.R. and Larsen, E.W., 2011. River channel cutoff dynamics, Sacramento river, California, USA. River Research and Applications, 27(3), pp.328-344.

Minitab, 2024. Available at: https://support.minitab.com/en-us/minitab/help-and-how-to/statistics/nonparametrics/how-to/mann-whitney-test/interpret-the-results/all-statistics/#:~:text=Minitab%20uses%20the%20Mann%2DWhitney,a%20decision%20about%20the%20test.

Naik, M.U.D., 2024. Adsorbents for the Uranium Capture from Seawater for a Clean Energy Source and Environmental Safety: A Review. ACS Omega, 9(11), pp.12380-12402.

Nanson, G.C., 1980. Point bar and floodplain formation of the meandering Beatton River, northeastern British Columbia, Canada. Sedimentology, 27(1), pp.3-29.

Newell, A.J. and Shariatipour, S.M., 2016. Linking outcrop analogue with flow simulation to reduce uncertainty in sub-surface carbon capture and storage: an example from the Sherwood Sandstone Group of the Wessex Basin, UK. Geological Society, London, Special Publications, 436(1), pp.231-246.

Nichols, G.J. and Fisher, J.A., 2007. Processes, facies and architecture of fluvial distributary system deposits. Sedimentary geology, 195(1-2), pp.75-90.

Nie, F., Yan, Z., Feng, Z., Li, M., Xia, F., Zhang, C., Wang, Y., Yang, J., Kang, S. and Shen, K., 2020. Genetic models and exploration implication of the paleochannel sandstone-type uranium deposits in the Erlian Basin, North China–A review and comparative study. Ore Geology Reviews, 127, p.103821.

Nyberg, B., Henstra, G., Gawthorpe, R.L., Ravnås, R. and Ahokas, J., 2023. Global scale analysis on the extent of river channel belts. Nature Communications, 14(1), p.2163.

Owen, A., Nichols, G.J., Hartley, A.J., Weissmann, G.S. and Scuderi, L.A., 2015. Quantification of a distributive fluvial system: the Salt Wash DFS of the Morrison Formation, SW USA. Journal of Sedimentary Research, 85(5), pp.544-561.

Peakall, J., Ashworth, P.J. and Best, J.L., 2007. Meander-bend evolution, alluvial architecture, and the role of cohesion in sinuous river channels: a flume study. Journal of Sedimentary Research, 77(3), pp.197-212.

Poff, N.L., 2002. Ecological response to and management of increased flooding caused by climate change. Philosophical transactions of the royal society of London. Series A: mathematical, physical and engineering sciences, 360(1796), pp.1497-1510.

Porsani, J.L., Assine, M.L. and Moutinho, L., 2005. Application of GPR in the study of a modern alluvial megafan: the case of the Taquari River in Pantanal Wetland, west-central Brazil. Subsurface Sensing Technologies and Applications, 6, pp.219-233.

Rhoads, B.L., 2020. River dynamics: geomorphology to support management. Cambridge University Press.

Russell, C.E., Mountney, N.P., Hodgson, D.M. and Colombera, L., 2018. A novel approach for prediction of lithological heterogeneity in fluvial point-bar deposits from analysis of meander morphology and scroll-bar pattern. Fluvial Meanders and Their Sedimentary Products in the Rock Record, pp.385-417.

Sahoo, H., Gani, M.R., Gani, N.D., Hampson, G.J., Howell, J.A., Storms, J.E., Martinius, A.W. and Buckley, S.J., 2020. Predictable patterns in stacking and distribution of channelized fluvial sand bodies linked to channel mobility and avulsion processes. Geology, 48(9), pp.903-907.

Santos, M.G., Hartley, A.J., Mountney, N.P., Peakall, J., Owen, A., Merino, E.R. and Assine, M.L., 2019. Meandering rivers in modern desert basins: Implications for channel planform controls and prevegetation rivers. Sedimentary Geology, 385, pp.1-14.

Schumm, S.A., 1963. Sinuosity of alluvial rivers on the Great Plains. Geological Society of America Bulletin, 74(9), pp.1089-1100.

Schumm, S.A., 1985. Patterns of alluvial rivers. Annual Review of Earth and Planetary Sciences, 13(1), pp.5-27.

Schook, D.M., Rathburn, S.L., Friedman, J.M. and Wolf, J.M., 2017. A 184-year record of river meander migration from tree rings, aerial imagery, and cross sections. *Geomorphology*, *293*, pp.227-239.

Seminara, G., Zolezzi, G., Tubino, M. and Zardi, D., 2001. Downstream and upstream influence in river meandering. Part 2. Planimetric development. Journal of Fluid Mechanics, 438, pp.213-230.

Shukla, T. and Rhoads, B.L., 2023. Meandering rivers that anabranch in the upper Midwest (USA): Prevalence, morphological characteristics, and power regimes. Geomorphology, 440, p.108854.

Sinha, R., Sripriyanka, K., Jain, V. and Mukul, M., 2014. Avulsion threshold and planform dynamics of the Kosi River in north Bihar (India) and Nepal: A GIS framework. Geomorphology, 216, pp.157-170.

Singh, D.S. and Awasthi, A., 2011. Natural hazards in the Ghaghara river area, Ganga Plain, India. Natural Hazards, 57, pp.213-225.

Slingerland, R. and Smith, N.D., 2004. River avulsions and their deposits. Annu. Rev. Earth Planet. Sci., 32, pp.257-285.

Smith, N.D., Cross, T.A., Dufficy, J.P. and Clough, S.R., 1989. Anatomy of an avulsion. Sedimentology, 36(1), pp.1-23.

Smith, D.G., Hubbard, S.M., Leckie, D.A. and Fustic, M., 2009. Counter point bar deposits: lithofacies and reservoir significance in the meandering modern Peace River and ancient McMurray Formation, Alberta, Canada. Sedimentology, 56(6), pp.1655-1669.

Swan, A., Hartley, A.J., Owen, A. and Howell, J., 2018. Reconstruction of a sandy point-bar deposit: implications for fluvial facies analysis. Fluvial Meanders and Their Sedimentary Products in the Rock Record, pp.445-474.

Ventra, D. and Clarke, L.E., 2018. Geology and geomorphology of alluvial and fluvial fans: current progress and research perspectives. Geological Society, London, Special Publications, 440(1), pp.1-21.
Visher, G.S., 1960. Fluvial processes as interpreted from ancient and recent fluvial deposits.

Weissmann, G.S., Hartley, A.J., Scuderi, L.A., Nichols, G.J., Owen, A., Wright, S., Felicia, A.L., Holland, F. and Anaya, F.M.L., 2015. Fluvial geomorphic elements in modern sedimentary basins and their potential preservation in the rock record: a review. Geomorphology, 250, pp.187-219.

Weissmann, G.S., Hartley, A.J., Scuderi, L.A., Nichols, G.J., Davidson, S.K., Owen, A., Atchley, S.C., Bhattacharyya, P., Chakraborty, T., Ghosh, P. and Nordt, L.C., 2013. Prograding distributive fluvial systems—geomorphic models and ancient examples.

Weissmann, G.S., Hartley, A.J., Nichols, G.J., Scuderi, L.A., Olson, M.E., Buehler, H.A. and Massengill, L.C., 2011. Alluvial facies distributions in continental sedimentary basins—distributive fluvial systems.

Weissmann, G.S., Hartley, A.J., Nichols, G.J., Scuderi, L.A., Olson, M., Buehler, H. and Banteah, R., 2010. Fluvial form in modern continental sedimentary basins: distributive fluvial systems. Geology, 38(1), pp.39-42.

Williams, R.E., 2023. Quantifying variability within the medial zone of modern distributive fluvial systems: implications for reservoir characterisation. Unpublished MSc by Research Thesis. University of Glasgow.

Willis, B.J. and Tang, H., 2010. Three-dimensional connectivity of point-bar deposits. Journal of Sedimentary Research, 80(5), pp.440-454.

Wilzbach, M.A. and Cummins, K.W., 2008. Rivers and streams: Physical setting and adapted biota.

Wolman, M.G. and Leopold, L.B., 1957. River flood plains: some observations on their formation (No. 282-C, pp. 87-109). US Government Printing Office.

Xiao, C., Chen, J., Yuan, X., Chen, R. and Song, X., 2020. Model test of the effect of river sinuosity on nitrogen purification efficiency. Water, 12(6), p.1677.

Yang, C.T., 1971. Formation of riffles and pools. Water Resources Research, 7(6), pp.1567-1574.

Zani, H., Assine, M.L. and McGlue, M.M., 2012. Remote sensing analysis of depositional landforms in alluvial settings: Method development and application to the Taquari megafan, Pantanal (Brazil). Geomorphology, 161, pp.82-92.